

Protein conformational fluctuations and
aromatic ring dynamics studied by NMR



Matthias Dreydoppel

Protein conformational fluctuations and
aromatic ring dynamics studied by NMR

Protein conformational fluctuations and aromatic ring dynamics
studied by NMR

Dissertation

zur Erlangung des Doktorgrades der Naturwissenschaften
(Dr. rer. nat.)

der

Naturwissenschaftlichen Fakultät II
Chemie, Physik und Mathematik

der Martin-Luther-Universität
Halle-Wittenberg

vorgelegt von

Matthias Dreydoppel
geb. am 24. März 1993 in Neuwied

Supervisor and first reviewer: Prof. Dr. Jochen Balbach

Second reviewer: Prof. Dr. Kay Saalwächter

Third reviewer: Prof. Dr. Paul Schanda

Date of public defense: 17 March 2023

Papers I & II published by Springer Nature

Papers III & IV published by American Chemical Society

Cover illustration by Karin Scharf

Quotation on the facing page from

The Hobbit. HarperCollins Publishers, 2006

*Knowing the truth about the vanishing
did not lessen their opinion of Bilbo at all;
for they saw that he had some wits, as well
as luck and a magic ring – and all three
are very useful possessions.*

J. R. R. Tolkien, *The Hobbit*

Contents

List of publications	iv
Populärwissenschaftliche Zusammenfassung	vii
1 Introduction	1
Protein GB1	3
2 NMR	5
Nuclear Magnetism	5
Bloch Equations and the Rotating Frame	7
Theoretical Considerations	II
Spin Interactions	13
Chemical Shift	13
Scalar Coupling	13
Residual Dipolar Coupling	14
Chemical Exchange	15
Rotating-Frame Relaxation	17
The $R_{1\rho}$ Relaxation Dispersion Experiment	19
Longitudinal Relaxation Optimization	20
Spin State Selection	21
The Relaxation Period	22
Some Practical Aspects	23
3 Energetics of Protein Fluctuations	25
Aromatic Ring Flips	25
Transition-State Theory and Activation Parameters	27
Compressibility of Proteins	32
4 Results and Conclusions	35
Paper I: Slow ring flips in aromatic cluster of GB1 studied by aromatic ^{13}C relaxation dispersion methods	35
Paper II: ^1H $R_{1\rho}$ relaxation dispersion experiments in aromatic side chains	36
Paper III: Transition-state compressibility and activation volume of tran- sient protein conformational fluctuations	37

Paper IV: Characterizing fast conformational exchange of aromatic rings using residual dipolar couplings: Distinguishing jumplike flips from other exchange mechanisms	38
Paper I	41
Paper II	53
Paper III	65
Paper IV	77
5 Summary	87
Outlook	89
References	91
Supplement	105
Supporting Information to Papers I and III	105
Curriculum vitae	123
Statutory Declaration – Eidesstattliche Erklärung	124
Acknowledgements – Danksagung	125

List of publications

This thesis is based on the following publications, referred to by their Roman numerals:

- I **Slow ring flips in aromatic cluster of GB1 studied by aromatic ^{13}C relaxation dispersion methods**
M. Dreydoppel, H. N. Raum, U. Weininger
J. Biomol. NMR, 2020, 74(2), pp. 183-191
- II **^1H $R_{1\rho}$ relaxation dispersion experiments in aromatic side chains**
M. Dreydoppel, R. J. Lichteneker, M. Akke, U. Weininger
J. Biomol. NMR, 2021, 75(10), pp. 383-392
- III **Transition-state compressibility and activation volume of transient protein conformational fluctuations**
M. Dreydoppel, B. Dorn, K. Modig, M. Akke, U. Weininger
JACS Au, 2021, 1(6), pp. 833-842
- IV **Characterizing fast conformational exchange of aromatic rings using residual dipolar couplings: Distinguishing jumplike flips from other exchange mechanisms**
M. Dreydoppel, M. Akke, U. Weininger
J. Phys. Chem. B, 2022, 126(40), pp. 7950-7956

All papers are reproduced with permission of their respective publishers.

Publications which are not included in this thesis:

Equilibrium and kinetic unfolding of GB1: Stabilization of the native state by pressure

M. Dreydoppel, P. Becker, H. N. Raum, S. Gröger, J. Balbach, U. Weininger
J. Phys. Chem. B, 2018, 122(38), pp. 8846-8852

Conformational exchange of aromatic side chains by ¹H CPMG relaxation dispersion

H. N. Raum, M. Dreydoppel, U. Weininger
J. Biomol. NMR, 2018, 72(1), pp. 105-114

Site-selective ¹H/²H labeling enables artifact-free ¹H CPMG relaxation dispersion experiments in aromatic side chains

H. N. Raum, J. Schörghuber, M. Dreydoppel, R. J. Lichteneker, U. Weininger
J. Biomol. NMR, 2019, 73(10), pp. 633-639

Monitoring protein unfolding transitions by NMR-spectroscopy

M. Dreydoppel, J. Balbach, U. Weininger
J. Biomol. NMR, 2022, 76(1-2), pp. 3-15

Populärwissenschaftliche Zusammenfassung

Proteine gehören zu den wichtigsten biologischen Molekülen und übernehmen in lebenden Organismen zahlreiche Aufgaben. Sie führen dabei dynamische Fluktuationen ihrer Struktur aus, um sich zu stabilisieren oder ihre Funktion auszuüben. Zum Beispiel erfordert das Binden eines Proteins an ein Zielmolekül ein vorheriges Justieren der Bindungsstelle. Entsprechend wichtig ist das Verständnis der zugrundeliegenden Mechanismen auch für die Entwicklung neuer Medikamente.

Strukturelle Formänderungen von Proteinen können auf Zeitskalen zwischen Sekunden und weniger als Milliardstel Sekunden stattfinden, und sind für viele physikalische Messmethoden unsichtbar. Kernspinresonanzspektroskopie (engl. NMR) ermöglicht die Messung von atomaren Strukturen und kann sogar die Dynamik einzelner Molekülteile nachweisen. Besonders interessant sind die sogenannten aromatischen Aminosäuren in Proteinen, die einen Ring aus sechs Kohlenstoffatomen besitzen. Vor etwa 50 Jahren wurde mittels NMR nachgewiesen, dass sich diese Ringe im Innern von Proteinen regelmäßig um eine eigene Achse drehen, und man nannte diese Bewegungen Ringflips. Bis dahin hatte man Proteinstrukturen für zu starr und unbeweglich gehalten, um solche Dynamik zu ermöglichen. Aromatische Aminosäuren, die selbst wichtig für die Bindung von Proteinen an andere Moleküle sind, geben damit in einzigartiger Weise Auskunft über die Flexibilität der Proteine. Da Ringflips experimentell schwierig zu verfolgen sind, gab es lange Zeit trotzdem nur wenig entsprechende Studien.

In dieser Doktorarbeit werden vier wissenschaftliche Arbeiten präsentiert, in denen wir die Ringflips in einem natürlichen Protein untersucht haben. Die Rate, also Häufigkeit der Ringflips, hängt von Temperatur und Druck ab, unter dem sich das Protein befindet. Daraus kann berechnet werden, welche Energie für einen Ringflip unter den jeweiligen Bedingungen nötig ist und was das über die Struktur des gesamten Moleküls aussagt. Neben anderen thermodynamischen Parametern konnten wir erstmals die Änderung der Kompressibilität während eines Ringflips bestimmen. Dieser Parameter gibt an, wie gut sich ein Körper zusammendrücken lässt. Wir haben herausgefunden, dass sich das Innere des Proteins während des Flips ähnlich einer Flüssigkeit verhält, obwohl die feste Grundstruktur immer wieder eingenommen wird. Ringflips können damit auch bei sehr hohem Druck stattfinden, wenn ein Ausdehnen des gesamten Moleküls nicht mehr möglich ist. Wir konnten die Methoden zur Untersuchung aromatischer Aminosäuren verbessern und nachweisen, dass sich die Ringe tatsächlich sprungartig bewegen und wieder in ihren Anfangszustand zurückkehren, und sich nicht etwa kontinuierlich weiterdrehen. Die Proteinstruktur ist also nicht beliebig fluktuierend, sondern wechselt zwischen bestimmten Formen. Dieses Wissen und die eingebrachten Methoden sind nützlich für die weitere Forschung zur Flexibilität und Funktion von Proteinen.

Chapter 1

Introduction

In his famous *Lectures on Physics*, Nobel laureate Richard Feynman stated that “certainly no subject or field is making more progress on so many fronts at the present moment, than biology, and if we were to name the most powerful assumption of all, which leads one on and on in an attempt to understand life, it is that all things are made of atoms, and that everything that living things do can be understood in terms of the jiggings and wiggings of atoms.”¹ In line with this perspective it can be conceived today that biological molecules, with proteins as the most important class among them, are dynamic entities and that their flexibility is often critically related to their function.² Therefore, the research field of protein dynamics and flexibility is exceptionally developing. It has revealed that not only the structural ground states of proteins are ensembles fluctuating around energy minima, but that these molecules often feature transient alternations between different conformations.³ Such conformational fluctuations are associated with the movement of many atoms and they are more than a “lubricant for functional motions.”⁴ They are important in thermodynamic stabilization and in all processes that require structural adjustments of active sites, such as in molecular recognition, ligand binding and allostery.⁵ Consequently, the understanding of the underlying mechanisms is also of high importance for protein structure-based drug design.⁶

Protein conformational fluctuations cover a wide range of timescales from picoseconds to seconds and beyond.² Often the alternative states linked to biological function are only transiently formed and sparsely populated, so that they are elusive for many spectroscopic methods.⁷ Nuclear magnetic resonance (NMR) is the experimental method of choice for the investigation of internal motions: NMR active nuclei give account of conformational fluctuations with exceptional time and spatial resolution and the measured parameters report not only on structure but are also sensitive to motion.⁵ Half a century ago, seminal NMR experiments by Wüthrich and Wagner as well as

Campbell and coworkers detected rotational motions of aromatic side chains within a protein core.^{8,9} This fundamentally changed the view of proteins from static to dynamic systems and already signified the importance of NMR spectroscopy in protein science.⁵ In the last decades, a variety of NMR methods for the investigation of conformational dynamics together with theoretical descriptions appropriate for their interpretation were developed.^{10,11} Numerous examples and case studies exist where NMR spectroscopy provided insights into the mechanisms of protein function. They can be found in the literature and are frequently collected in extensive review articles.^{2,12}

Conformational dynamics on the microsecond to millisecond time scale are often linked to biological function. They can be explored by chemical exchange methods such as CPMG and $R_{1\rho}$ relaxation dispersion and the related CEST and DEST experiments.¹³ $R_{1\rho}$ relaxation dispersion experiments have accordingly been applied to processes critically related to protein function, namely folding, ligand binding and catalysis.¹⁴ Likewise, isotope-labeling has made more positions in protein structures amenable to NMR dynamic studies and extended the size limitations of accessible molecules.¹⁵ Complementary and advanced insights into the relationship of structure and dynamics of proteins have additionally been achieved by molecular dynamics (MD) simulations and other rapidly evolving computational methods. Standard MD simulations however probe processes on time scales below microseconds and to date have difficulties to access microsecond and millisecond dynamics.¹⁶

Aromatic amino acid side chains are interesting and particularly powerful probes for the study of protein dynamics. They constitute a significant part of the hydrophobic core of proteins, where they contribute to the stability of the molecule by means of the hydrophobic effect,¹⁷ as hydrogen bond acceptors¹⁸ or by interaction with methionine.¹⁹ At the same time the dynamic motions of aromatic rings and other side chains signify the flexibility of the inner protein structure.²⁰ Aromatic residues are of high importance in the functional binding of proteins to other molecules. They are prevalent as anchor side chains in protein-protein binding interfaces,^{21,22,23} protein-DNA complexes^{24,25} and at enzyme catalytic sites.^{26,27} Aromatic side chains are participating in the recognition of mRNA,²⁸ antigens²⁹ and neurotransmitters.³⁰ Recent studies revealed the significance of structure fluctuations associated with aromatic ring dynamics for the ligand binding selection to pharmaceutical drugs³¹ and for the biodegradation of synthetic polymers.³²

The research work presented in this thesis aims to enlighten the mechanistic and energetic principles of protein conformational fluctuations by focusing on aromatic ring dynamics. Using an advantageous model protein described below, several questions will be addressed: How static or dynamic are certain regions of proteins? What are the free energy barriers and energetic differences between the ground and transition state of ring flip transitions? What is the precise exchange mechanism of a ring flip

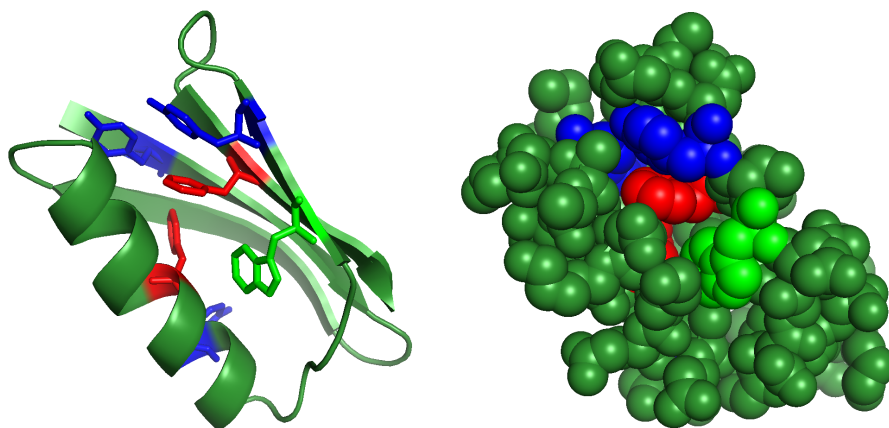


Figure 1.1: Structure of protein GB1. *Left:* The backbone is shown in ribbon representation and aromatic amino acids are depicted as sticks. Phenylalanines are coloured red, tyrosines blue and tryptophan light green, respectively. *Right:* The same perspective with atoms displayed as spheres. For simplicity, standard van der Waals-radii of the respective elements are used and hydrogen atoms are not shown. Created with the PyMOL software³³ based on the three-dimensional structure of GB1³⁴, PDB entity 1PGB.

and what role do internal cavities play during structural perturbations? To which extent do volume changes observable as “breathing motions” of proteins report on the internal structural processes?

State-of-the-art NMR relaxation dispersion methods are used and refined to explore the thermodynamic characteristics of ring flips in a temperature and pressure dependent way. In the following chapters, it will be explained that NMR is the only experimental technology that allows for detection of ring flips and for measurement of the flip rates. Therefore the fundamental concepts of NMR, chemical exchange and the required experiments will be described before the research projects are presented. Correspondingly the scientific background of aromatic ring flips and the associated energetics will be introduced to make the issues discussed in the articles as understandable as possible.

Protein GB1

The protein used in the studies of this thesis is GB1, one of the two binding domains of protein G from the cell wall of *Streptococcus* bacteria, which binds to immunoglobulin G.³⁵ It is a small protein with a molecular weight of about 6.5 kDa, consisting of 56 amino acids which form a four-stranded β -sheet encompassing one α -helix.³⁶ The structure is illustrated in Figure 1.1. GB1 is monomeric, very soluble, has a high structural long-term stability and is thus regarded as an ideal model system for protein NMR research. It is well characterized in terms of thermal,³⁷ mechanical,³⁸ and

pressure stability^{39,40} and structural changes under variation of pH,^{41,42} and used for example as a model for protein folding,⁴³ side chain protonation kinetics⁴⁴ or as crowding agent.⁴⁵ We make use of a variant of GB1 which has three amino acid mutations, T2Q to reduce N-terminal cleavage as well as N8D and N37D to adjust consequent covalent rearrangements.⁴¹ The full name of the system is hence PGB1-QDD. It is structurally identical to the wild type and shows reversible unfolding for temperatures up to 95 °C.⁴¹

GB1 possesses an extensive network of hydrogen bonds and a tightly packed hydrophobic core,³⁶ which is essential for the structural stability of the protein.⁴⁶ In the structure six aromatic amino acids can be found, they are highlighted in Fig. 1.1. Two phenylalanine and two tyrosine residues form an aromatic cluster in the core region, while another tyrosine side chain is exposed to the surface of the molecule. As will be shown, all of these aromatic rings are amenable to ring flips under differing conditions. The respective NMR signals are well resolved and affected characteristically by the exchange processes. This allows for the application and implementation of appropriate relaxation dispersion methods. The tryptophan side chain cannot perform symmetric rotational motions, wherefore its nuclei provide control values. In the right image in Fig. 1.1, atoms of GB1 are represented as spheres. This gives an impression of the packing density of the molecule which is crucial for the dynamics of ring flips. Imagining the rings rotating within in the structure evokes a first notion of how flexible and lively the structure must be.

Chapter 2

NMR

The nearly simultaneous and independent discovery of nuclear magnetic resonances by the groups of Purcell⁴⁷ and Bloch⁴⁸ in 1946 started a story of success. Continuously growing since then, NMR spectroscopy is now widely used in all natural sciences, its utilization ranging from material characterization and food chemistry to environmental science and medical imaging.⁴⁹ It is particularly valuable for the examination of biological macromolecules, their structure as well as internal dynamics. This chapter will give a short introduction to the broad field of NMR, following the textbooks by Levitt,⁴⁹ Cavanagh et al.⁵⁰ and van de Ven,⁵¹ unless stated otherwise. In preparation for understanding the relaxation dispersion experiments performed in this thesis, all relevant tools shall be elucidated, drawing particular attention to the application on aromatic protein side chains, where appropriate.

Nuclear Magnetism

The angular momentum of atomic nuclei is characterized by the nuclear spin quantum number, I . Nuclei with odd mass numbers have half-integral spin quantum numbers, such as the most important isotopes for biomolecular NMR spectroscopy, like ^1H and ^{13}C with $I = 1/2$. Nuclei with even mass numbers and odd atomic numbers have integral spin quantum numbers, like the deuteron (^2H) with $I = 1$. The nuclear spin angular momentum is a vector with a quantized magnitude of

$$|\mathbf{I}| = [\mathbf{I} \cdot \mathbf{I}]^{1/2} = \hbar[I(I + 1)]^{1/2} \quad (2.1)$$

where I is the nuclear spin quantum number and \hbar is the reduced Planck constant.

Since only one of the Cartesian coordinates of \mathbf{I} can be specified simultaneously with its magnitude, the z -component is selected as

$$I_z = \hbar m \quad (2.2)$$

with the magnetic quantum number $m = (-I, -I + 1, \dots, I - 1, I)$. Thus, the energy state of a spin I is $(2I + 1)$ -fold degenerate, with all quantum states having the same energy. This degeneracy is broken by the application of an external magnetic field, leading to the nuclear Zeeman splitting between the spin levels.

The magnetic properties of atomic nuclei are explained by the nuclear spin angular momentum, because it is directly proportional to the nuclear magnetic moment μ :

$$\begin{aligned} \boldsymbol{\mu} &= \gamma \mathbf{I} \\ \mu_z &= \gamma I_z = \gamma \hbar m \end{aligned} \quad (2.3)$$

The proportionality constant γ is the gyromagnetic ratio, which is characteristic for different nuclei and determines their NMR sensitivity. The energy of nuclear spin states in the presence of an external magnetic field \mathbf{B} is given by

$$E = -\boldsymbol{\mu} \cdot \mathbf{B} \quad (2.4)$$

For NMR experiments, the magnetic field is designed to be static and directed along the z -axis of the laboratory coordinate system, denoted \mathbf{B}_0 . Therefore, one can represent the energy levels of all possible angular momentum z -components depending on the static magnetic field strength, B_0 , as

$$E_m = -\gamma I_z B_0 = -\gamma \hbar m B_0 \quad (2.5)$$

The energy levels are called Zeeman levels, and transitions between them can be achieved by application of electromagnetic radiation. In consequence of the selection rule for magnetic dipole transitions, $\Delta m = \pm 1$, the energy difference between two adjacent Zeeman levels is

$$\Delta E = \gamma \hbar B_0 \quad (2.6)$$

and the frequency of the electromagnetic radiation required to accomplish a transition between the levels is given by

$$\omega_0 = \Delta E/\hbar = \gamma B_0 \quad (2.7)$$

This frequency can be identified with the Larmor frequency, which in the classical description is the angular velocity of a nuclear magnetic moment vector precessing around the static magnetic field.

The different energy states of equation (2.5) are not populated equally at thermal equilibrium, because certain orientations of the magnetic dipole vector are energetically more favourable than others. The population of nuclei in a certain spin state N_m relative to the total number of spins N is following a Boltzmann distribution:

$$\begin{aligned} \frac{N_m}{N} &= \exp\left(\frac{-E_m}{k_B T}\right) / \sum_{m=-I}^I \exp\left(\frac{-E_m}{k_B T}\right) \\ &\approx \frac{1}{2I+1} \left(1 + \frac{\gamma \hbar m B_0}{k_B T}\right) \end{aligned} \quad (2.8)$$

where k_B is the Boltzmann constant and T is the temperature. The approximation holds for temperatures relevant for solution NMR.

In a macroscopic sample at equilibrium, the longitudinal (z -) components of the nuclear magnetic moments of all nuclei add up to the bulk magnetic moment, \mathbf{M} . Its magnitude M_0 can be expressed using (2.3) and (2.8) as

$$M_0 = \gamma \hbar \sum_{m=-I}^I m N_m \approx \frac{N \gamma^2 \hbar^2 I(I+1)}{3k_B T} B_0 \quad (2.9)$$

The sensitivity of NMR spectroscopy depends on the small disparity of the populations of the Zeeman states. The latter equations show how this can be enhanced using high magnetic field strengths and isotopes with high gyromagnetic ratios. For protons (^1H has the highest γ of $2.675 \cdot 10^6 \text{ rad s}^{-1} \text{ T}^{-1}$) in a magnetic field of 14.1 T, as used in the present studies, the difference of populations is on the order of 1 per 10000.

Bloch Equations and the Rotating Frame

The Bloch formalism⁵² provides a semiclassical model for the evolution of the bulk magnetization under the effects of radiofrequency (rf) pulses and relaxation. The bulk magnetic moment of an ensemble of noninteracting spin-1/2 nuclei can be expressed

as a time-dependent Cartesian vector, $\mathbf{M}(t)$. Its time derivative in the presence of a magnetic field is given by

$$\frac{d}{dt}\mathbf{M}(t) = \mathbf{M}(t) \times \gamma\mathbf{B}(t) \quad (2.10)$$

Since the magnetic moment precesses around the static magnetic field, it causes a time-varying magnetic field which in principle can be measured via induction. Induced currents in a coil constitute the NMR signal, but they cannot be measured as long as the bulk magnetization is collinear with the z -axis. This equilibrium state is therefore disturbed by application of electromagnetic rf pulses. They introduce a second magnetic field and tilt the magnetization vector away from the static field, so that oscillating x - and y -components of the precession motion can be detected. The magnetic component of an rf field along the x -axis is given as

$$\begin{aligned} \mathbf{B}_{\text{rf}}(t) = & B_1(\cos(\omega_{\text{rf}}t + \phi)\mathbf{i} + \sin(\omega_{\text{rf}}t + \phi)\mathbf{j}) \\ & + B_1(\cos(\omega_{\text{rf}}t + \phi)\mathbf{i} - \sin(\omega_{\text{rf}}t + \phi)\mathbf{j}) \end{aligned} \quad (2.11)$$

Here, B_1 is the amplitude of the applied field, ω_{rf} is the frequency of the rf field, which is called the carrier frequency of the pulse, ϕ is its phase, and \mathbf{i} and \mathbf{j} are unit vectors for the x - and y -axes, respectively. The two terms in (2.11) denote circularly polarized fields rotating in the same and opposite sense as the magnetic moment, respectively. To solve Eq. (2.10) despite the time-dependency of the field, it is convenient to move from the laboratory coordinate system to a rotating reference frame. This is chosen to rotate with an angular frequency of ω_{rf} around the z -axis. The magnetization in the rotating frame evolves analogously to (2.10) with respect to an effective field, \mathbf{B}_{eff} , given by

$$\mathbf{B}_{\text{eff}} = B_1 \cos \phi \mathbf{i}^r + B_1 \sin \phi \mathbf{j}^r + \Delta B_0 \mathbf{k}^r \quad (2.12)$$

where \mathbf{i}^r , \mathbf{j}^r and \mathbf{k}^r are unit vectors in the rotating frame, and ΔB_0 is the reduced static field with

$$\Delta B_0 = B_0 + \frac{\omega_{\text{rf}}}{\gamma} = -\Omega/\gamma \quad (2.13)$$

in which $\Omega = \omega_0 - \omega_{\text{rf}}$ is defined as the offset between the carrier and the actual Larmor frequency of a spin. Within the rotating frame, the tilted magnetic moment appears to precess around an effective field B_{eff} with the strength

$$B_{\text{eff}} = \sqrt{B_1^2 + (\Delta B_0)^2} = B_1 / \sin \theta \quad (2.14)$$

where θ denotes the angle through which the effective field is tilted from the z -axis. It is defined by

$$\tan \theta = \frac{B_1}{\Delta B_0} = \frac{\omega_1}{\Omega} \quad (2.15)$$

using $\omega_1 = -\gamma B_1$ as the pulse strength in frequency units.

Given the duration τ_p of a rf pulse, one can calculate the effective rotation angle α executed by the magnetization vector as

$$\alpha = -\gamma B_1 \tau_p / \sin \theta = \omega_1 \tau_p / \sin \theta \quad (2.16)$$

The rf pulse is applied on-resonance when $\omega_{\text{ff}} = \omega_0$. In this case, the offset is zero and the effective field is collinear with the B_1 field in the rotating frame, $B_{\text{eff}} = B_1$.

The maximal NMR signal can be detected when the magnetization vector evolves in the transverse plane. However, two types of relaxation rebuilt the longitudinal magnetization back to the Boltzmann distribution and diminish the transverse magnetization. The first mechanism is called spin-lattice relaxation, since it accomplishes the population changes across the Zeeman transitions via energy exchange between the spin system and its surrounding. It is characterized by the longitudinal relaxation rate constant, R_1 . The second mechanism is the spin-spin relaxation due to dephasing of the nuclear magnetic moments over time, with the transverse relaxation rate, R_2 . More details concerning relaxation processes are given in the respective chapter. Using these parameters, the evolution of magnetization in a magnetic field can be expressed by the Bloch equations in the rotating reference frame:

$$\frac{d}{dt} \mathbf{M}(t) = \begin{bmatrix} -R_2 & -\Omega & \omega_1 \sin \phi \\ \Omega & -R_2 & -\omega_1 \cos \phi \\ -\omega_1 \sin \phi & \omega_1 \cos \phi & -R_1 \end{bmatrix} \mathbf{M}(t) + R_1 M_0 \begin{bmatrix} 0 \\ 0 \\ 1 \end{bmatrix} \quad (2.17)$$

In common pulsed NMR experiments, both B_1 and ϕ can be considered independent of time. Furthermore, for short pulses ($\tau_p \ll 1/R_1$ and $1/R_2$) the relaxation rate constants vanish, so that the solution to the Bloch equations can be represented as a series of rotations of the initial magnetization,

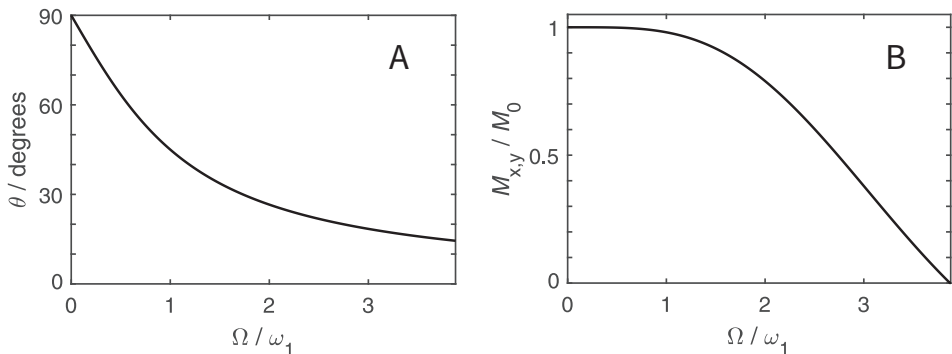


Figure 2.1: Off-resonance effects of a rectangular pulse with nominal $\alpha = 90^\circ$. Shown are (A) the tilt angle of the effective field and (B) the relative magnitude of the transverse magnetization depending on the relative offset.

$$\mathbf{M}(\tau_p) = \mathbf{R}_z(\phi)\mathbf{R}_y(\theta)\mathbf{R}_z(\alpha)\mathbf{R}_y(-\theta)\mathbf{R}_z(-\phi)\mathbf{M}(0) \quad (2.18)$$

where \mathbf{R}_y and \mathbf{R}_z are rotation matrices in the usual definition. $\mathbf{M}(\tau_p)$ thus gives the effect of rf pulses on the magnetization of isolated spins under the stated conditions. In the so-called acquisition time after a pulse, the precessing transverse magnetization will generate the recordable signal, damped by an exponential factor $\exp(-R_2t)$. The NMR signal is therefore referred to as free induction decay (FID).

In practice, nuclei of a spin ensemble will have different Larmor frequencies due to their chemical shifts (see below) and therefore will not all be on-resonant to the carrier frequency of a pulse. For nuclei with $\omega_0 \approx \omega_{rf}$, the effective field is similar to B_1 , but further off-resonance, the effective field will be tilted away from the intended x - y plane. For a pulse of y -phase applied to equilibrium z -magnetization of magnitude M_0 , Eq. (2.18) results in

$$\begin{aligned} M_x &= M_0 \sin \alpha \sin \theta \\ M_y &= M_0(1 - \cos \alpha) \sin \theta \cos \theta \\ M_z &= M_0(\cos^2 \theta + \cos \alpha \sin^2 \theta) \end{aligned} \quad (2.19)$$

The amplitude of the resonance signal is given by the transverse magnetization, $M_{x,y} = \sqrt{M_x^2 + M_y^2}$. The dependency of the magnetization on the offset is shown in Figure 2.1B. It remains approximately constant as long as the offset is small compared to the pulse field strength. At larger offsets, the signal decreases until it disappears.

In the $R_{1\rho}$ relaxation dispersion experiments which are used in this thesis and presented further below, so called spin-lock pulses are utilized to keep the magnetization at a tilted position. In the on-resonance approach, these pulses are aimed for inducing a tilt angle $\theta = 90^\circ$, so that off-resonance effects are negligible at the beginning of the spin-lock period. This can be examined in Fig. 2.1 and is achieved by adjusting ω_{rf} to the respective Larmor frequency.

Theoretical Considerations

Since the Bloch model itself is strictly limited to noninteracting nuclei, further concepts are required to thoroughly describe the evolution of a spin system through a NMR pulse sequence. Such concepts are provided by quantum mechanics and will be briefly introduced in this chapter.

The expectation value of a physically observable quantity A can be expressed using its corresponding operator, \mathbf{A} , in Dirac (bra-ket) notation as

$$\langle A \rangle = \langle \Psi | \mathbf{A} | \Psi \rangle \quad (2.20)$$

where Ψ is the wavefunction containing all information about the state of the given system. It can be written as a superposition of orthonormal time-independent ket vectors,

$$|\Psi\rangle = \sum_{n=1}^N c_n |n\rangle \quad (2.21)$$

with c_n being complex amplitude factors. For a single spin-1/2 nucleus the basis kets will be eigenfunctions of the angular momentum operator for the two Zeeman energy states, denoted α and β . The wavefunction of the spin is a superposition of the two, $|\Psi\rangle = c_\alpha |\alpha\rangle + c_\beta |\beta\rangle$. Since distinct wavefunctions are difficult to specify for complex systems like macromolecules in a protein solution, these systems are divided into the ensemble of nuclear spins and the lattice covering all other degrees of freedom. The expectation value of the property A of the sample can then be defined by averaging over all molecular subensembles,

$$\langle \bar{A} \rangle = \sum_{nm} \overline{c_n c_m^*} \langle m | \mathbf{A} | n \rangle \quad (2.22)$$

The ensemble average of coefficients is a matrix which is used to define the density operator σ , so that $\overline{c_n c_m^*} = \sigma_{nm} = \langle n | \sigma | m \rangle$. The diagonal matrix elements of σ are real, positive numbers that represent the population of the state $|n\rangle$, and the off-diagonal elements represent coherent superpositions between two eigenstates, which signifies that phase relationships between different states can be created. The time evolution of σ is needed to assess the expectation value of an NMR observable and is described by the Liouville–von Neumann equation:

$$\frac{d}{dt}\sigma(t) = -i[\mathcal{H}, \sigma(t)] \quad (2.23)$$

The solution to Eq. (2.23) describes the transformation of the initial density operator to a new operator σ' as a rotation under the effect of a time-independent Hamiltonian, \mathcal{H} , and is given by

$$\sigma' = e^{-i\mathcal{H}t} \sigma e^{i\mathcal{H}t} \quad (2.24)$$

The density operator can be constructed as a linear combination of orthogonal basis set operators, for which the Cartesian angular momentum operators can be used. Two examples from the basis set that are important to follow the evolution of operators in the relaxation dispersion experiment are the single-element basis operator for the α state, $I^\alpha = |\alpha\rangle\langle\alpha|$, and the the z -component of the spin angular momentum (Eq. (2.2)) expressed as $I_z = \frac{1}{2}(|\alpha\rangle\langle\alpha| - |\beta\rangle\langle\beta|)$. When a nuclear spin is weakly coupled to a similar spin S , the two-spin system has four eigenstates according to all possible combinations of its magnetic quantum numbers, as outlined below. The angular momentum then becomes a product operator, $I_z = \frac{1}{2}(|\alpha\alpha\rangle\langle\alpha\alpha| + |\alpha\beta\rangle\langle\alpha\beta| - |\beta\alpha\rangle\langle\beta\alpha| - |\beta\beta\rangle\langle\beta\beta|)$, where the first and second symbol in each eigenstate represents the I and S spin, respectively. The product operator formalism⁵³ allows for calculation of the density operator evolution in weakly coupled systems. If a set of three operators satisfy the commutation relation, $[\mathbf{A}, \mathbf{B}] = i\mathbf{C}$, transformations of the operators are described by

$$e^{-i\theta\mathbf{C}} \mathbf{A} e^{i\theta\mathbf{C}} = \mathbf{A} \cos \theta + \mathbf{B} \sin \theta \quad (2.25)$$

where θ is the rotation angle. In analogy to the case of a single spin angular momentum, the effect of rf pulses and free precession intervals on product operators can thus be calculated conveniently by geometrical arguments.

Spin Interactions

Chemical Shift

In a complex molecule like a protein, the nuclei perceive slightly different magnetic field strengths depending on their local environment. The external magnetic field induces motions of electrons that cause secondary fields, which partially shield the nuclei from the external field. Their resonance frequencies are thus altered from the one predicted by Eq. (2.7). The differences in resonance frequencies allow for differentiation between identical nuclei in different chemical environments and are therefore called chemical shifts. They depend on structural and conformational characteristics such as electrostatic interactions, hydrogen bonding and side chain dihedral angles.^{54,55} The chemical shift of a resonance signal, denoted δ , is defined field-independently in parts per million (ppm) relative to the resonance of a standard molecule as

$$\delta = \frac{\Omega - \Omega_{\text{ref}}}{\omega_0} \cdot 10^6 \quad (2.26)$$

where Ω_{ref} is the offset frequency of the reference resonance signal. In liquid samples with rapid molecular tumbling, the observed chemical shift is the isotropic average of the spatially anisotropic chemical shielding. However, chemical shift anisotropy (CSA) is a source of spin relaxation since the locally induced fields change with molecular rotation.

Aromatic ring systems show relatively large chemical shifts because of the ring-current effect. The external magnetic field induces circular currents in the π -electron cloud which lead to high nuclear shielding close to the surface normal and to an increase of the local fields near the plane of the ring. Typical ^1H and ^{13}C chemical shift values of nuclei in aromatic amino acids are around 6 to 8.5 ppm and 110 to 130 ppm, respectively.

Scalar Coupling

Direct dipole-dipole coupling of nuclear magnetic dipole moments is the most important relaxation mechanism because of the continual change of local magnetic fields in tumbling molecules, but the dipole-dipole spin Hamiltonian averages to zero in isotropic liquids. However, the nuclear magnetic moments interact with each other via the electrons that form chemical bonds between the nuclei. This interaction is therefore named indirect spin-spin coupling, as well as scalar- or J -coupling. For a

spin system consisting of two spins I and S , the J -coupling interaction is described by a scalar product Hamiltonian:

$$\mathcal{H}_J = \omega_I I_z + \omega_S I_z + 2\pi \mathbf{J} \mathbf{I} \cdot \mathbf{S} \quad (2.27)$$

in which J is the isotropic coupling constant expressed in Hz. The hyperfine interaction of each nuclear spin with the electronic magnetic moments modifies the energy levels of the two-spin system. Thus, the respective resonance signal of I is split into $2S + 1$ lines, and the resonance of S into $2I + 1$ lines. In the weak coupling limit, fulfilled when $|\omega_I - \omega_S| \gg 2\pi J$, the four wavefunctions describing the system are eigenfunctions of \mathcal{H}_J , representing independent energy levels. The weak coupling Hamiltonian then simplifies to $\mathcal{H}_J = \omega_I I_z + \omega_S I_z + 2\pi J I_z S_z$. Scalar couplings are field-independent and of great importance to transfer magnetization between desired nuclei in NMR pulse sequences.

Residual Dipolar Coupling

In a weakly oriented solvent, for example in the presence of dilute liquid crystalline phases, biomolecules tumble freely but are forced to have a very slight preference for certain orientations. In that case, the distribution of molecule orientations is no longer uniform, and large anisotropic interactions (such as the dipolar coupling, the CSA or the electric quadrupole interaction) are incompletely averaged, giving rise to so-called residual dipolar couplings (RDCs).^{56,57} These couplings provide useful structural information, since they depend on the time-averaged orientation of internuclear vectors with respect to the molecular frame. For a two-spin system such as a carbon nucleus attached to its hydrogen, the residual coupling constant is given by:

$$D_{\text{RDC}} = \frac{1}{2} D_{IS} \left(A_a (3 \cos^2 \vartheta - 1) + \frac{3}{2} A_r \sin^2 \vartheta \cos 2\varphi \right) \quad (2.28)$$

Here, ϑ and φ are the polar angles describing the orientation of the ^{13}C - ^1H vector with respect to the so-called alignment tensor, A , that defines the orientation of the molecule within the laboratory reference frame. A_a and A_r are the axial and rhombic component of the alignment tensor, respectively, and D_{IS} is the dipole-dipole coupling constant,

$$D_{IS} = -\frac{\mu_0}{4\pi^2} \frac{\gamma_I \gamma_S \hbar}{r_{IS}^3} \quad (2.29)$$

in which μ_0 is the vacuum magnetic permeability and r_{IS} is the distance between the two spins. The Hamiltonian in the weak coupling limit, $|\omega_I - \omega_S| \gg 2\pi D_{\text{RDC}}$, is then given by

$$\mathcal{H}_{\text{RDC}} = 2\pi D_{\text{RDC}} I_z S_z \quad (2.30)$$

Thus, the Hamiltonian has the same functional form as the weak scalar coupling Hamiltonian, leading to the fact that in the presence of weak alignment, the experimentally measurable coupling constant is given by $J + D_{\text{RDC}}$.

Chemical Exchange

The reversible transfer of an isolated nuclear spin between different molecular environments is called chemical exchange. When the environments are magnetically distinct, the nucleus will have different resonance frequencies and thus chemical shifts. Hence, the underlying chemical or conformational kinetic process can be monitored by NMR. The simplest situation is a two-site exchange where the scalar coupling constants are not altered. It is described as a reaction between states A and B:



in which k_1 and k_{-1} are the forward and reverse rate constant, respectively. The chemical exchange rate constant, k_{ex} , being a transition probability per unit time, is given by

$$k_{\text{ex}} = k_1 + k_{-1} = k_1/p_{\text{B}} = k_{-1}/p_{\text{A}} \quad (2.32)$$

where p_{A} is the equilibrium population of spins in state A, and $p_{\text{B}} = 1 - p_{\text{A}}$ is the population of equivalent spins in state B. The chemical kinetic rate laws for two-site exchange can be expressed in matrix form as

$$\frac{d}{dt} \begin{bmatrix} [\text{A}](t) \\ [\text{B}](t) \end{bmatrix} = \begin{bmatrix} -p_{\text{B}}k_{\text{ex}} & p_{\text{A}}k_{\text{ex}} \\ p_{\text{B}}k_{\text{ex}} & -p_{\text{A}}k_{\text{ex}} \end{bmatrix} \begin{bmatrix} [\text{A}](t) \\ [\text{B}](t) \end{bmatrix} \quad (2.33)$$

In such a system, the time course of the magnetization under free precession is described by the modified Bloch or McConnell equations.⁵⁸ The evolution of the transverse magnetization at each site, M_{A}^+ and M_{B}^+ , is thus given by

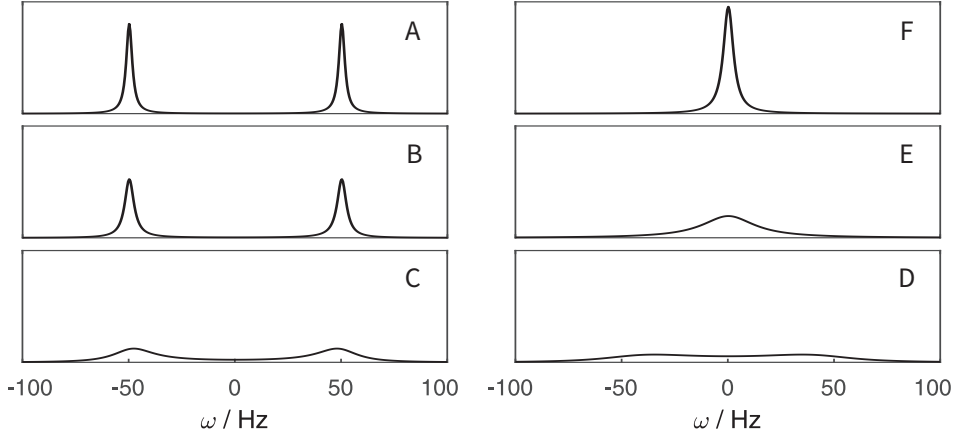


Figure 2.2: Symmetrical two-site exchange. Lineshapes were calculated based on Eq. (2.35) for $k_{\text{ex}}/\Delta\omega = 0.001$ (A), 0.01 (B), 0.1 (C), 0.25 (D), 1 (E), 10 (F). Resonance frequencies of -50 Hz and +50 Hz ($\Delta\omega = 2\pi 100$), equal populations and $R_2^0 = 10 \text{ s}^{-1}$ were used for both sides.

$$\frac{d}{dt} \begin{bmatrix} M_A^+(t) \\ M_B^+(t) \end{bmatrix} = \begin{bmatrix} -i\Omega_A - R_{2,A}^0 - p_B k_{\text{ex}} & p_A k_{\text{ex}} \\ p_B k_{\text{ex}} & -i\Omega_B - R_{2,B}^0 - p_A k_{\text{ex}} \end{bmatrix} \begin{bmatrix} M_A^+(t) \\ M_B^+(t) \end{bmatrix} \quad (2.34)$$

Here, $R_{2,A}^0$ and $R_{2,B}^0$ are the transverse relaxation rates resulting from processes other than chemical exchange, and Ω_A and Ω_B are the resonance frequencies in the rotating frame for spins in states A and B, respectively. The chemical shift difference between the two sites is termed $\Delta\omega = \Omega_A - \Omega_B$. In the generalized case of N chemical reactions between N species, the Bloch-McConnell equations can be equivalently formulated with corresponding $N \times N$ rate matrices.⁵⁹ The solution to Eq. (2.34) describes the transfer of magnetization due to the exchange process in the form of

$$\begin{bmatrix} M_A^+(t) \\ M_B^+(t) \end{bmatrix} = \begin{bmatrix} a_{AA}(t) & a_{AB}(t) \\ a_{BA}(t) & a_{BB}(t) \end{bmatrix} \begin{bmatrix} M_A^+(0) \\ M_B^+(0) \end{bmatrix} \quad (2.35)$$

in which $a_{ij}(t)$ are the exponential transfer amplitudes, which are intricately depending on the aforementioned rate constants and populations. For these lengthy expressions the reader is referred to the literature.^{50,60}

The NMR spectrum of a two-site exchanging system is given by the Fourier transformation of the FID generated by $M_A^+(t) + M_B^+(t)$. Figure 2.2 shows simulated spectra for symmetric unimolecular exchange ($p_A = p_B$). The relative values of k_{ex} and $\Delta\omega$ define the limits of the exchange time regimes, which are referred to as slow exchange ($k_{\text{ex}} < \Delta\omega$), intermediate exchange ($k_{\text{ex}} \approx \Delta\omega$), and fast exchange ($k_{\text{ex}} > \Delta\omega$). In

this context, the term “slow” (“fast”) stands for an infrequently (frequently) occurring event, irrespective of how fast the exchange process itself is.

In Fig. 2.2 the different time regimes are depicted. For slow exchange (spectrum A), two resolved resonance lines are observed for the two states. At increasing k_{ex} , the lines broaden due to enhanced dephasing of the transverse magnetization (spectra B and C), until they coalesce, as shown in spectra D and E. These illustrate the intermediate regime, where the resonance signal might be indistinguishable from the baseline noise. At fast exchange rates, a single line appears at the average resonance frequency, denoted $\bar{\omega}$. As the rate increases further (F), the resonance lineshape becomes narrower until the limit $k_{\text{ex}} \rightarrow \infty$, where the relaxation decay is given by $\bar{R}_2 = p_A R_{2,A}^0 + p_B R_{2,B}^0$.

A textbook example for symmetric exchange processes are 180° rotations of aromatic rings, where the two physically identical ground states are distinguishable by NMR spectroscopy if the molecular vicinity generates different chemical shifts for equivalent nuclei on both sides of the ring. The forward and reverse rate constants are equal and labeled k_{flip} , so that Eq. (2.32) gives $k_{\text{ex}} = 2k_{\text{flip}}$. Due to varying chemical shift differences, ring flip processes of different aromatic residues can be in different exchange regimes even if the flip rates are the same. The processes are therefore of different accessibility to the experiment, despite similar flip rates at given experimental conditions.

In the case of skewed exchange ($p_A \neq p_B$), the intensities of the resolved signals are uneven according to the populations, and with rising k_{ex} the minor signal broadens primarily relative to the major form. The generalized coalescence condition is given by $2\sqrt{p_A p_B} k_{\text{ex}} \approx \Delta\omega$. In the fast exchange regime a single resonance line appears at the population-weighted average shift.

Rotating-Frame Relaxation

Relaxation rates provide information on motions and exchange processes at the atomic scale, because they are due to fast fluctuations of local magnetic fields that are caused by such molecular motions.⁶¹ In an $R_{1\rho}$ relaxation dispersion experiment, as described in the following chapter, the magnetization is spin-locked in the rotating frame via application of a rf field.⁶² $R_{1\rho}$ denotes the relaxation rate constant for the component of the magnetization along the effective field in the rotating frame. In the presence of chemical exchange, this rate constant is constituted of contributions from R_1 and R_2 processes and from the exchange process,⁶³

$$R_{1\rho} = \bar{R}_1 \cos^2 \theta + \bar{R}_2 \sin^2 \theta + R_{\text{ex}} \quad (2.36)$$

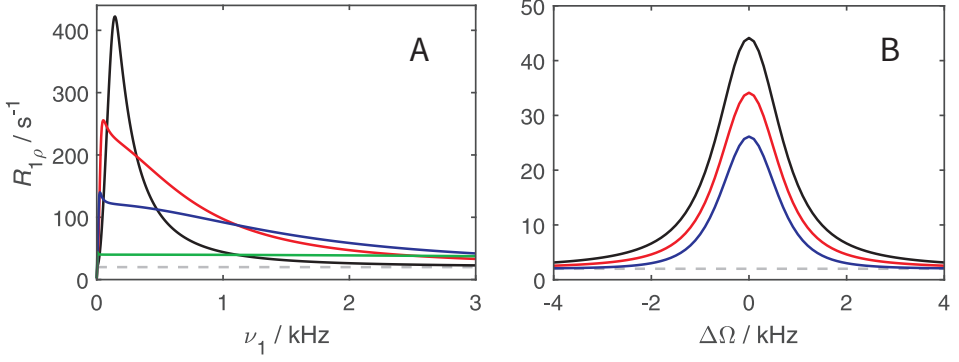


Figure 2.3: Field strength and offset dependence of the $R_{1\rho}$ relaxation rate constant for different values of k_{ex} and \bar{R}_2 , respectively. Calculated with Eqs. (2.36-2.37) using equal populations and $\Delta\omega = 2000 \text{ s}^{-1}$. (A) $R_{1\rho}$ depending on $\nu_1 = \omega_1/(2\pi)$ for $\Delta\Omega = 0$ and $\bar{R}_2 = 20 \text{ s}^{-1}$ (represented as a grey dashed line). Shown are $k_{\text{ex}}/(10^3 \text{ s}^{-1}) = 1$ (black), 5 (red), 10 (blue), 50 (green). (B) Offset dependence of $R_{1\rho}$ for $\nu_1 = 1 \text{ kHz}$, $k_{\text{ex}} = 1 \cdot 10^3 \text{ s}^{-1}$ and $\bar{R}_1 = 2 \text{ s}^{-1}$ (grey dashed line). Depicted are $\bar{R}_2/(s^{-1}) = 20$ (black), 10 (red), 2 (blue).

where \bar{R}_1 and \bar{R}_2 are population-average values, θ is the tilt angle of the effective field, and R_{ex} is the relaxation contribution due to chemical exchange broadening. The different contributions can be separated from each other under realistic experimental conditions, where the correlation time for overall rotational diffusion of the molecule, $\tau_c \ll k_{\text{ex}}^{-1}$, and $\bar{R}_2 - \bar{R}_1 \ll k_{\text{ex}}$ is satisfied.⁶⁴ Depending on the exchange time regime and the relative populations, different expressions for R_{ex} are valid. These have been derived from the Bloch-McConnell evolution matrix or the evolution of the average density operator of the spin system. Approximations are available for the fast exchange limit^{65,66} as well as for motional time scales outside this limit, provided that the site populations are not equal.⁶⁷ For symmetric exchange (equal populations) and for the case that the carrier frequency is placed at the numerical average resonance frequency of the sites, Miloshev and Palmer derived the general expression⁶³

$$R_{\text{ex}} = \frac{k_{\text{ex}}}{2} - \frac{k_{\text{ex}}}{2} \sqrt{1 - \frac{4 \sin^2 \theta p_A p_B \Delta\omega^2}{\omega_A^2 \omega_B^2 / \omega_{\text{eff}}^2 + k_{\text{ex}}^2 - \sin^2 \theta p_A p_B \Delta\omega^2 \frac{k_{\text{ex}}^2 (\omega_A^2 + \omega_B^2)}{\omega_A^2 \omega_B^2 + \omega_{\text{eff}}^2 k_{\text{ex}}^2}}}} \quad (2.37)$$

Here, ω_A and ω_B are the effective field strengths at the resonance frequency of each site given by $\omega_i = \sqrt{\Omega_i^2 + \omega_1^2}$. The tilt angle $\theta = \tan^{-1}(\omega_1/\Delta\Omega)$ using the average offset from the carrier, $\Delta\Omega = \bar{\omega} - \omega_{\text{rf}}$, and the respective effective field strength $\omega_{\text{eff}} = \sqrt{\Delta\Omega^2 + \omega_1^2}$ (cf. Eqs. (2.13-2.15)).⁶⁸

At the beginning of a spin-lock period, the magnetization is aligned with the effective field. Due to the exchange process, the offset component of the field and thus the tilt

angle changes by the difference of chemical shifts of the two states, and ensemble magnetization aligned along the initial effective field is gradually lost.⁶¹ At higher effective fields (larger offsets or rf field strengths), the change of the tilt angle becomes smaller and the exchange contribution to relaxation is quenched more efficiently. Therefore, the exchange parameters can be extracted from the characteristic dependence of $R_{1\rho}$ on the effective field.⁶² Figure 2.3A illustrates such $R_{1\rho}$ relaxation dispersion curves for symmetrical exchange in the on-resonance case, given by a fixed $\omega_{\text{rf}} = \bar{\omega}$. The \bar{R}_1 contribution in Eq. (2.36) vanishes because of the tilt angle $\theta = 90^\circ$, and the observed $R_{1\rho}$ rate constant is dominated by the contributions from transverse relaxation and the exchange process. $R_{1\rho}$ approaches the constant value of \bar{R}_2 for field strengths $\omega_1 \rightarrow \infty$. The relaxation decay is more pronounced for slower k_{ex} . In Eq. (2.37) the chemical shift difference $\Delta\omega$ appears in a product with the populations. They can only be deconvoluted by use of ancillary information, as in case of aromatic ring flips where the populations are known to be 0.5 each. The steep decrease of $R_{1\rho}$ at very low field strengths is of theoretical origin and of no relevance for the experiment. Under realistic experimental conditions it always appears at frequencies much lower than those needed for tilting of the effective field, as described below.

In the off-resonance $R_{1\rho}$ approach, the effective field is changed by variation of the carrier frequency ω_{rf} at a fixed or varied ω_1 , so that different offsets and tilt angles are obtained. Fig. 2.3B shows that the transverse relaxation rate determines the maximum $R_{1\rho}$ relaxation rate, which decreases with increasing offset and approaches the constant \bar{R}_1 as $\theta \rightarrow 0$. Pronounced dispersion steps are therefore measured preferably on-resonance, especially for high exchange rates.

The $R_{1\rho}$ Relaxation Dispersion Experiment

Since dynamical processes of biomacromolecules take place on highly diverse time scales ranging from picoseconds up to seconds, different solution-state NMR methods are applicable for their investigation.¹⁰ For kinetic processes and conformational dynamics on the microsecond to second time scale, Carr-Purcell-Meiboom-Gill (CPMG) and $R_{1\rho}$ relaxation dispersion experiments are the most advantageous heteronuclear NMR techniques.^{10,60}

Figure 2.4 shows a pulse sequence for ^{13}C $R_{1\rho}$ relaxation measurements on aromatic side chains,⁶⁹ which is used in all studies of the present thesis for the determination of ring flip exchange parameters. Therefore this chapter will particularize its components and features, explaining specific rationales in subchapters while following the time course of the pulse sequence.

At the beginning, a 90° hard pulse on the ^{13}C channel followed by a pulsed field gradient (PFG) clear up possible carbon transverse magnetization. Thus all detected

^1H spins. Their magnetization state affects the efficiency of the relaxation, which in turn defines the sensitivity of such experiments.⁷⁴ Therefore it is important that the water and aliphatic magnetization is maintained along the $+z$ -axis to provide a steady thermal bath for relaxation of the aromatic ^1H spins.⁷⁵ Suppression of the excessive solvent signal is accordingly achieved. The L-optimization is implemented by selective E-BURP2 pulses⁷¹ acting as flip-back pulses for the water and aliphatic magnetization.⁷⁶ They are indicated as narrow semi-ellipses in Fig. 2.4.

Spin State Selection

Further improvement of sensitivity and relaxation is accomplished by reducing transverse relaxation of the desired coherences using Transverse Relaxation Optimization Spectroscopy (TROSY).⁷⁷ As mentioned above, a heteronuclear two-spin system shows a multiplet of resonance signals due to the J -coupling, unless one species is decoupled by respective rf fields. The signals corresponding to the ^1H spin states α and β will be affected differently by transverse relaxation caused predominantly by the CSA and direct coupling between ^1H and ^{13}C . These cross-correlated interactions affect the local magnetic field at the ^{13}C nucleus with different signs, interfering constructively for one ^1H spin state and destructively for the other. The relaxation of the ^{13}C magnetization is thus enhanced or reduced depending on the spin state and R_2 relaxation of the attached proton. In contrast, the contribution of CSA to aromatic ^1H is neglectable. Since the transverse relaxation rate determines the linewidth of a resonance signal, one multiplet component is considerably broadened while the other is narrowed. The extent of the narrowing depends on the static magnetic field that makes the CSA relaxation mechanism competitive with the dipole-dipole relaxation. For a 14.1 T field as exploited in this thesis, the effect on aromatic spins is nearly optimal as can be calculated from the chemical shielding tensor for aromatic compounds.^{75,78}

TROSY-detected $R_{1\rho}$ pulse sequences take advantage of the narrowing effect by tracking the slowly decaying coherence only.^{11,79} This results both in reduced linewidths of the detected signals and in a reduced \bar{R}_2 in the $R_{1\rho}$ relaxation dispersion profile. In the present case, the narrow doublet component is selected using a heteronuclear S^3E element⁸⁰ (Fig. 2.4 B), which excites only the resonances corresponding to the α spin state of the aromatic protons. Hereby $I_z S_z$ magnetization is converted into $I^\alpha S_z$.

The Relaxation Period

Figure 2.4 section C contains the relaxation period, t_{sl} , which is divided into two parts of equal length. In each block, the narrow TROSY component of the carbon magnetization is aligned along the effective field using an adiabatic rf pulse,⁷² spin-locked on-resonance with a continuous-wave rf field and returned to the z -axis with a time-reversed adiabatic pulse. Such pulses sweep the effective rf field over a certain frequency range by simultaneous amplitude and phase modulation. The magnetization vector is forced to follow, provided that the adiabatic condition, $|d\theta/dt| \ll \omega_{eff}$, is fulfilled. Adiabatic ramps then yield accurate alignment and avoid oscillatory behaviour of mismatched magnetization.⁷² The duration of the sweeps is restricted to 4 ms to avoid large relaxation losses, which enables field strengths of 1 kHz or higher. Other approaches for alignment with the effective field are based on chemical shift precession⁸¹ or utilize specific pulse schemes.⁸²

During both parts of the spin-lock period, $R_{1\rho}$ relaxation evolves due to exchange processes. However, interference of the direct ^1H - ^{13}C coupling and the CSA would lead to cross-relaxation of the different TROSY components and distort the $R_{1\rho}$ rate constant measured on the narrow component.⁸³ The cross-relaxation is therefore suppressed while simultaneously decoupling the ^1H scalar coupling interactions by inverting the sign of $I^\alpha S_z$ in the middle of the period. This selective ^1H inversion is realized by a $S^3\text{CT}$ element.⁸⁴ It uses composite pulses on ^1H ($90_x 180_y 90_x$) superior to conventional ^1H 180° pulses which can lead to incomplete decoupling and overestimation of the relaxation rate constants in $R_{1\rho}$ experiments.^{85,86}

The final part of the pulse sequence (Fig. 2.4 D) prepares for the measurement of a heteronuclear 2D NMR spectrum of the narrow TROSY component. During the evolution period, t_1 , ^{13}C chemical shift evolves from the antiphase heteronuclear coherence, $I_z S_x$. In a number of experiments with incremented t_1 , the carbon nucleus is frequency labeled so that its frequency can be extracted from the final FID by Fourier transformation. The remaining pulses and delays accomplish magnetization transfer back to the protons. This is done in a PEP (preservation of equal pathways) fashion, where both the sin and cos components of the chemical shift evolution are transferred to detectable I_y magnetization at the beginning of the acquisition period. The FID is collected during t_2 , while scalar coupling evolution is suppressed by heteronuclear decoupling. This is realized by applying a GARP sequence⁷³ on the ^{13}C channel, which uses a series of composite 180° pulses to average the scalar couplings to zero. The overall pulse sequence is repeated not only with regard to different spin-lock field strengths and incrementation of t_1 , but also with combined phase cycling of pulses, the receiver and field gradients to exclude all unwanted coherence pathways.

The $R_{1\rho}$ relaxation rate can be calculated from the intensity of the respective resonance signal according to⁸⁷

$$R_{1\rho} = -\ln(I_{\text{relax}}/I_0)/t_{\text{sl}} \quad (2.38)$$

where I_{relax} and I_0 are the intensities measured with and without a spin-lock period of duration t_{sl} , respectively. Both intensities have to be measured for all ω_{eff} individually to account for the relaxation losses during the adiabatic sweeps,^{82,88} which are present also when measuring without the spin-lock.

Relaxation dispersion experiments that are carried out on uniformly ^{13}C enriched aromatic side chains encounter problems from scalar coupling interactions between neighbouring atoms. During relaxation periods, large one-bond or higher order J -couplings can give rise to magnetization transfer that cause artifacts in the relaxation dispersion profiles.^{89,90} Strong ^1H - ^1H or ^{13}C - ^{13}C couplings emerge when the chemical shift difference between the two nuclei is not sufficiently larger than the coupling constant, which is likely to be the case in aromatic rings.⁹¹ Additionally, Hartmann-Hahn transfer of magnetization can occur between coupled nuclei during ^1H or ^{13}C irradiation, depending on the coupling constants and the spin-lock field strength.^{92,93} This phenomenon is analyzed in detail in Paper II of this thesis. To avoid magnetization transfer between scalar coupled nuclei and aberrant relaxation pathways, site-specific labeling of proteins is used.^{94,95} Thus isolated ^1H - ^{13}C spin pairs are obtained that are devoid of scalar couplings to similar nuclei. Since the labeling schemes do not provide complete enrichment of the protein samples, the increased accuracy of the relaxation dispersion experiment goes along with a decrease in sensitivity. Sensitivity enhancement by the combination of L-optimization with the TROSY approach is therefore of high advantage.⁹⁶ This holds especially for large proteins since the transverse relaxation rate increases with protein size, and for systems that suffer significantly from chemical exchange, like aromatic rings undergoing flipping motions (see Fig. 2.2).

Some Practical Aspects

The time scale of exchange processes that can be studied by relaxation dispersion experiments is determined by the accessible range of effective magnetic field strengths.¹⁴ Due to the large effective fields of 1 to 6 kHz, $R_{1\rho}$ relaxation experiments are applicable for processes with a lifetime of 10 μs to 1 ms, whereas CPMG experiments cover processes with $1/k_{\text{ex}} \approx 1$ ms to 10 ms.⁶¹ In a CPMG relaxation experiment, relaxation of transverse magnetization is observed during a series of spin-echo pulses of frequency ν_{cp} . In the limit of fast exchange, it can be considered an on-resonance rotating frame experiment with low effective field strength $\omega_{\text{eff}} = \sqrt{48}\nu_{\text{cp}}$.⁹⁷ Principal advantages of $R_{1\rho}$ over CPMG experiments are the wider range of accessible exchange rates, a possible complete characterization of exchange processes at a single magnetic

field by combination of the on- and off-resonance approaches, and the potential to obtain the absolute sign of chemical shift changes outside the fast-exchange limit.^{14,67} Major experimental limitations are set to the methods by the maximum ω_{eff} that is achievable by the probe head and amplifiers, and sample heating at high effective fields or pulsing rates, respectively. Nevertheless, weak-field $R_{1\rho}$ experiments⁸⁶ as well as CPMG experiments with high pulse rates⁹⁸ are also objects of development. To set the effective field on-resonance on a desired aromatic nucleus, its chemical shift is measured in a TROSY two-dimensional NMR spectrum prior to the relaxation dispersion experiment. Accurate calibration of the effective field strength is performed by measuring a 2D NMR experiment with continuous-wave decoupling during the acquisition period.⁹⁹ The decoupling frequency is set off-resonance with respect to a selected signal, so that a reduced scalar-coupling constant, $J_{\text{eff}} = J \cos \theta$, can be measured. The tilt angle and thus the effective field strength can be calculated from $\tan \theta = \sqrt{(J/J_{\text{eff}})^2 - 1}$ by comparison to an experiment without decoupling.⁶⁰

Chapter 3

Energetics of Protein Fluctuations

The dynamic properties of proteins are directly related to their biological function. Often the biological activity goes in hand with the adoption of different conformational states on a broad range of magnitudes and time scales.^{4,15} During the history of protein science it was concurrently observed that these molecules undergo fluctuations in thermodynamic properties while exhibiting distinct structural features.¹⁰⁰ To fully understand the conformational fluctuations of proteins it is necessary to study the free energy differences and barriers between the different states. Rotational motions of symmetric aromatic rings in the interior of globular proteins are unique reporters on transient structural fluctuations and allow to determine the associated activation parameters. In this chapter, the characteristics of aromatic ring flips and the concept of activation energy barriers will therefore be introduced. The compressibility of proteins as a particular thermodynamic characteristic demonstrates the complex correlation of diverse volume fluctuations in protein solutions.

Aromatic Ring Flips

Four of the 20 amino acids in proteins are aromatic amino acids, namely phenylalanine (Phe, F), tyrosine (Tyr, Y), tryptophan (Trp, W) and histidine (His, H). The structures of the former two are shown in Figure 3.1. They possess a symmetric six-ring side chain structure which can perform 180° jumps around the χ_2 dihedral angle or imaginary C_β - C_γ - C_ζ axis. So called ring flips were observed for the first time in 1975 using ¹H NMR spectroscopy,^{8,9} which dramatically changed our understanding of the very nature of proteins as dynamic systems and not static objects.^{101,102} For aromatic side chains buried in the interior of a protein, the flipping motions are

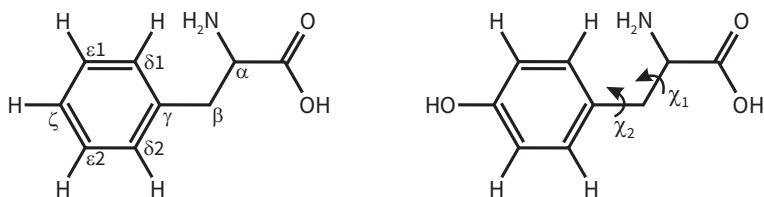


Figure 3.1: Structure of aromatic amino acids. *Left:* Phenylalanine¹¹² with Greek letter nomenclature of carbon positions.¹¹³ *Right:* Tyrosine¹¹⁴ with indication of the side chain dihedral angles.

characterized by two symmetry-equivalent ground states of the ring and the transition state encountered when χ_2 is rotated by 90° . Fig. 3.2A illustrates how the ring planes are oriented perpendicular to each other in the ground state and the transition state. The orientation of the ground state and the free energy barrier for flipping are determined by the interactions in which the aromatic rings are involved.

Due to their hydrophobicity, Phe and to a lesser degree Tyr are often excluded from the solvent and buried in the hydrophobic core of a protein together with other non-polar side chains, thereby contributing to the protein stability.¹⁷ Phe, Tyr and Trp aromatic residues have a quadrupolar electrostatic character originating from the cloud of delocalized π electrons, which enables a large number of aromatic interactions.¹⁰³ They can interact with cations^{104,105}, sulfur¹⁹, hydrocarbons¹⁰⁶ and serve as acceptors for weak hydrogen bonds.¹⁸ Most notably, aromatic-aromatic stacking interactions are essential for the structure and interplay of biomolecules.¹⁰⁷ On average 60% of the aromatic side chains in proteins are involved in π - π interactions, most of them forming networks containing three or more aromatic residues.¹⁰⁸ The interaction energies are on the order of the free energy of protein folding (up to 10 kJ/mol per pair of rings)^{108,109} and mainly governed by electrostatic and van der Waals contributions.¹¹⁰ A parallel-displaced arrangement of two rings and a T-shaped edge-to-face geometry are found to be the most preferred orientations.¹¹¹

In order for rotational motions of side chains buried in the densely packed interior of proteins to occur, the surrounding has to undergo substantial conformational changes.¹¹⁵ Such fluctuations of the folded structure are referred to as “breathing motions” of a protein, since they provide the activation volumes required for the ring flip to occur. The flip rates of aromatic rings exposed at the surface of proteins can be 10^6 s^{-1} or even higher, whereas for rings buried in the interior, the flip rates can be slower by several orders of magnitude.¹¹⁶ The Phe and Tyr rotational motions are then called slow ring flips and their ground states are well-defined with residence times on the order of μs to ms. Since ring flips dynamics are directly connected to the local conformational fluctuations, they serve as valuable probes reporting on the interior of folded globular proteins. The lineshape of NMR signals of the ring carbons and protons are affected by the rotational exchange process if the chemical shifts are different on both sites of the ring (δ_1 and δ_2 , or ϵ_1 and ϵ_2 , Fig. 3.1), which they often are.⁷⁰

Ring flips can therefore be detected with NMR, while protein X-ray crystallography and other methods only examine a time-averaged protein structure.⁹ They are unable to distinguish the two orientations of the ring and hence to detect ring flips.

Although the value of aromatic ring flips for probing protein structural flexibility has been recognized already nearly 50 years ago, only a limited number of systems has been reported where flip rates or activation parameters have actually been measured.¹¹⁷ Yet there has been an awakening interest in the last years because of methodological improvements such as isotope labeling and NMR experiments which are no longer restricted to ring flips in the slow exchange regime.^{94,118} The first ring flip rates were measured on hen lysozyme,⁹ horse ferricytochrome c^{119,120} and BPTI,^{8,101,121} which has been revisited several times.^{115,122,123,124} Likewise, ring flips in iso-2-cytochrome c,¹²⁵ xylanase,¹²⁶ FKBP12^{127,128} and lately a SH3 domain¹²⁹ were examined. Pressure- and temperature-dependent studies were performed only on BPTI,^{130,131} HPr¹¹⁶ and ubiquitin.¹³² Solid-state NMR revealed aromatic ring flips in protein crystals of enkephalin,¹³³ HP36,¹³⁴ GB1 and LC8,¹³⁵ the TET2 enzyme¹³⁶ and ubiquitin.¹³⁷ Furthermore, fast ring flips can be observed in MD simulation studies such as on barstar²⁰, and slow ring flips were examined in a long-time simulation study on BPTI.^{138,139}

Transition-State Theory and Activation Parameters

The rate constant of a ring flip process is a function of temperature and pressure as determined by the thermodynamic characteristics of the transition process. The energy, entropy and volume of activation can be obtained from this dependency by use of the transition-state theory. It describes reaction rate constants in terms of thermodynamic parameters and was developed mainly in 1935 by Henry Eyring¹⁴⁰ as well as Evans and Polanyi.¹⁴¹ The basic idea is that in a chemical reaction, an initial system of low potential energy transforms into a final state via formation of a transition state with high potential energy. The reaction rates can be calculated by focusing on the transient states lying in the vicinity of the top of the energy barrier, using equilibrium theory and statistical mechanics.¹⁴² In the case of an aromatic ring flip reaction, the energy profile has the form showed in Fig. 3.2B, where the initial and the final conformation are structurally and energetically indistinguishable.⁹ The principles of the transition-state theory shall be outlined here for the case of a more general chemical reaction, following the textbooks by McQuarrie and Simon¹⁴³ and Atkins and de Paula.¹⁴⁴

A bimolecular reaction of two species A and B forming a product C can be modeled by a two-step process in which the reactants first form an activated complex, AB[‡]. The reaction equation can be written as

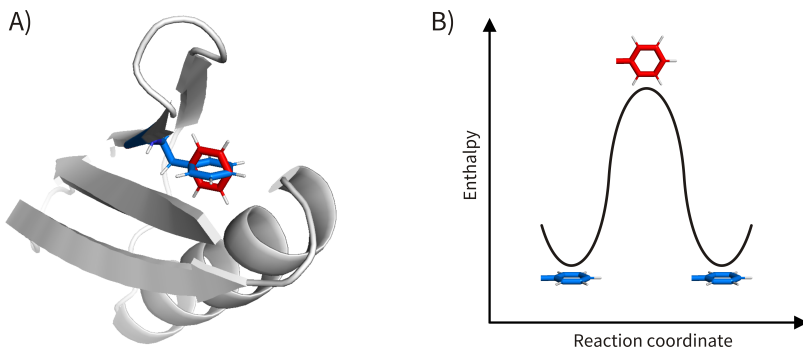


Figure 3.2: Ring flips of aromatic amino acids. (A) Illustration of aromatic ring flipping of F52 in protein GB1. Carbon bonds of the ground state are depicted in blue, of the transition state in red. Hydrogen atoms are indicated as grey sticks. The backbone of the protein is shown in ribbon representation. (B) Schematic energy profile of a ring flip process. The ground states and the transition state are labeled in analogy to (A).



with the reaction rate constant k . The reactants are proposed to be in equilibrium with the activated complex, which can be identified with the transition state. Hence the transition-state theory is also known as activated-complex theory. The equilibrium constant is given by

$$K^\ddagger = \frac{[AB^\ddagger]c^\circ}{[A][B]} \quad (3.2)$$

Here, c° is the standard-state concentration which in the following is set to 1 mol/L for simplicity. The concentrations of the different species can be written in terms of molecular partition functions, which contain all thermodynamic properties of a system. They are defined as $q(V, T) = \sum_i e^{E_i/k_B T}$, where E_i are the possible energy states of a molecule. These are composed of contributions from all translational, vibrational and rotational degrees of freedom. Using q/V which are functions of the temperature only, the equilibrium constant can be rewritten as

$$K^\ddagger = \frac{(q^\ddagger/V)}{(q_A/V)(q_B/V)} \quad (3.3)$$

where q_A , q_B and q^\ddagger are the partition functions of A, B and AB^\ddagger , respectively. For the formation of the final product C, the activated complex has to be tipped over the energy barrier. This is traced by change of one of the degrees of freedom of the transition state. One possible approach is to consider the crossing of the barrier top

induced by a one-dimensional translational motion of the activated complex. The rate law for the formation of C can then be expressed not only in terms of the forward rate constant, but also of the frequency with which the transition state crosses the barrier, ν , so that

$$\frac{d}{dt}[C] = k[A][B] = \nu[AB^\ddagger] = \nu[A][B]K^\ddagger \quad (3.4)$$

which gives $k = \nu K^\ddagger$. The partition function of the transition state needs to be split up into $q^\ddagger = q_{\text{trans}}\bar{q}^\ddagger$, where q_{trans} accounts for the translational motion and \bar{q}^\ddagger covers all other degrees of freedom. The former is given by

$$q_{\text{trans}} = \frac{(2\pi m^\ddagger k_B T)^{1/2}}{h} \delta \quad (3.5)$$

where m^\ddagger is the mass of the activated complex, h is the Planck constant and δ is a small variation of the reaction coordinate around the activation barrier top, where the activated complex is assumed to be stable. The reaction coordinate is a theoretical collection of all motions proceeding during a reaction, such as changes in interatomic distances and bond angles. The variables ν and δ are not well-defined and difficult to determine, but their product gives the average speed with which the activated complex crosses the barrier, denoted $\langle v \rangle = \nu \delta$. Since the reactants and activated complex are in equilibrium, the speed is given by a one-dimensional Maxwell-Boltzmann distribution. Integration over all complexes that pass the barrier towards the final state leads to

$$\langle v \rangle = \left(\frac{k_B T}{2\pi m^\ddagger} \right)^{1/2} \quad (3.6)$$

Using equations (3.3), (3.5) and (3.6), the reaction rate constant can thus be expressed as

$$k = \frac{k_B T}{h} \frac{(\bar{q}^\ddagger/V)}{(q_A/V)(q_B/V)} = \frac{k_B T}{h} \bar{K}^\ddagger \quad (3.7)$$

where \bar{K}^\ddagger is the equilibrium constant with one degree of freedom discarded. Yet by definition it can be expressed in terms of a Gibbs free energy of activation,

$$\Delta^\ddagger G = -RT \ln \bar{K}^\ddagger \quad (3.8)$$

which denotes the change of Gibbs free energy when going from the reactants to the transition state at standard conditions. R is the molar gas constant. Δ^\ddagger signifies the difference between a transition state and the ground state, and it should be mentioned that the positioning of the \ddagger sign is not consistent throughout the literature. Representing the rate constant as a function of the free energy barrier is known as the Eyring equation:

$$k = \frac{k_{\text{B}}T}{h} e^{-\Delta^\ddagger G/RT} \quad (3.9)$$

The Gibbs free energy of activation is composed of the enthalpy of activation, $\Delta^\ddagger H$, and the entropy of activation, $\Delta^\ddagger S$, according to

$$\Delta^\ddagger G = \Delta^\ddagger H - T\Delta^\ddagger S \quad (3.10)$$

At constant temperature, the volume of activation, denoted $\Delta^\ddagger V$, can additionally be derived from the Gibbs free energy of activation by taking its partial derivative with respect to pressure. In conclusion, the Eyring equation can be represented in a temperature and pressure dependent form as¹¹⁶

$$k = \frac{k_{\text{B}}T}{h} e^{-\frac{\Delta^\ddagger H}{RT} + \frac{\Delta^\ddagger S}{R} - p\frac{\Delta^\ddagger V}{RT}} \quad (3.11)$$

The activation parameters can thus be extracted from the reaction rates when measured as a function of temperature and pressure. In the semilogarithmic plot in Fig. 3.3A the rate is represented as a linear function of inverse temperature. Here it can be seen that an increase in $\Delta^\ddagger H$ shifts the rate function to lower values with a higher slope. Increasing $\Delta^\ddagger S$ ($\Delta^\ddagger V$) leads to a parallel shift towards higher (lower) rates. When the rates are displayed as a function of pressure, the slope is given by the activation volume, as shown in Fig. 3.3B.

Returning to the case of ring flip kinetics, the meaning of the introduced parameters can be explained qualitatively. The rate constant defined for the forward direction of a process can be equated with k_{flip} , since the flipping process is structurally symmetric. $\Delta^\ddagger H$ corresponds to the energy which is required for the protein structure around a ring to reorganize and to create space for the rotation.¹¹⁶ Noncovalent and steric interactions with neighbouring atoms constituting the minimum energy ground state that have to be altered and repulsive interactions from the ring atoms with their environment occasion energetic costs.¹⁴⁵ The enthalpy of activation is therefore positive and it is provided by thermal energy fluctuations. $\Delta^\ddagger S$ is also found to be positive

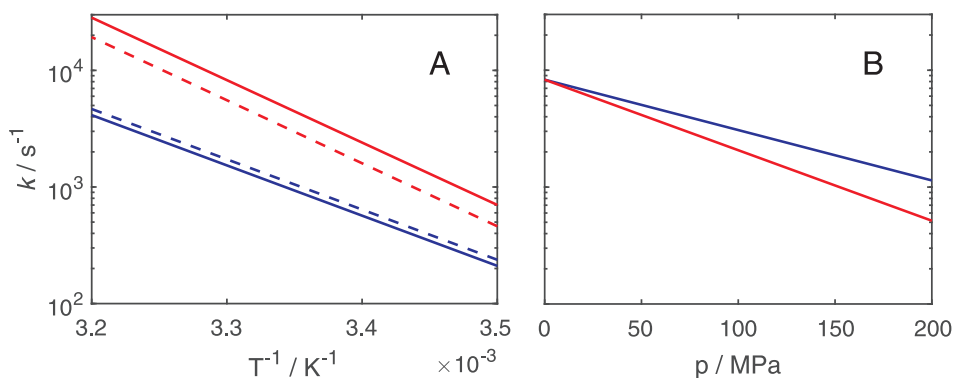


Figure 3.3: Temperature and pressure dependence of reaction rate constants. Calculated with the Eyring equation (3.11) and shown on a logarithmic y-axis. (A) Reaction rates as a function of $1/T$ (temperatures between 283 and 313 K) using a fixed $\Delta^\ddagger H = 80$ kJ/mol with $\Delta^\ddagger S = 80$ and 81 J/mol/K (straight and dashed blue lines, respectively), or a fixed $\Delta^\ddagger S = 160$ J/mol/K with $\Delta^\ddagger H = 100$ and 101 kJ/mol (straight and dashed red lines, respectively). $\Delta^\ddagger V$ was set to 25 ml/mol at ambient pressure. (B) Reaction rates as a function of p using $\Delta^\ddagger V = 25$ ml/mol (blue) and 35 ml/mol (red) with $T = 303$ K, $\Delta^\ddagger H = 100$ kJ/mol and $\Delta^\ddagger S = 160$ J/mol/K.

in all systems where it has been measured so far.^{116,124} That implies that the ground state is a condition of higher structural order, whereas the transition state allows for a broader distribution of possible structural configurations. This is in agreement with the folded ground state of a protein being the most tightly packed.

The volume of activation represents the size of a cavity that is required so that the ring can rotate without collisions.¹³⁰ A positive sign of $\Delta^\ddagger V$ implies the enlargement of the space around an aromatic ring in its transition state compared to the ground state, again in agreement with the folded ground state of the protein being the most compact.

Interestingly, reported activation enthalpies and activation volumes that were measured on isolated aromatic rings are very similar. $\Delta^\ddagger H$ ranges between 64 kJ/mol (Y97 in cytochrome *c*¹²⁰) and 83-89 kJ/mol (Y23, Y35 and F45 in BPTI¹²⁴ and Y6 in HPr¹¹⁶). Somewhat higher values were only found for the rings in iso-2-cytochrome *c* which are involved in interactions with each other and with a heme group.¹²⁵ The reported $\Delta^\ddagger H$ values are comparable with the activation energies for hydrogen exchange enabled by structural fluctuations of globular proteins.¹⁴⁶ Determined $\Delta^\ddagger V$ values were 27, 28 and 51 ml/mol from HPr¹¹⁶ and BPTI,^{130,131} which can be approximated already by relatively simple geometrical perceptions of the ring flipping motion. Variations are higher in the values for $\Delta^\ddagger S$, which is only reliably measurable when monitoring the process over sufficiently broad temperature ranges. The similarity between reported activation parameter values among different proteins is remarkable since the systems differ in their thermal stability and in characteristics like the number of disulfide bridges.¹¹⁶ This suggests that globular proteins have fluctuation mechanisms in common which determine their flexibility. Furthermore, if the

flexibility of hydrophobic domains is uncorrelated to the overall stability of a protein, this underlines the concept that the formation of hydrophobic clusters is one of the primary steps in the process of protein folding.^{147,148}

Compressibility of Proteins

The isothermal compressibility of proteins is closely associated with their dynamic, structural and functional properties.¹⁴⁹ It reflects a protein's response to an applied pressure and is a benchmark for the flexibility since it is related to volume fluctuations of the molecule.¹⁰⁰ Such fluctuations are partially enabled by atomic packing defects and cavities that exist in the interior of proteins and that are found to shrink under applied pressures.¹⁵⁰ Changes in compressibility are observed during thermal and pressure-induced unfolding,^{151,152} and are furthermore correlated with the hydrogen exchange rates as well as the binding affinity of proteins.¹⁵³ The compressibility and thus softness of proteins in solution is to a large extent determined by the volume fluctuations of internal cavities, but also by complicated hydration impacts arising from the hydrogen bond dynamics at the protein-water interface.¹⁵⁴

The isothermal compressibility is defined as the change of volume in response to an isothermal pressure change and moreover describes the volume fluctuation of a system,¹⁵⁵

$$\kappa = -\frac{1}{\langle V \rangle} \left(\frac{\partial \langle V \rangle}{\partial p} \right)_T = \frac{\langle (\delta V)^2 \rangle}{k_B T \langle V \rangle} \quad (3.12)$$

where p is the pressure, $\langle V \rangle$ is the mean volume of a closed system with fixed particle number and $\delta V = V - \langle V \rangle$ is an isothermal volume fluctuation of the system. The compressibility is in this way related to the mean square deviation of atoms from the equilibrium position.¹⁴⁹

Experimentally, the measurement of ultrasonic wave velocities in an aqueous protein solution yields the adiabatic protein compressibility from which the isothermal compressibility coefficient can be calculated.¹⁵⁶ However hereby one obtains partial compressibilities that contain contributions from the protein as well as the solvent. The latter is regarded in terms of hydration shells, which are the layers of water molecules that surround a biomolecule and which interact with it or are subsequently influenced by it.¹⁵⁷ The protein and water contributions cannot be disentangled without further assumptions, and methods to measure the compressibility with minimized hydration shells are limited to scattering techniques on frozen protein solutions.¹⁴⁹ The experimentally measured partial compressibility, $\bar{\kappa}_p$, can be decomposed into the protein and water contributions according to¹⁵⁸

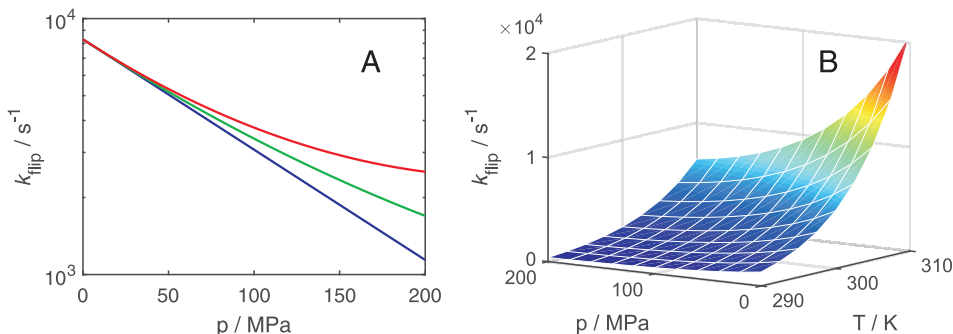


Figure 3.4: Pressure and compressibility dependence of ring flip rates. Calculated with Eq. (3.14) using $\Delta^\ddagger H = 100 \text{ kJ/mol}$, $\Delta^\ddagger S = 160 \text{ J/mol/K}$ and $\Delta^\ddagger V = 25 \text{ ml/mol}$. (A) Flip rates as a function of p for $\Delta^\ddagger \kappa' / (\text{ml/mol/MPa}) = 0$ (blue), 0.05 (green) and 0.1 (red). (B) k_{flip} as a function of pressure and temperature using $\Delta^\ddagger \kappa' = 0.1 \text{ ml/mol/MPa}$.

$$\bar{\kappa}_p = \bar{\kappa}_{p,\text{int}} + \bar{\kappa}_{p,\text{hyd}} + \bar{\kappa}_{p,\text{ex}} \quad (3.13)$$

Here, $\bar{\kappa}_{p,\text{int}}$ is the intrinsic protein contribution representing the volume-corrected protein component compressibility, which in turn is due to self-correlated local volume fluctuations and cross-correlated fluctuations in adjacent solvent shells.¹⁵⁹ The self-compressibility of different proteins was calculated to be around 0.12 GPa^{-1} , which is the isothermal compressibility of ice.^{154,158} The hydration contribution, $\bar{\kappa}_{p,\text{hyd}}$, is representing the intrinsic compressibility of the solvent. It is a function of the distance from the protein surface since the packing density of water molecules is lower in hydration shells further away from the protein.¹⁶⁰ Different from the protein, the hydration shells are open thermodynamic systems with fluctuating numbers of water molecules. This is taken into account by the exchange contribution, $\bar{\kappa}_{p,\text{ex}}$.¹⁵⁸ Although difficult to distinguish from experimental methods, the different contributions to the partial compressibility can be computed using molecular dynamics simulations. There the different geometries and interactions of protein atoms and cavities as well as the solvent molecules need to be considered by careful definition of the respective volumes.

Aromatic rings in the interior of proteins are largely shielded from the solvent, so that their dynamics are primarily governed by local volume fluctuations. They therefore provide unique information on the protein compressibility with only secondary correlation to the dynamics of the hydration shells. The cavity volume required for a rotation of an aromatic ring can in principle be provided by fluctuations of its surrounding which do not lead to a net expansion of the protein. The pressure effect on the flip rate is then taken into account using an isothermal volume compressibility of activation, denoted $\Delta^\ddagger \kappa' = \Delta^\ddagger (\kappa V)$. In Paper III of this thesis the relationship between compressibility coefficients and the free energy of activation of a ring flip

process will be derived in detail. Introducing the consequent second-order pressure dependence of the ring flip rate into the Eyring equation (3.9), it reads

$$k_{\text{flip}} = \frac{k_{\text{B}}T}{h} e^{-\frac{\Delta^\ddagger H}{RT} + \frac{\Delta^\ddagger S}{R} - p\frac{\Delta^\ddagger V}{RT} + p^2\frac{\Delta^\ddagger \kappa'}{2RT}} \quad (3.14)$$

Figure 3.4A displays how the decline of the flip rate with increasing pressure is attenuated by a positive volume compressibility. The effect is more pronounced at high pressures, where flip rates have to be measured with high accuracy to determine the compressibility coefficient reliably. Combined variation of pressure and temperature allows for a more precise measurement and separation of the different activation parameters.^{161,162} In Fig. 3.4B the contributions of temperature and pressure to the absolute flip rate are visualized in one graph. Its characteristic shape is resulting from a parabolic p - T phase diagram of ring flips that will be established in Paper III.

Chapter 4

Results and Conclusions

In this thesis the results of the research work are presented and discussed in four articles which have been published in peer-review journals. In the current chapter, every publication is shortly introduced. The introductions are not supposed to repeat the abstract of the actual papers, which the reader is encouraged to read entirely, but to put the publications in context and highlight the relevance of the addressed issues. In addition, the author contributions to every project are specified here. For the Papers I and III, supplementary material exists that can be found in the appendix.

Paper I: Slow ring flips in aromatic cluster of GB1 studied by aromatic ^{13}C relaxation dispersion methods

In this publication we show that protein GB1 is particularly suited for the investigation of conformational fluctuations in a protein core under variation of temperature and pressure. This builds on a preceding solution-state NMR study which found that the native state of GB1 is stabilized by pressure and that the intensity of aromatic signals is affected by slow ring flip processes.⁴⁰ The hydrophobic core of GB1 contains four aromatic rings which cluster together by stacking interactions. Numerous protein systems are known to contain networks of interacting aromatic rings,¹⁰⁸ and the enthalpy of activation reports on the stabilizing interactions. Yet so far only one study exists that determined the ring flip activation parameters of an aromatic pair, finding similar activation enthalpies for both rings.¹²⁵ The question if there is a correlation between aromatic stacking interactions and the activation parameters of ring flips was addressed in the following paper using state-of-the-art aromatic ^{13}C relaxation dis-

persion methods on site-specific isotope labeled GB1 at different temperatures and pressures. We did not observe any such correlation but found that exchange rates between the rings are similar except for considerably elevated rates for the aromatic ring which is the center of the cluster and interacting with all of the other rings. This is an indication for correlated ring flips where two or more rings accommodate their stabilizing interactions and allocate partial space to move into. Concerted rotational motions have been discussed directly after the discovery of ring flips but never been detected experimentally.¹⁴⁵ We established GB1 as a model system for studying ring flips by exploiting beneficial structural properties of the protein.

Hitherto activation parameters of ring flips under different hydrostatic pressures were investigated in two protein systems only. Very few activation volumes were actually measured even though this parameter is crucial to understand the ring flip mechanism. To gain a substantiated understanding of the cavity model of ring flips, the activation volumes for aromatic rings with different solvent exposure were determined in the following study, thereby doubling the number of published ring flip activation volumes.

Author contributions: The author did the purification of the proteins with the help of H. Raum. The author performed all experiments and the subsequent analysis of data and contributed to the writing of the manuscript.

Paper II: $^1\text{H } R_{1\rho}$ relaxation dispersion experiments in aromatic side chains

In the previous article it was shown that not all positions in aromatic side chains are amenable to the measurement of ring flips with existing ^{13}C relaxation dispersion methods. If the chemical shift difference between the exchanging sites is zero, the respective signal line shape is unaffected by ring flips. This is the case for the ^{13}C chemical shifts of F30 ϵ and F52 δ in GB1. The F30 δ position also suffers a disadvantage because the large carbon chemical shift difference gives rise to a severely broadened signal at temperatures where the flip rate is in the appropriate range for the $^{13}\text{C } R_{1\rho}$ experiment. However the proton chemical shift difference is not zero so that a complementary $^1\text{H } R_{1\rho}$ experiment will allow to determine the flip rates and thus the enthalpy and entropy of activation in such cases.

Protons are ubiquitous in biological macromolecules as well as sensitive to conformational changes and their large gyromagnetic ratio can be exploited to gain high spin-lock powers.¹⁶³ Therefore $^1\text{H } R_{1\rho}$ experiments have been developed for amide protons^{93,164} and methyl groups¹⁶⁵. Here we developed and benchmarked a $^1\text{H } R_{1\rho}$ experiment for aromatic side chains. $^3J_{\text{HH}}$ -couplings and loss of magnetization dur-

ing the spin-lock period through the Rotating Frame Overhauser Effect (ROE) and Hartmann-Hahn coherence transfer can distort the relaxation dispersion. The following study addresses these issues by introducing the relaxation dispersion experiment in combination with site-selective ^{13}C and ^1H labeling schemes.

The new pulse sequence was used to measure ring flip rates in a temperature dependent way so that activation parameters could be calculated. The results are in excellent agreement with the data of Paper I, which were obtained by ^{13}C $R_{1\rho}$ experiments. The presented pulse sequence extends the applicability of relaxation dispersion methods to nuclei that were inaccessible before and allows to study faster exchange processes.

Author contributions: The author conducted the purification of the proteins and contributed to the development of the pulse sequence. The author performed all experiments and the subsequent analysis of data and contributed to the writing of the manuscript.

Paper III: Transition-state compressibility and activation volume of transient protein conformational fluctuations

To understand the nature of protein conformational fluctuations a thorough thermodynamic characterization of the occupied structural states is required. Even for seemingly simple processes like the rotational motions of aromatic amino acid side chains the analysis is complicated because stabilizing interactions and structural properties in all states are affected by the compounded effects of temperature and pressure. Furthermore, activation parameters always report on ensemble-averaged differences between the versatile ground and transition states.

The dynamics of ring flips and the broad distribution of possible flip rates are determined by the packing density and flexibility of proteins, which in turn are expected to be sensitive to hydrostatic pressure. The effects of pressure on the enthalpy and volume of activation therefore give account of the stabilizing interactions and compressibility of the ground and transition state of a ring flip process. In the first pressure dependent study on ring flips it was assumed that “the transient volume increase around an aromatic ring is not localized in a compressible ring environment but is transmitted to the protein surface since otherwise no ΔV^\ddagger would be observed.”¹³⁰ In the following study a difference in volume compressibility between the ground state and transition-state ensemble is investigated and ring flips occurring with zero net activation volume are traced for the first time. For F52 which is deeply embedded in the hydrophobic core of GB1 the ring flip rates were measured over a broad range of temperatures and pressures to unveil a second-order pressure dependence of the flip rate. The combined variation of both thermodynamic parameters allows for calculation of a phase diagram

for the free energy barrier of ring flips. The underlying theory following the example of protein unfolding¹⁶⁶ was developed and justified by statistical methods. From the volume compressibility of activation the isothermal compressibility of the transition state and the component compressibility of the hydrophobic core itself could be estimated.

Author contributions: The author performed the experiments together with B. Dorn (in the scope of a Bachelor thesis). The author adapted the theory and analyzed the data together with K. Modig. The author contributed to the writing of the manuscript.

Paper IV: Characterizing fast conformational exchange of aromatic rings using residual dipolar couplings: Distinguishing jumplike flips from other exchange mechanisms

With the first detection of ring flips, discussions about the mechanistic principles of processes in the interior of proteins were brought into focus. The occurrence of the positive ring flip activation volume was interpreted by two different models. In the diffusion model based on Kramer's theory,¹⁶⁷ the ring was considered to rotate continuously in a viscous protein interior, so that the reaction rate would be determined mainly by enthalpic and frictional effects.¹⁶⁸ In the cavity model described by the transition-state theory, the ring flip is a jumplike rotation associated with the formation of a cavity providing the required free volume.¹³⁰ The activation volumes can then be predicted by the difference in volumes occupied by a fully rotating ring and the ring in the ground state. Experimental findings agree very well and clearly support the latter conception.¹¹⁶ For the symmetry-related sites of aromatic rings in GB1 two distinct NMR resonance signals could be measured under slow-exchange conditions, reporting on the ground state structures. With increasing temperature they coalesce into a single signal at the average resonance frequency, as expected for a symmetric two-site exchange process. Nuclei in a ring which occupies all possible χ_2 rotation angles would not necessarily give rise to an averaged signal at this frequency. Nevertheless there is still a discussion about whether dynamics of aromatic rings go beyond a cavity or breathing model and how much the underlying mechanisms can vary from protein to protein. In consequence of the cavity model and the findings of the previous articles, the transition state of ring flips in some proteins have liquid-like properties, while the ground-state can be considered solid-like. In contrast, diffusive ring motions as inferred from a study on ubiquitin would suggest a liquid-like nature even for the ground state.¹³² It is therefore important to distinguish between different fluctuation mechanisms that affect exchange measurements.

The following study aims to prove jumplike flips and thus to validate the cavity model by exploiting residual dipolar couplings in a weakly aligned protein sample. RDCs enable the detection of exchange processes even when the chemical shift differences between exchanging nuclei are zero, because they can provide the required modulation of resonance frequencies.¹⁶⁹ Aromatic ring flips were thus measured by RDC-mediated relaxation dispersion experiments for the first time. Experimental results were compared to RDCs of the aromatic bond vectors predicted from crystal structures under alignment.

Author contributions: The author performed all experiments and the subsequent analysis of data. The author carried out the RDC calculations and contributed to the writing of the manuscript.

Paper 1





Slow ring flips in aromatic cluster of GB1 studied by aromatic ^{13}C relaxation dispersion methods

Matthias Dreydoppel¹ · Heiner N. Raum¹ · Ulrich Weininger¹

Received: 28 November 2019 / Accepted: 27 January 2020 / Published online: 3 February 2020
© The Author(s) 2020

Abstract

Ring flips of phenylalanine and tyrosine are a hallmark of protein dynamics. They report on transient breathing motions of proteins. In addition, flip rates also depend on stabilizing interactions in the ground state, like aromatic stacking or cation– π interaction. So far, experimental studies of ring flips have almost exclusively been performed on aromatic rings without stabilizing interactions. Here we investigate ring flip dynamics of Phe and Tyr in the aromatic cluster in GB1. We found that all four residues of the cluster, Y3, F30, Y45 and F52, display slow ring flips. Interestingly, F52, the central residue of the cluster, which makes aromatic contacts with all three others, is flipping significantly faster, while the other rings are flipping with the same rates within margin of error. Determined activation enthalpies and activation volumes of these processes are in the same range of other reported ring flips of single aromatic rings. There is no correlation of the number of aromatic stacking interactions to the activation enthalpy, and no correlation of the ring's extent of burying to the activation volume. Because of these findings, we speculate that F52 is undergoing concerted ring flips with each of the other rings.

Keywords Aromatic interaction · NMR spectroscopy · Protein dynamics · Protein breathing · Protein stability

Introduction

Aromatic residues are overrepresented in protein binding interfaces where they contribute to a significant part of the binding free energy. They also contribute to a significant part (roughly 25% of the volume in average) of the hydrophobic core where they stabilize proteins in two ways. Firstly, they are hydrophobic (especially Trp and Phe) and contribute to the so called hydrophobic effect, where hydrophobic side chains are excluded from the solvent (water) (Pace et al. 2014; Rose and Wolfenden 1993). Secondly, due to their quadrupolar electrostatic character, they can be engaged in specific aromatic-aromatic pair interactions (Burley and Petsko 1985, 1989) and interact with cations (Mahadevi and Sastry 2013) or sulfur (Valley et al. 2012).

Additionally, many Phe and Tyr residues undergo frequent 180° rotations ("ring flips") of the χ_2 dihedral angle (around the imaginary $\text{C}_\beta\text{--C}_\gamma\text{--C}_\zeta$ axis) (Campbell et al. 1975; Hattori et al. 2004; Hull and Sykes 1975; Wagner et al. 1976, 1987; Weininger et al. 2013, 2014b; Wüthrich and Wagner 1975; Yang et al. 2015). The requirement for a ring flip to occur is that the surrounding undergoes concerted "breathing" motions with relatively large activation volumes (Hattori et al. 2004; Li et al. 1999; Wagner 1980). Thus, aromatic side chains are the perfect probe for such transient dynamic processes in proteins. Additionally, a ring flip directly reports on the energy difference between the ground state and the transition state (90° tilted ring). Because of the quadrupolar electrostatic nature, interactions that are stabilizing the ground state are destabilizing the transition state and thus are leading to slower ring flips. Comparing ring flips for aromatic residues involved in different interactions should therefore provide an experimental measure of the energy of these interactions.

Experimental measurements of ring flips, however, have been limited so far to a handful of cases since their discovery in the 1970s (Campbell et al. 1975; Hull and Sykes 1975; Wagner et al. 1976). Recently, new cases have been reported (Weininger et al. 2014b; Yang et al. 2015) enabled

Electronic supplementary material The online version of this article (<https://doi.org/10.1007/s10858-020-00303-3>) contains supplementary material, which is available to authorized users.

✉ Ulrich Weininger
ulrich.weininger@physik.uni-halle.de

¹ Institute of Physics, Biophysics, Martin-Luther-University Halle-Wittenberg, 06120 Halle (Saale), Germany

by methodological advances in site-selective ^{13}C labeling (Lundström et al. 2007; Teilum et al. 2006), aromatic ^{13}C relaxation dispersion experiments (Weininger et al. 2012, 2014a) and the understanding of strong ^1H – ^1H couplings (Weininger et al. 2013). Additionally, ring flips can be studied by long scale MD simulations (Shaw et al. 2010) and extremely fast ring flips are shown to affect order parameters (Kasinath et al. 2015). So far, ring flips in all but one system (Nall and Zuniga 1990) are of aromatic residues without specific interactions, like aromatic-aromatic pair interactions (Burley and Petsko 1985, 1989) and interactions with cations (Mahadevi and Sastry 2013) or sulfur (Valley et al. 2012). They all show a similar activation enthalpy of 83–97 kJ mol $^{-1}$ (Hattori et al. 2004; Weininger et al. 2014b), while for Iso-2-cytochrome c higher activation enthalpies of 117–150 kJ mol $^{-1}$ have been observed (Nall and Zuniga 1990). Here the rings of Y46 and Y48 pack tightly together in a typical aromatic-pair interaction, while Y67 packs against the hem group.

Applying high pressure is an elegant way to slow down ring flips and to study their activation volumes. So far, activation volumes have been determined to 27 mL mol $^{-1}$ (Y6 in HPr) (Hattori et al. 2004), 51 mL mol $^{-1}$ (Y35 in BPTI) and 27 mL mol $^{-1}$ (F45 in BPTI) (Li et al. 1999). A connection with the energy of a ring flip is not known. For extremely fast ring flips, that affect order parameters, no sizeable pressure effect was observed (Kasinath et al. 2015).

Here we investigate slow ring flips in the aromatic cluster of GB1 that have been found recently (Dreydoppel et al. 2018), using ^{13}C aromatic relaxation dispersion methods (Weininger et al. 2012, 2014a) in a temperature and pressure dependent way. We found that all four residues of the cluster (Y3, F30, Y45, F52) show slow ring flips. Y3, Y45 and F52 displayed nearly identical activation enthalpies and activation volumes similar to previously determined (Campbell et al. 1975; Hattori et al. 2004; Li et al. 1999; Weininger et al. 2014b), while F30 did not allow any quantification. Moreover, ring flip rates are nearly identical for Y3, Y45 (and F30) while ring flips for F52 are significantly faster. F52 is the central part of the aromatic cluster, in contact with all the other slow flipping rings. We speculate that standard activation enthalpies and faster flip rates in the center of the cluster point to correlated flip motions of F52 with all its other ring partners, each at a time.

Materials and methods

Protein samples

1- ^{13}C and 2- ^{13}C glucose labeled GB1 (UniProtKB P06654) was expressed and purified as described elsewhere (Lindman et al. 2006). 1- ^{13}C glucose labeling (Teilum et al. 2006)

results in site-selective ^{13}C labeled Phe and Tyr δ positions, 2- ^{13}C glucose labeling (Lundström et al. 2007) in site-selective ^{13}C labeled Phe and Tyr ϵ positions. It was dissolved to a concentration of around 5 mM in 20 mM HEPES, 90% $\text{H}_2\text{O}/10\%$ D_2O with addition of small amounts of NaN_3 . The pH was adjusted to 7.0 in the sample.

NMR spectroscopy

All experiments were performed at Bruker Avance III spectrometers at a static magnetic field strength of 14.1 T. Aromatic L-optimized TROSY selected ^{13}C CPMG (Weininger et al. 2012) and $R_{1\rho}$ (Weininger et al. 2014a) relaxation dispersion experiments have been acquired between 10 and 40 °C and 0.1 and 100 MPa. $R_{1\rho}$ relaxation dispersion experiments have been recorded on-resonance. High pressure experiments were performed using a commercial 3 mm ceramic cell (Peterson and Wand 2005) (Daedalus Innovations LLC), connected to a home-built pressure generator. An aromatic $^1\text{H}^{13}\text{C}$ -TROSY-HSQC spectrum at -5 °C and 200 MPa was recorded by utilizing pre-cooled air from an external device. Spectra were processed with NMRPipe (Delaglio et al. 1995) and analyzed with PINT (Ahlner et al. 2013).

Non-averaged signals at low temperature and high pressure

At -5 °C and 200 MPa ring flips become so slow that the individual sides of the ring could be observed in the spectra (see Table 1). This enabled us to determine the ^{13}C $\Delta\delta$ for the two sides of Y3 δ (2.11 ppm), Y3 ϵ (1.40 ppm), F30 δ (5.39 ppm), F30 ϵ (0.00 ppm) and F52 ϵ (1.76 ppm). Previously, it was found that the shift difference $\Delta\delta$ is not changing with temperature (Weininger et al. 2014b). Therefore, we used the derived $\Delta\delta$ as fixed parameters in the fitting of the $R_{1\rho}$ relaxation dispersion experiments, when possible. Derived ^{13}C $\Delta\delta$ might be slightly too low, because the spectrum might still be affected by exchange. However they still serve as a meaningful restraint of the fit. Furthermore, in BPTI the potential problem can be estimated to less than 1%.

Data analysis

$R_{1\rho}$ relaxation dispersion data were fitted to the general equation for symmetric exchange derived by Miloushev and Palmer (2005) using fixed populations, $p_1 = p_2 = 0.5$, and treating $\Delta\delta$ either as a free parameter ($\Delta\delta_{\text{disp}}$) or fixed at the value ($\Delta\delta_{\text{spectra}}$) measured from HSQC spectra under slow-exchange conditions. Derived relaxation dispersion data at different temperatures and pressures were fitted simultaneously with the restrictions: $k_{\text{flip}}(T_{\text{high}}) > k_{\text{flip}}(T_{\text{low}})$, $R_{2,0}(T_{\text{high}}) \leq R_{2,0}(T_{\text{low}})$, and $k_{\text{flip}}(p_{\text{high}}) < k_{\text{flip}}(p_{\text{low}})$.

Table 1 Effect of slow ring flips on possible positions of Phe and Tyr residues

Position	$\Delta\delta^{\text{1H}}$ (ppm)	$\Delta\delta^{\text{13C}}$ (ppm)	LB $^{\text{1H}}$	LB $^{\text{13C}}$	$R_{\text{ex}}^{\text{13C}}$	Ring flip	RD method
Y3 δ	0.40	2.11	Yes	Yes	Yes	Slow	$^{\text{1H/13C}}$
Y3 ϵ	0.50	1.40	Yes	Yes	Yes	Slow	$^{\text{1H/13C}}$
F30 δ	0.84	5.39	Yes	Yes	Yes	Slow	$^{\text{1H/13C}}$
F30 ϵ	0.56	0.00	Yes	No	No	Slow	$^{\text{1H}}$
Y33 δ			No	No	No	Fast	
Y33 ϵ			No	No	No	Fast	
Y45 δ						Slow	
Y45 ϵ			Yes	Yes	Yes	Slow	$^{\text{1H/13C}}$
F52 δ			No	No		Slow	
F52 ϵ	0.00	1.76	No	Yes	Yes	Slow	$^{\text{13C}}$

$\Delta\delta$: chemical shift difference between individual signals of both sides of the ring, detected at -5°C and 200 MPa. LB: significant line broadening at lower temperatures. R_{ex} : exchange contribution of R_2 at lower temperatures. RD method: suitable relaxation dispersion method to study slow ring flips on this position

Activation barriers of the ring flips were determined by non-linear regression of the flip rates, $k_{\text{flip}} = k_{\text{ex}}/2$, on the temperature T , using the Eyring equation. The Eyring equation was parameterized as

$$k_{\text{flip}} = \left(\frac{k_{\text{B}}T}{h}\right) \times \exp\left[-(\Delta H^{\ddagger} - T\Delta S^{\ddagger})/RT\right] \quad (1)$$

where k_{B} and h are Boltzmann's and Planck's constants, respectively, and ΔH^{\ddagger} and ΔS^{\ddagger} are the activation enthalpy and activation entropy, respectively. Activation volumes ΔV^{\ddagger} were determined from the pressure dependence of the flip rates according to

$$\left(\frac{\partial \ln k_{\text{flip}}}{\partial p}\right) = -\frac{\Delta V^{\ddagger}}{RT} \quad (2)$$

Errors in the fitted parameters were estimated using Monte–Carlo simulations (Press et al. 2002); the reported errors correspond to one standard deviation.

Volume occupancies from aromatic rings in ground or transition state were estimated considering them as rotational ellipsoids with half-axes of 3.5 Å and 1.76 Å (Tsai et al. 1999; Wagner 1980). The intersection volumes of two rings in aromatic contact were then calculated using their spatial dispositions from the crystal structure (1pgb.pdb).

Results

Protein GB1 consists of five symmetric aromatic residues (Fig. 1), three Tyr (3, 33, 45) and two Phe (30, 52). According to their hydrophobicity, the Tyr are located closer to the surface while the Phe are buried more in the interior. The accessible surface area of the aromatic side-chains determined by GETAREA (Fraczkiewicz and Braun 1998) using 1pgb.pdb ranks the following: Y33 (70 Å²) >> Y45

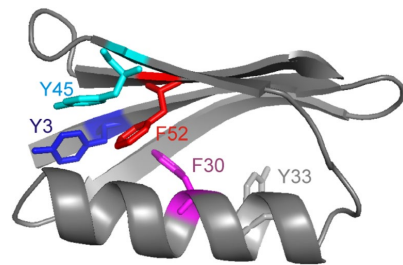


Fig. 1 Three-dimensional structure of GB1 (1pgb.pdb) shown as ribbon presentation. Phe and Tyr side-chains are shown colored in stick representation and are labeled accordingly

(48 Å²) >> Y3 (6 Å²) > F30 (4 Å²) ~ F52 (4 Å²). Y33 is not involved in any particular stabilizing interactions. Y45 is stacking with the π cloud of F52 from one side, F30 is stacking with it from the other side. F52 itself is stacking with the π cloud of Y3.

Identification of slow ring flips in GB1

Five averaged signals of the δ positions (δ^*) and five averaged signals of the ϵ positions (ϵ^*) can be observed in the aromatic $^{\text{1H13C}}$ TROSY-HSQC spectra at higher temperatures. At lower temperatures signals from Y3 δ/ϵ , F30 δ/ϵ , Y45 δ/ϵ and F52 ϵ are becoming broadened (SI Fig. 1) and significantly less intense (Fig. 2). In contrast, both signals of Y33 are unaffected (other than intensity losses from slower tumbling at lower temperature). A combination of low temperature (-5°C) and applied high pressure (200 MPa) is slowing down the flip processes so far, that a splitting of several signals (Y3 δ , Y3 ϵ , F30 δ , F30 ϵ and F52 ϵ) could be observed, representing both sides of the ring in different chemical environments (Fig. 3). This effect was further

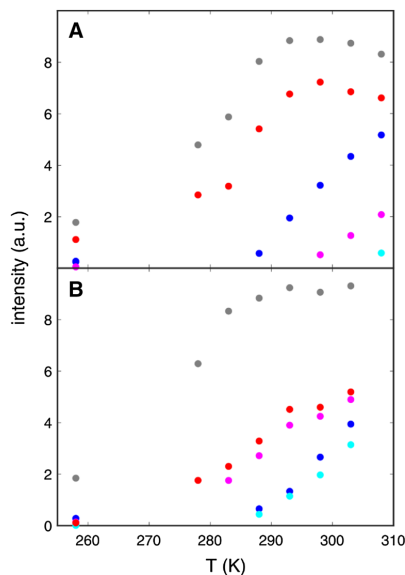


Fig. 2 Intensity of aromatic signals that can be affected by ring flips (Phe and Tyr δ and ϵ). Y3 is shown in blue, F30 in magenta, Y33 in grey, Y45 in cyan and F52 in red. Normalized relative intensities of δ (a) and ϵ (b) are plotted against the temperature. Intensities of -5°C and 200 MPa are plotted at -15°C , since going from 0.1 to 200 MPa has roughly the same effect on the rate of ring flips than lowering the temperature by 10 K. Here the intensities of the two individual signals ($\delta 1$ and $\delta 2$, or $\epsilon 1$ and $\epsilon 2$) are the same within the symbol size. In all other cases, only averaged signals δ^* and ϵ^* (or no signals) could be observed

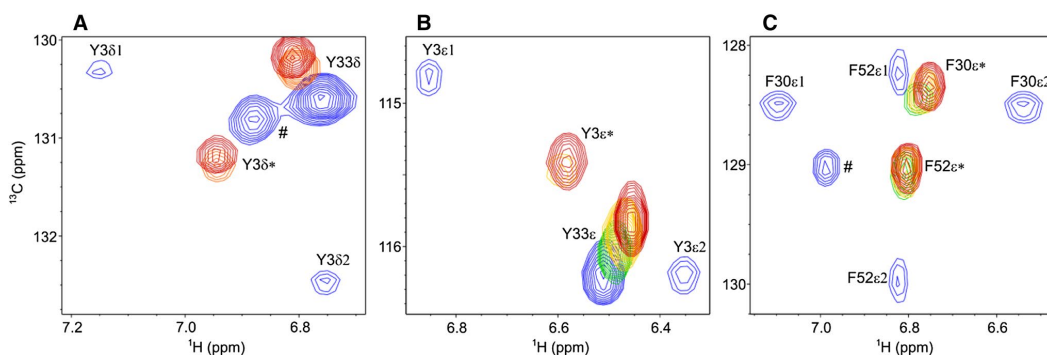


Fig. 3 Region of a Tyr δ^* (Y3 and Y33), b Tyr ϵ^* (Y3 and Y33) and c Phe ϵ^* (F30 and F52) in the aromatic $^1\text{H}/^{13}\text{C}$ -TROSY-HSQC of GB1 at 30 $^\circ\text{C}$ (red), 25 $^\circ\text{C}$ (orange), 20 $^\circ\text{C}$ (yellow), 10 $^\circ\text{C}$ (green) and ambient pressure. The spectrum at -5°C and 200 MPa is shown in blue, where split signals ($\delta 1$ and $\delta 2$, or $\epsilon 1$ and $\epsilon 2$, respectively)

elaborated by aromatic ^{13}C CPMG relaxation dispersion experiments, showing an increase in ^{13}C R_2 (at lower temperatures) for the exact same positions where an increase in the ^{13}C line width was observed (SI Figs. 1, 2). Furthermore, the kinetic process that is causing the increase in R_2 is too fast to be quenched by CPMG experiments (SI Fig. 2). Taken all these findings together (Table 1), it could be established that all rings of the aromatic cluster are undergoing slow ring flips which causes an effect on ^{13}C R_2 , line shapes and consequently signal intensity. The exception is Y33, which does not show any signs that would point towards a slow ring flip. Together with its high surface exposure we concluded that Y33 is undergoing fast ring flips. Five positions are suitable for studying slow ring flips by ^{13}C relaxation dispersion methods over a range of temperature: Y3 δ , Y45 ϵ and F52 ϵ , and to a lesser degree Y3 ϵ and F30 δ . In F30 ϵ and F52 δ ^{13}C (and in case of F52 also ^1H) is unaffected by ring flips, since the respective $\Delta\delta$ between both sides of the ring is (close to) zero. Y45 δ is only detectable at 35 $^\circ\text{C}$ where ring flips are too fast to be studied by ^{13}C $R_{1\rho}$ experiments.

Quantification of slow ring flips in Y3, F30, Y45 and F52 by aromatic ^{13}C $R_{1\rho}$ relaxation dispersion experiments

Over the whole studied range of temperature (10 $^\circ\text{C}$ to 40 $^\circ\text{C}$) at ambient pressure only averaged signals could be observed, or signals have been broadened beyond detection. The underlying ring flips causing the averaged signals are too fast to be captured by aromatic ^{13}C CPMG relaxation dispersion experiments (Weininger et al. 2012) (SI Fig. 2), in agreement with observations on BPTI (Weininger et al. 2014b). Therefore, aromatic ^{13}C $R_{1\rho}$ relaxation dispersion

can be observed. Signals indicated as # are caused by sample impurities which can be detected at very high S/N experiments, which were needed for the -5°C and 200 MPa condition, where the split signals are still severely broadened

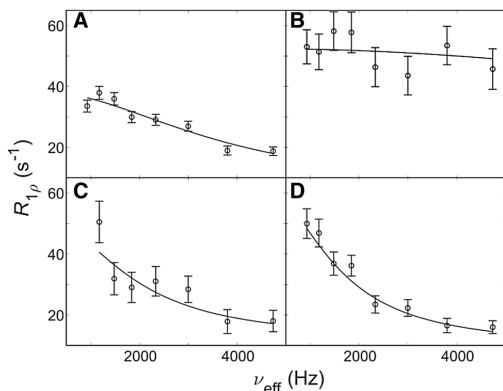


Fig. 4 Aromatic ^{13}C L-TROSY-selected $R_{1\rho}$ relaxation dispersions recorded on-resonance (tilt angle $\theta > 85^\circ$) at a static magnetic field-strength of 14.1 T. Dispersion profiles for Y3 δ at 25 °C (a), F30 δ at 35 °C (b), Y45e at 20 °C (c) and F52e at 10 °C (d) are shown. Data were fitted with fixed populations $p_1 = p_2 = 0.5$ and free (Y45) or fixed chemical shift differences $\Delta\delta_{\text{disp}}$ derived from low temperature and high pressure spectra. The resulting flip rates are: $(12 \pm 2) \times 10^3 \text{ s}^{-1}$, $(53 \pm 4) \times 10^3 \text{ s}^{-1}$, $(6 \pm 2) \times 10^3 \text{ s}^{-1}$ and $(4.8 \pm 0.9) \times 10^3 \text{ s}^{-1}$, respectively

experiments (Weininger et al. 2014a) have been applied. Relaxation dispersion profiles could be recorded for Y3 δ , Y45e and F52e (Fig. 4a, c, d), which could be fitted to the ring flip processes. F30 δ at high temperatures displays increased $R_{1\rho}$ values, which cannot be quenched sufficiently (Fig. 4b). ^{13}C $R_{1\rho}$ relaxation dispersion experiments are allowing an accurate quantification of the ring flip processes by a simultaneous and restricted fit at different temperatures or pressures. Determined flip rates range from 4000 to 38,000 s^{-1} (75,000 s^{-1} for F30).

Aromatic ^{13}C $R_{1\rho}$ relaxation dispersion profiles could be recorded and quantified for Y3 δ at 25 °C, 30 °C and 35 °C, Y45e at 20 °C, 25 °C and 30 °C, and F52e at 10 °C, 15 °C and 20 °C. For F30 δ , only two temperatures (35 °C and 40 °C) could be used (SI Figs. 3–6). Plotting the derived flip rates against temperature (Fig. 5) reveals similar flip rates for Y3, F30 and Y45 (within margin of error), but significantly faster flip rates for F52 (at a given temperature). The latter are approximately three times higher, as can be seen from the values at 25 °C, where rates of $12 \times 10^3 \text{ s}^{-1}$ and $11 \times 10^3 \text{ s}^{-1}$ can be measured for Y3 and Y45, respectively, and a value of $37 \times 10^3 \text{ s}^{-1}$ can be extrapolated for F52. Moreover, Y3 and F52, the two residues studied with the highest accuracy, display the same temperature dependence. Because of the higher flip rates, F52 had to be studied at lower temperatures. This finding is somewhat surprising, since F52 is among the most interior aromatic ring and the central part of the cluster (Fig. 1).

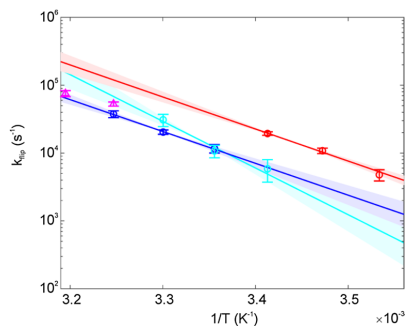


Fig. 5 Temperature dependence of flip rates. k_{flip} is plotted as a function of $1/T$ for F52 (red), Y3 (blue), Y45 (cyan) and F30 (magenta). The fits are displayed as solid lines, while the uncertainties of the fits are displayed as shaded areas in the appropriate colors. The data are represented using a logarithmic y-axis to show the expected linearity, but the fit was performed using non-linear regression of k_{flip} on T

In order to further validate our results derived by aromatic ^{13}C $R_{1\rho}$ relaxation dispersion experiments, we reanalyzed the dispersion profiles for Y3 δ and F52e without the $\Delta\delta$ fixed from information of the low temperature and high pressure spectrum. Derived ring flip rates and activation enthalpies and entropies are the same (within margin of error) with and without the additionally fixed $\Delta\delta$ (SI Fig. 7). Furthermore, derived $\Delta\delta$ of the fits (2.17 ± 0.20 ppm and 1.84 ± 0.09 ppm, for Y3 δ and F52e, respectively) are in excellent agreement with the $\Delta\delta$ from the spectrum (2.11 ppm and 1.76 ppm).

Y3, Y45 and F52 display similar activation enthalpies

Ring flip rates at three temperatures for Y3, Y45 and F52 could be used to derive the activation enthalpy (ΔH^\ddagger) and activation entropy (ΔS^\ddagger) for the individual flip processes using Eq. 1 (Fig. 5). Activation enthalpies for Y3 ($87 \pm 14 \text{ kJ mol}^{-1}$) and F52 ($88 \pm 11 \text{ kJ mol}^{-1}$) are virtually identical. The activation enthalpy for Y45 appears to be somewhat higher ($129 \pm 29 \text{ kJ mol}^{-1}$), but could still be interpreted to be the same as for Y3 and F52, considering the significantly higher error. In fact, only the flip rate at the highest temperature for Y45, which is the least well covered in the relaxation dispersion profiles, is deviating from Y3. Activation entropies are $126 \pm 46 \text{ J mol}^{-1} \text{ K}^{-1}$, $137 \pm 38 \text{ J mol}^{-1} \text{ K}^{-1}$ and $275 \pm 102 \text{ J mol}^{-1} \text{ K}^{-1}$, for Y3, F52 and Y45, respectively. It is not meaningful to derive activation enthalpy and entropy for F30. However, it is safe to assume that the activation enthalpy is not higher than for Y3 and F52, as indicated by the determined flip rates.

Y3, Y45 and F52 display similar activation volumes

Ring flip rates for Y3, Y45 and F52 could also be recorded and quantified at three different (0.1, 50 and 100 MPa) hydrostatic pressures (SI Figs. 8–10). This allowed us to determine the activation volumes (ΔV^\ddagger) of the individual ring flip processes using Eq. 2 (Fig. 6). Activation volumes for Y3 ($26 \pm 5 \text{ mL mol}^{-1}$) and F52 ($29 \pm 2 \text{ mL mol}^{-1}$) are virtually identical. The activation volume for Y45 appears to be somewhat higher ($51 \pm 11 \text{ mL mol}^{-1}$), but could still be interpreted as the same as for Y3 and F52, considering the errors. The findings for the activation volumes thereby resemble the same general observation as for the activation enthalpies.

Again, we validated our results by an analysis without fixed $\Delta\delta$. Derived ring flip rates and activation enthalpies and entropies are again the same (within margin of error) (SI Fig. 7) and derived $\Delta\delta$ of the fits ($1.99 \pm 0.31 \text{ ppm}$, $1.12 \pm 0.09 \text{ ppm}$ and $1.89 \pm 0.07 \text{ ppm}$, for Y3 δ , Y3 ϵ and F52 ϵ , respectively) are in good agreement with the $\Delta\delta$ from the spectrum (2.11 ppm, 1.40 ppm and 1.76 ppm).

Discussion

Ring flips in the fast to intermediate NMR exchange regime

In contrast to previously reported cases of slow ring flips investigated by NMR spectroscopy (Hattori et al. 2004; Wagner et al. 1976, 1987; Weininger et al. 2014b), ring flips in GB1 do not reach the slow exchange regime, in which individual signals for both sides of symmetric aromatic

rings (Phe and Tyr) could be observed, at least not at ambient pressure and temperatures above 0 °C. They are in the fast exchange regime, in which only averaged signals for both sides of symmetric aromatic rings can be observed. By lowering the temperature these signals become gradually broadened and less intense until signals are completely vanished. Since there are surprisingly very limited reports of slow ring flips in the literature, this might be the case for the vast majority of proteins. Ring flips are somewhat slow and can cause a dramatic reduction of signal intensity close to or in the intermediate exchange regime, but are not as slow to reach the slow exchange regime. Thus by more thorough temperature dependent studies of aromatic signals, many more examples of slow ring flips can be expected, despite not reaching the slow exchange regime. The aromatic ^{13}C $R_{1\rho}$ relaxation dispersion experiment is completely eligible to obtain correct ring flip rates (SI Fig. 7) and chemical shift differences, even without information from the slow exchange regime, and therefore allows the quantification of ring flips in the fast to intermediate NMR exchange regime. Furthermore, the determination of flip rates is robust to small variations in the chemical shift difference. In addition, high-pressure NMR is an important tool that allows additional changing of the ring flip conditions.

Individual nuclei in aromatic side chains are affected differently

Four rings in GB1 undergo slow ring flips. In theory, ring flips could be studied on eight positions (4 δ , 4 ϵ). In practice the number of positions that can be used is significantly reduced. While some positions display differences in ^1H and ^{13}C chemical shifts and therefore can be studied by ^1H and ^{13}C methods (Y3 $\delta\epsilon$, F30 δ , Y45 $\delta\epsilon$), others just show differences in ^1H (F30 ϵ) or ^{13}C (F52 ϵ), or not at all (F52 δ). Similar behaviour has been observed in BPTI and rapamycin- or FK506-bound FKBP12 (SI Fig. 11) (Wagner et al. 1987; Weininger et al. 2014b; Yang et al. 2015). There are also examples of slow ring flips where both positions (δ and ϵ) do not display shift differences in ^1H and ^{13}C and thus are not accessible by relaxation dispersion methods (Weininger et al. 2013). Since the time scale of exchange is in the limit of $R_{1\rho}$ and not CPMG relaxation dispersion experiments, and to date no ^1H $R_{1\rho}$ relaxation dispersion methods in aromatic side chains exist, F30 ϵ is also not accessible. If the size of the chemical shift difference (for both sides of the ring) is large in ^1H or ^{13}C , the ^1H - ^{13}C cross signal will be broadened over a large range of temperature, which is the case for F30 δ and presumably Y45 δ . Together with the upper rate limit, that can be studied by ^{13}C $R_{1\rho}$ relaxation dispersion experiments, and limited protein stability at higher temperatures, the final number of accessible positions is reduced even more. In case of GB1, three positions can be studied

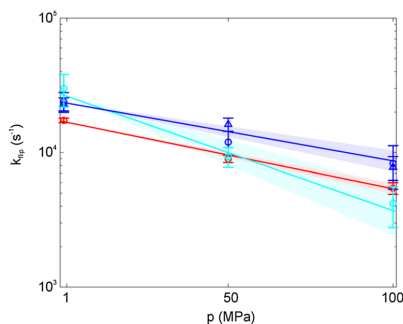
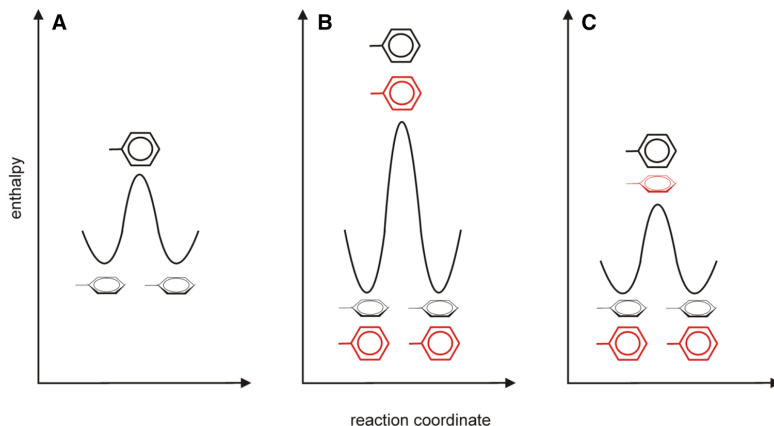


Fig. 6 Pressure dependence of flip rates. k_{flip} is plotted as a function of pressure for F52 (20 °C, red), Y3 (30 °C, blue) and Y45 (30 °C, cyan). The fits are displayed as solid lines, while the uncertainties of the fits are displayed as shaded areas in the appropriate colors. The data are represented using a logarithmic y-axis to show the expected linearity, but the fit was performed using non-linear regression of k_{flip} on p

Fig. 7 Activation enthalpy of ring flips for certain scenarios. **a** Activation enthalpy of a ring without stabilizing contacts. **b** Activation enthalpy of a ring with stabilizing contacts, in this case a stacking ring (shown in red). The stabilization of the ground state is between 5 and 10 kJ mol⁻¹ (Burley and Petsko 1989). **c** Activation enthalpy of a ring with stabilizing contacts of a stacking ring (shown in red), both rings are undergoing concerted ring flips



well (Y36, Y45e and F52e), while for two others the range and accuracy is less (Y3e and F30f). Taken all together, it requires a significant amount of screening conditions in order to conduct a quantitative study of ring flips, if the slow exchange regime cannot be reached.

Ring flips in an aromatic cluster

The key findings for ring flips in GB1 are the following. F52, the central part of the aromatic cluster with three aromatic-aromatic contacts, is flipping at a higher rate (at a given temperature) than Y3, Y45 and F30, which flip with roughly the same rate constants (Fig. 5). The activation enthalpies for F52 (88 ± 11 kJ mol⁻¹) and Y3 (87 ± 14 kJ mol⁻¹) are virtually the same, no activation enthalpy could be determined for F30, but it is rather safe to conclude that it is not larger, whereas Y45 (129 ± 29 kJ mol⁻¹) might also display the same activation enthalpy (within margin of error) or a slightly higher value. Activation entropies (126 ± 46 J mol⁻¹ K⁻¹, 137 ± 38 J mol⁻¹ K⁻¹ and 275 ± 102 J mol⁻¹ K⁻¹) are somewhat higher than previously reported ones, which range between 16 and 96 J mol⁻¹ K⁻¹ (Hattori et al. 2004; Weininger et al. 2014b; Yang et al. 2015). This reflects a higher loss in order in the transition state compared to the ground state of the aromatic cluster of GB1. This might be a characteristic of aromatic clusters in general and potentially is reporting a more ordered ground state. Activation volumes (Fig. 6) for F52 (29 ± 2 mL mol⁻¹) and Y3 (26 ± 5 mL mol⁻¹) are virtually identical; again, Y45 might display the same activation volume (within margin of error) or a slightly higher one (51 ± 11 mL mol⁻¹). Previously reported activation enthalpies (86, 83, 86 and 89 kJ mol⁻¹ for BPTI Y23, Y35 and F45, and HPr Y6, respectively (Hattori et al. 2004; Weininger et al. 2014b) and activation volumes (51, 28 and 27 mL mol⁻¹ for BPTI Y35

and F45 (Li et al. 1999) and HPr Y6 (Hattori et al. 2004)), that have been derived on isolated aromatic rings, are very similar. The only difference is in the activation entropy.

Given all this findings, a global breathing (transient expansion) or unfolding of the aromatic cluster (which would result in higher activation enthalpies and activation volumes) can be ruled out. The ring flip process of aromatic side chains in an aromatic cluster therefore seems to be a local process, only involving a single ring or two rings in a concerted flip as will be discussed below. In fact, derived activation enthalpies and activation volumes are in very good agreement with the flipping of a single ring in an independent event. However, there are two reasons that might question this. Firstly, the central ring of the cluster which has a low accessible surface area, is flipping significantly (around three times) faster (at a given temperature). This finding is surprising, but clearly supported by the experimental data. Isolated single ring flips do not give an explanation for this. Secondly, one would have to assume that aromatic interactions (Burley and Petsko 1985, 1989) do not significantly contribute to ground state stabilization, not even for F52, the central ring with three such interactions. Aromatic stacking, however, is believed to provide between 5 and 10 kJ mol⁻¹ (Burley and Petsko 1989) which would roughly translate to an increased activation enthalpy of 10 to 20 kJ mol⁻¹ (Fig. 7a, b). But it might simply be, that the aromatic environment of F52 is more homogenous and better suitable for dynamic processes like ring flips and this somehow counters the enthalpic ground state stabilization by aromatic stacking.

The other possibility would be that the aromatic ring in aromatic contact with each of the others (F52) could flip in a concerted event with each one of the other rings. Under this assumption (F52 has the possibility to flip together with each Y3, F30 and Y45 in individual events) the flip

rate of F52 would be the sum of all the other flip rates. In case of a concerted flip, the transition state would not be destabilized by an aromatic stacking but also stabilized, resulting in unchanged activation enthalpies (Fig. 7c). Furthermore, activation volumes could then be imagined to be reduced, because of the rings providing partial space for their partners to flip into, when rotating into the transition state. For the spatial configuration in the hydrophobic core of GB1, one obtains volume advantages of 1.6 mL mol^{-1} and 1.5 mL mol^{-1} conceded to F52 by Y45 and F30, respectively. This could partially explain why the activation volume of F52 is not significantly higher than for the others, despite being the central aromatic ring of the cluster. While all these are good reasons to speculate about concerted ring flips, it should be noted that none of the experiments performed in this study is proof for it. In order to accurately prove or disprove concerted ring flips, one has to perform MD simulations or develop challenging multiple quantum (of two rings) NMR exchange experiments (Lundström et al. 2005) through space.

Conclusions

Here we find that the ring in the center of an aromatic cluster (F52), making aromatic stacking to three other aromatic rings, is flipping with a faster rate than the other rings, whose rates are comparable. Activation enthalpies and activation volumes in the cluster, even in its center are not increased. The only ring with a possible increase (Y45) is the ring in the cluster located most on the protein surface. We speculate that these findings are caused by correlated ring flips of F52 to at least two of its adjacent rings.

Acknowledgements Open access funding provided by Projekt DEAL. This research was supported by the Deutsche Forschungsgemeinschaft (Grant No. WE 5587/1-1).

Open Access This article is licensed under a Creative Commons Attribution 4.0 International License, which permits use, sharing, adaptation, distribution and reproduction in any medium or format, as long as you give appropriate credit to the original author(s) and the source, provide a link to the Creative Commons licence, and indicate if changes were made. The images or other third party material in this article are included in the article's Creative Commons licence, unless indicated otherwise in a credit line to the material. If material is not included in the article's Creative Commons licence and your intended use is not permitted by statutory regulation or exceeds the permitted use, you will need to obtain permission directly from the copyright holder. To view a copy of this licence, visit <http://creativecommons.org/licenses/by/4.0/>.

References

- Ahlner A, Carlsson M, Jonsson BH, Lundström P (2013) PINT: a software for integration of peak volumes and extraction of relaxation rates. *J Biomol NMR* 56:191–202. <https://doi.org/10.1007/s10858-013-9737-7>
- Burley SK, Petsko GA (1985) Aromatic-aromatic interaction: a mechanism of protein structure stabilization. *Science* 229:23–28
- Burley SK, Petsko GA (1989) Electrostatic interactions in aromatic oligopeptides contribute to protein stability. *Trends Biotechnol* 7:354–359
- Campbell ID, Dobson CM, Williams RJP (1975) proton magnetic-resonance studies of tyrosine residues of hen lysozyme—assignment and detection of conformational mobility. *Proc Royal Soc B* 189:503–509. <https://doi.org/10.1098/rspb.1975.0070>
- Delaglio F, Grzesiek S, Vuister GW, Zhu G, Pfeifer J, Bax A (1995) Nmrpipe—a multidimensional spectral processing system based on unix pipes. *J Biomol NMR* 6:277–293
- Dreydoppel M, Becker P, Raum HN, Gröger S, Balbach J, Weininger U (2018) Equilibrium and kinetic unfolding of GB1: stabilization of the native state by pressure. *J Phys Chem B* 122:8846–8852. <https://doi.org/10.1021/acs.jpbc.8b06888>
- Fraczkiewicz R, Braun W (1998) Exact and efficient analytical calculation of the accessible surface areas and their gradients for macromolecules. *J Comput Chem* 19:319–333. [https://doi.org/10.1002/\(Sici\)1096-987x\(199802\)19:3%3c319:Aid-Jcc6%3e3.3.Co;2-3](https://doi.org/10.1002/(Sici)1096-987x(199802)19:3%3c319:Aid-Jcc6%3e3.3.Co;2-3)
- Hattori M, Li H, Yamada H, Akasaka K, Hengstenberg W, Gronwald W, Kalbitzer HR (2004) Infrequent cavity-forming fluctuations in HPr from *Staphylococcus carnosus* revealed by pressure- and temperature-dependent tyrosine ring flips. *Protein Sci* 13:3104–3114. <https://doi.org/10.1110/ps.04877104>
- Hull WE, Sykes BD (1975) Fluorotyrosine alkaline-phosphatase—internal mobility of individual tyrosines and role of chemical-shift anisotropy as a F-19 nuclear spin relaxation mechanism in proteins. *J Mol Biol* 98:121–153. [https://doi.org/10.1016/S0022-2836\(75\)80105-7](https://doi.org/10.1016/S0022-2836(75)80105-7)
- Kasinath V, Fu YN, Sharp KA, Wand AJ (2015) A sharp thermal transition of fast aromatic-ring dynamics in ubiquitin. *Angew Chem Int Ed* 54:102–107
- Li H, Yamada H, Akasaka K (1999) Effect of pressure on the tertiary structure and dynamics of folded basic pancreatic trypsin inhibitor. *Biophys J* 77:2801–2812
- Lindman S, Xue WF, Szczepankiewicz O, Bauer MC, Nilsson H, Linse S (2006) Salting the charged surface: pH and salt dependence of protein G B1 stability. *Biophys J* 90:2911–2921. <https://doi.org/10.1529/biophysj.105.071050>
- Lundström P, Mulder FAA, Akke M (2005) Correlated dynamics of consecutive residues reveal transient and cooperative unfolding of secondary structure in proteins. *Proc Natl Acad Sci USA* 102:16984–16989. <https://doi.org/10.1073/pnas.0504361102>
- Lundström P et al (2007) Fractional C-13 enrichment of isolated carbons using [1-C-13]- or [2-C-13]-glucose facilitates the accurate measurement of dynamics at backbone C-alpha and side-chain methyl positions in proteins. *J Biomol NMR* 38:199–212
- Mahadevi AS, Sastry GN (2013) Cation-pi interaction: its role and relevance in chemistry, biology, and material science. *Chem Rev* 113:2100–2138
- Miloushev VZ, Palmer AG (2005) R(1p) relaxation for two-site chemical exchange: general approximations and some exact solutions. *J Magn Reson* 177:221–227. <https://doi.org/10.1016/j.jmr.2005.07.023>
- Nall BT, Zuniga EH (1990) Rates and energetics of tyrosine ring flips in yeast iso-2-cytochrome-c. *Biochemistry* 29:7576–7584

- Pace CN, Scholtz JM, Grimsley GR (2014) Forces stabilizing proteins. *FEBS Lett* 588:2177–2184. <https://doi.org/10.1016/j.febslet.2014.05.006>
- Peterson RW, Wand AJ (2005) Self contained high pressure cell, apparatus and procedure for the preparation of encapsulated proteins dissolved in low viscosity fluids for NMR spectroscopy. *Rev Sci Instrum* 76:1–7. <https://doi.org/10.1063/1.2038087>
- Press WH, Teukolsky SA, Vetterling WT, Flannery BP (2002) *Numerical recipes in C++: the art of scientific computing*, 2nd edn. Cambridge University Press, Cambridge
- Rose GD, Wolfenden R (1993) Hydrogen-bonding, hydrophobicity, packing, and protein-folding. *Annu Rev Biophys Biomol Struct* 22:381–415. <https://doi.org/10.1146/annurev.bb.22.060193.002121>
- Shaw DE et al (2010) Atomic-level characterization of the structural dynamics of proteins. *Science* 330:341–346
- Teilum K, Brath U, Lundström P, Akke M (2006) Biosynthetic C-13 labeling of aromatic side chains in proteins for NMR relaxation measurements. *J Am Chem Soc* 128:2506–2507
- Tsai J, Taylor R, Chothia C, Gerstein M (1999) The packing density in proteins: standard radii and volumes. *J Mol Biol* 290:253–266. <https://doi.org/10.1006/jmbi.1999.2829>
- Valley CC, Cembran A, Perlmutter JD, Lewis AK, Labello NP, Gao J, Sachs JN (2012) The methionine-aromatic motif plays a unique role in stabilizing protein structure. *J Biol Chem* 287:34979–34991
- Wagner G (1980) Activation volumes for the rotational motion of interior aromatic rings in globular-proteins determined by high-resolution h-1-nmr at variable pressure. *FEBS Lett* 112:280–284
- Wagner G, Demarco A, Wüthrich K (1976) Dynamics of aromatic amino-acid residues in globular conformation of basic pancreatic trypsin-inhibitor (Bpti) I H-1 NMR-studies. *Biophys Struct Mech* 2:139–158
- Wagner G, Bruhwiler D, Wüthrich K (1987) Reinvestigation of the aromatic side-chains in the basic pancreatic trypsin-inhibitor by heteronuclear two-dimensional nuclear-magnetic-resonance. *J Mol Biol* 196:227–231
- Weininger U, Respondek M, Akke M (2012) Conformational exchange of aromatic side chains characterized by L-optimized TROSY-selected C-13 CPMG relaxation dispersion. *J Biomol NMR* 54:9–14
- Weininger U, Respondek M, Löw C, Akke M (2013) Slow aromatic ring flips detected despite near-degenerate NMR frequencies of the exchanging nuclei. *J Phys Chem B* 117:9241–9247
- Weininger U, Brath U, Modig K, Teilum K, Akke M (2014a) Off-resonance rotating-frame relaxation dispersion experiment for C-13 in aromatic side chains using L-optimized TROSY-selection. *J Biomol NMR* 59:23–29
- Weininger U, Modig K, Akke M (2014b) Ring flips revisited: C-13 relaxation dispersion measurements of aromatic side chain dynamics and activation barriers in basic pancreatic trypsin inhibitor. *Biochemistry* 53:4519–4525
- Wüthrich K, Wagner G (1975) Nmr investigations of dynamics of aromatic amino-acid residues in basic pancreatic trypsin-inhibitor. *FEBS Lett* 50:265–268. [https://doi.org/10.1016/0014-5793\(75\)80504-7](https://doi.org/10.1016/0014-5793(75)80504-7)
- Yang CJ, Takeda M, Terauchi T, Jee J, Kainosho M (2015) Differential large-amplitude breathing motions in the interface of FKBP12-drug complexes. *Biochemistry* 54:6983–6995. <https://doi.org/10.1021/acs.biochem.5b00820>

Publisher's Note Springer Nature remains neutral with regard to jurisdictional claims in published maps and institutional affiliations.

Paper II





^1H $R_{1\rho}$ relaxation dispersion experiments in aromatic side chains

Matthias Dreydoppel¹ · Roman J. Lichtenecker² · Mikael Akke³ · Ulrich Weinginger¹

Received: 23 June 2021 / Accepted: 3 September 2021 / Published online: 12 September 2021
© The Author(s) 2021

Abstract

Aromatic side chains are attractive probes of protein dynamic, since they are often key residues in enzyme active sites and protein binding sites. Dynamic processes on microsecond to millisecond timescales can be studied by relaxation dispersion experiments that attenuate conformational exchange contributions to the transverse relaxation rate by varying the refocusing frequency of applied radio-frequency fields implemented as either CPMG pulse trains or continuous spin-lock periods. Here we present an aromatic ^1H $R_{1\rho}$ relaxation dispersion experiment enabling studies of two to three times faster exchange processes than achievable by existing experiments for aromatic side chains. We show that site-specific isotope labeling schemes generating isolated ^1H - ^{13}C spin pairs with vicinal ^2H - ^{12}C moieties are necessary to avoid anomalous relaxation dispersion profiles caused by Hartmann–Hahn matching due to the $^3J_{\text{HH}}$ couplings and limited chemical shift differences among ^1H spins in phenylalanine, tyrosine and the six-ring moiety of tryptophan. This labeling pattern is sufficient in that remote protons do not cause additional complications. We validated the approach by measuring ring-flip kinetics in the small protein GB1. The determined rate constants, k_{flip} , agree well with previous results from ^{13}C $R_{1\rho}$ relaxation dispersion experiments, and yield ^1H chemical shift differences between the two sides of the ring in good agreement with values measured under slow-exchange conditions. The aromatic ^1H $R_{1\rho}$ relaxation dispersion experiment in combination with the site-selective ^1H - $^{13}\text{C}/^2\text{H}$ - ^{12}C labeling scheme enable measurement of exchange rates up to $k_{\text{ex}} = 2k_{\text{flip}} = 80,000 \text{ s}^{-1}$, and serve as a useful complement to previously developed ^{13}C -based methods.

Keywords Conformational exchange · Protein dynamics · Aromatic side chains · Rotating-frame relaxation · Aromatic ring-flip

Introduction

Conformational dynamics in proteins on the microsecond to millisecond time scales are often linked to biological function (Mittermaier and Kay 2009). Transiently populated high-energy states play important roles in enzyme catalysis (Boehr et al. 2006; Cole and Loria 2002; Eisenmesser et al. 2002) or ligand binding by conformational selection (Demers and Mittermaier 2009; Malmendal et al. 1999). Such

conformational transitions generally lead to a modulation of NMR parameters as the chemical shift (Gutowsky and Saika 1953), residual dipolar coupling (Igumenova et al. 2007; Vallurupalli et al. 2007) or strong scalar coupling (Weinginger et al. 2013b). The conformational dynamics can be probed by NMR relaxation dispersion methods (Palmer 2004; Palmer et al. 1991), such as $R_{1\rho}$ (Akke and Palmer 1996; James et al. 1977) or Carr-Purcell-Meiboom-Gill (CPMG) experiments (Carr and Purcell 1954; Loria et al. 1999a, 1999b; Meiboom and Gill 1958), and chemical exchange saturation transfer (CEST) methods (Forsen and Hoffman 1963; Palmer and Koss 2019; Vallurupalli et al. 2012, 2017) in the case of slower time scales.

Phenylalanine, tyrosine, histidine and tryptophan all have aromatic side chains, which make them an interesting subgroup of amino acids that serve multiple functions in proteins. Aromatic side chains are bulky and constitute a significant proportion of the protein hydrophobic core. They typically form pairs or clusters on the basis of specific

✉ Ulrich Weinginger
ulrich.weinginger@physik.uni-halle.de

¹ Institute of Physics, Biophysics, Martin-Luther-University Halle-Wittenberg, 06120 Halle (Saale), Germany

² Institute of Organic Chemistry, University of Vienna, 1090 Vienna, Austria

³ Division of Biophysical Chemistry, Center for Molecular Protein Science, Department of Chemistry, Lund University, P.O. Box 124, 22100 Lund, Sweden

aromatic-aromatic interactions (Burley and Petsko 1985, 1989). Furthermore, aromatic residues are overrepresented in protein binding interfaces, where they contribute a significant part of the binding free energy (Birtalan et al. 2010; Bogan and Thorn 1998; Lo Conte et al. 1999). Finally, tyrosine and especially histidine play critical roles in enzyme catalysis, where they make up 6% and 18%, respectively, of all catalytic residues (Bartlett et al. 2002). Histidine can exist in three different states, one protonated and two neutral tautomeric forms. Despite their generally tight packing, Phe and Tyr residues undergo intermittent 180° transitions ('ring flips') of the χ_2 dihedral angle and thereby provide unique information of transient 'breathing' processes of proteins (Dreydoppel et al. 2020; Wagner 1980; Wagner et al. 1976; Weininger et al. 2014b). Each of these properties makes aromatic side chains highly interesting and powerful probes for studying protein dynamics.

Recent developments have enabled straightforward and robust site-selective ^{13}C labeling of aromatic side chains (Kasinath et al. 2013; Lundström et al. 2007; Schörghuber et al. 2018; Teilum et al. 2006; Weininger 2019), which eliminate unwanted relaxation pathways and coherent magnetization transfer via one-bond ^{13}C - ^{13}C couplings. These advancements have made possible advanced studies of protein dynamics involving aromatic side chains, including methods to characterize fast (ps–ns) timescale dynamics via ^{13}C relaxation rate constants (Weininger et al. 2012a) that enable studies of order parameters (Boyer and Lee 2008; Kasinath et al. 2013, 2015). Furthermore, slower (μs – ms) timescale dynamics have been probed with ^{13}C relaxation dispersion experiments, either using CPMG (Weininger et al. 2012b) or $R_{1\rho}$ refocusing elements (Weininger et al. 2014a). In particular, these relaxation dispersion methods have been used to measure ring-flip rates (Dreydoppel et al. 2020; Weininger et al. 2014b) and transient histidine tautomerization (Weininger et al. 2017). Complementary ^1H CPMG relaxation dispersion experiments are applicable to a subset of aromatic sites, namely His δ_2 , His ϵ_1 and Trp δ_1 . Other positions are inaccessible due to sizeable $^3J_{\text{HH}}$ couplings and possibly strong $^1J_{\text{CC}}$, where 1J -couplings are equal or greater than the chemical shift difference, can

cause severe artifacts (Raum et al. 2018). Site-selective ^1H - $^{13}\text{C}/^2\text{H}$ - ^{12}C labeling addresses both issues and allows to obtain artifact-free ^1H CPMG relaxation dispersion profiles (Raum et al. 2019).

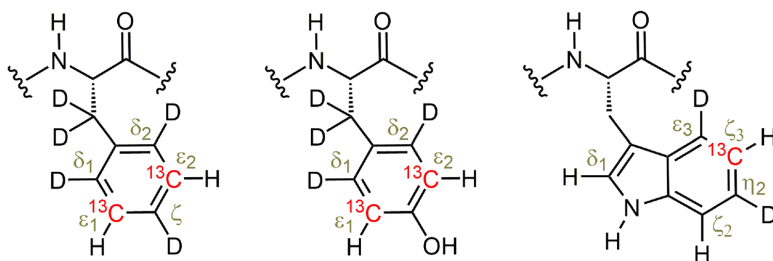
It is expected that ^1H $R_{1\rho}$ experiments make it possible to access faster time scales, since the attainable refocusing frequency scales with the gyromagnetic ratio and the RF field amplitude, $\omega_1 = \gamma B_1$. ^1H $R_{1\rho}$ experiments have successfully been applied to the aromatic position H8 of adenine and guanine and in RNA (Steiner et al. 2016), which is not affected by sizeable $^3J_{\text{HH}}$ couplings or cross relaxation with remote protons. The situation is more challenging in certain aromatic protein residues, where $^3J_{\text{HH}}$ is on the order of 7–8 Hz and the chemical shift difference between vicinal ring protons is often small. Here we demonstrate these problems can be solved by site-selective ^1H - $^{13}\text{C}/^2\text{H}$ - ^{12}C labeling, which is necessary and sufficient to ensure artifact-free ^1H $R_{1\rho}$ relaxation dispersion data for aromatic side chains in proteins.

Materials and methods

Protein samples

The B1 domain of the bacterial antibody-binding protein G (GB1) containing the mutations T2Q, N8D and N37D (QDD variant) was expressed and purified as described previously (Lindman et al. 2006), with three different labeling patterns: (i) site-selective $^{13}\text{C}/^{12}\text{C}$ using 2- $^{13}\text{C}_1$ glucose with natural abundance ^1H incorporation (Lundström et al. 2007), (ii) site-selective ^1H - $^{13}\text{C}/^2\text{H}$ - ^{12}C labeling protein (Fig. 1) using site-selectively $^1\text{H}/^2\text{H}$ and ^{13}C labeled -ketoacids as precursors (Lichtenecker 2014; Lichtenecker et al. 2013), 80 mg/L for Phe, 350 mg/L for Tyr, 10 mg/L for Trp, (iii) same as (ii) but with additional 70% background deuteration by expression in D_2O (implemented only in the case of Phe ϵ^*). NMR samples contained around 1 mM protein in 20 mM HEPES, 90% $\text{H}_2\text{O}/10\%$ D_2O with addition of small amounts of NaN_3 . The pH of the NMR samples was adjusted to 7.0.

Fig. 1 Labeling patterns in Phe, Tyr and Trp (from left to right), using site-selectively $^1\text{H}/^2\text{H}$ and ^{13}C labeled -ketoacids as precursors (Lichtenecker 2014; Lichtenecker et al. 2013). Protons and deuterons are displayed by H and D, respectively. ^{13}C is shown in red, other carbon positions are ^{12}C



NMR spectroscopy

All experiments were acquired on a Bruker Avance III spectrometer at a static magnetic field strength of 14.1 T, equipped with a room temperature probe. ^1H $R_{1\rho}$ relaxation dispersion experiments were performed using the pulse sequence shown in Fig. 2, with spectral widths of 14.0 ppm (^1H) and 30.0 ppm (^{13}C), by 1024 and 128 points, respectively. Nineteen experiments were performed at temperatures of 15, 20, 25, 30 and 35 °C. $R_{1\rho}$ rate constants were measured in separate experiments conducted on-resonance with the signal of interest resulting in tilt angles of 90° from the z-axis, using a constant-time relaxation period (Mulder et al. 2001) of 20 ms and spin-lock field strengths varying between 1000 and 9000 Hz; the 4-ms adiabatic ramps used to align the magnetization along the effective spin-lock field do not achieve perfect alignment below 1000 Hz. Spectra were processed with NMRPipe (Delaglio et al. 1995) and analyzed with PINT (Ahlner et al. 2013).

Data analysis

Relaxation rates in the rotating reference frame were calculated from the signal intensities measured in presence and absence of the spin-lock pulse, $I(\omega_1)$ and I_0 , respectively, according to (Mulder et al. 2001)

$$R_{1\rho}(\omega_1) = -\frac{1}{T_{\text{SL}}} \ln \frac{I(\omega_1)}{I_0} \quad (1)$$

$R_{1\rho}$ relaxation dispersions were fitted to the general equation for symmetric exchange derived by Miloushev and Palmer (2005) using fixed populations, $p_1 = p_2 = 0.5$, and treating $\Delta\delta$ as a free parameter, which was compared to values measured under slow-exchange conditions at -5 °C and 200 MPa. Data modeling utilized the Levenberg–Marquardt nonlinear least-squares optimization algorithm (Press et al. 2002) implemented in MATLAB. Errors in the fitted parameters were estimated using 1000 Monte-Carlo simulations per fit; the reported errors correspond to one standard deviation.

Activation parameters of the ring flips were determined by non-linear regression of the flip rates, $k_{\text{flip}} = k_{\text{ex}}/2$, on the temperature T , using the Eyring equation. The Eyring equation was parameterized as

$$k_{\text{flip}} = \left(\frac{k_{\text{B}}T}{h} \right) \times \exp[-(\Delta H^\ddagger - T\Delta S^\ddagger)/RT] \quad (2)$$

where k_{B} and h denote Boltzmann's and Planck's constants, respectively, and ΔH^\ddagger and ΔS^\ddagger are the activation enthalpy and activation entropy, respectively.

Hartmann–Hahn transfer calculations

A nucleus affected by a spin-lock radio frequency pulse with field strength $\omega_1 = -\gamma B_1$ will perceive an effective

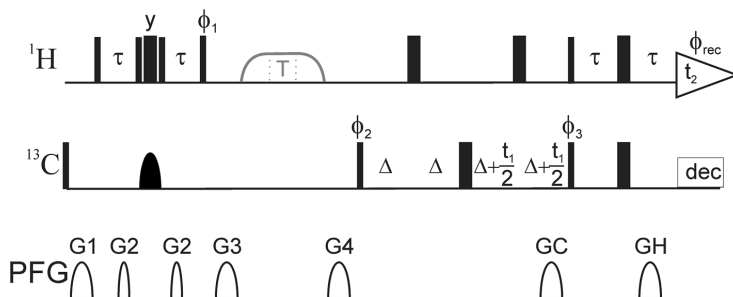


Fig. 2 Pulse sequence for the ^1H $R_{1\rho}$ constant-time relaxation dispersion experiment for measuring conformational exchange of aromatic side chains in specifically ^1H - ^{13}C / ^1H - ^{12}C labeled proteins. All pulses are applied along the x -axis unless otherwise indicated. Narrow (wide) solid bars indicate rectangular high-power 90° (180°) pulses. The continuous-wave spin-lock relaxation periods T and their flanking 4 ms tan/tanh adiabatic profiles (Mulder et al. 1998) are outlined in gray. The adiabatic sweep is initiated 25 kHz downfield or upfield of the spin-lock frequency. The wide semi-ellipse on ^{13}C represents a REBURP (Geen and Freeman 1991) pulse with a bandwidth of 40 ppm. The pulse sequence can be modified to accommodate non-constant relaxation periods or off-resonance spin-locks by including a pair of ^{13}C 180° pulses to mitigate the effects of dipole-dipole/

CSA cross-correlated relaxation (Korzhev et al. 2002; Massi et al. 2004). The delay τ can be set to 1.6 ms (Phe and Tyr), 1.35 ms (all aromatics) or 1.25 ms (His). The phase cycle is: $\phi_1 = (4y, 4-y)$, $\phi_2 = (x, -x)$, $\phi_3 = (x, x, -x, -x)$, $\phi_{\text{rec}} = (x, -x, -x, x, -x, x, x, -x)$. Pulsed field gradients G1–4 are employed to suppress unwanted coherences and artifacts, while GC and GH are encoding and decoding gradients, respectively, for echo/anti-echo coherence selection, obtained by inverting the signs of GH (Kay et al. 1992). The delay Δ is equal to GC. For every second t_1 increment ϕ_2 and the receiver were incremented. Gradient durations (in ms) and relative power levels (in %) are set to (duration, power level) G1=(1.0, 13), G2=(0.5, 10), G3=(1.0, 30), G4=(1.0, 90), GC=(1.0, 80), GH=(1.0, -20.1)

field strength $\omega_{\text{eff}} = (\Omega^2 + \omega_1^2)^{1/2}$ and will be oriented at an angle $\theta = \tan^{-1}(\omega_1/\Omega)$ from the static magnetic field, with $\Omega = \omega_0 - \omega_c$ denoting the offset between the nuclear precession frequency ω_0 and the carrier frequency ω_c of the spin-lock pulse. In the case of two spins I and S , coupled by a scalar-coupling constant J , Hartmann–Hahn matching of the two effective fields causes magnetization transfer between them, according to the coherence transfer function given by (Brath et al. 2006; van de Ven 1995)

$$F_{\text{HaHa}} = A_{\text{HaHa}} \sin^2(DT_{\text{SL}}/2) \quad (3)$$

where T_{SL} is the duration of the spin-lock period, $D = (\Delta^2 + J_{\text{eff}}^2)^{1/2}$, $\Delta = \omega_{\text{eff},I} - \omega_{\text{eff},S}$, $J_{\text{eff}} = \frac{1}{2}J(1 + \cos(\theta_I - \theta_S))$ and A_{HaHa} is the coherence transfer amplitude

$$A_{\text{HaHa}} = \frac{1}{1 + (\Delta/J_{\text{eff}})^2} \quad (4)$$

Hartmann–Hahn mediated magnetization transfer from the monitored proton of the ^1H - ^{13}C moiety to vicinal protons in the aromatic ring scales the intensity by a factor of $1 - F_{\text{HaHa}}(\omega_1)$ for a given spin-lock period T_{SL} . Consequently, the apparent $R_{1\rho}$ rate constant is given by:

$$R_{1\rho,\text{app}}(\omega_1) = -\frac{1}{T_{\text{SL}}} \left(\ln \frac{I(\omega_1)}{I_0} + \ln(1 - F_{\text{HaHa}}(\omega_1)) \right) \quad (5)$$

where the first term describes the $R_{1\rho}$ rate constant according to Eq. (1), i.e., in the absence of Hartmann–Hahn matching. Similarly, as a first approximation, in the case of n protons coupled to the monitored proton, the apparent rate constant is:

$$R_{1\rho,\text{app}}(\omega_1) = -\frac{1}{T_{\text{SL}}} \left(\ln \frac{I(\omega_1)}{I_0} + \sum_i^n \ln(1 - F_{\text{HaHa},i}(\omega_1)) \right) \quad (6)$$

A_{HaHa} and F_{HaHa} were calculated for scalar-coupled protons in the aromatic rings of GB1 using $J = {}^3J_{\text{HH}} = 7$ Hz, $T_{\text{SL}} = 20$ ms, and the resonance frequencies measured in the spectrum acquired at 25 °C: 0.22 ppm between Y33 ϵ^* and δ^* ; 0.65 ppm (0.16 ppm) between F52 ϵ^* and $\delta^*(\zeta)$; and 0.98 ppm (0.13 ppm) between W43 $\zeta 3$ and $\epsilon 3$ ($\eta 2$). In case of frequencies averaged by fast ring-flips, i.e. δ^* and ϵ^* in Phe and Tyr, it is sufficient to use them directly.

Results and discussion

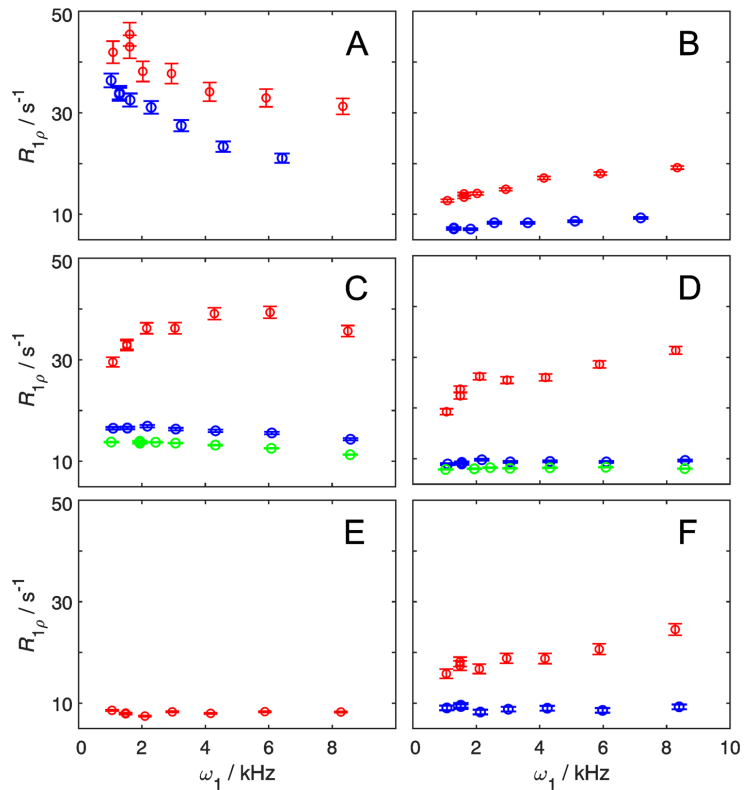
We performed aromatic ^1H $R_{1\rho}$ relaxation dispersion experiments on the small protein domain GB1, ^1H - ^{13}C labeled in three different ways: (i) natural abundance protonation

and site selective $^{13}\text{C}/^{12}\text{C}$ labeling; (ii) additional selective deuteration of vicinal hydrogen sites in order to eradicate ${}^3J_{\text{HH}}$ couplings resulting in site-selective ^1H - $^{13}\text{C}/^2\text{H}$ - ^{12}C labeling (Fig. 1); or (iii) as (ii) with additional non-specific background deuteration at a level of 70%. There are five symmetric aromatic residues (Phe and Tyr) in GB1: Y3, F30, Y33, Y45 and F52. All but Y33 undergo relatively slow ring-flip processes that have been studied by aromatic ^{13}C $R_{1\rho}$ relaxation dispersion experiments (Dreydoppel et al. 2020); in particular Y3 δ , Y3 ϵ , F30 δ , Y45 ϵ and F52 ϵ have been studied previously and provide valuable points of reference for comparison with our present work. Individual cross peaks from the two symmetric sites of the aromatic rings could be observed under slow exchange conditions (−5 °C, 200 MPa) for Y3 δ , Y3 ϵ , F30 δ , F30 ϵ and F52 ϵ . Based on these results, the following ^{13}C and ^1H chemical shift differences could be extracted: Y3 δ (2.11 ppm; 0.40 ppm), Y3 ϵ (1.40 ppm; 0.50 ppm), F30 δ (5.39 ppm; 0.84 ppm), F30 ϵ (0.00 ppm; 0.56 ppm) and F52 ϵ (1.76 ppm; 0.00 ppm). F52 ϵ , which has a ^1H chemical shift difference of zero, serves as a negative control in the present study, since it should not exhibit any exchange-mediated dependence of the $R_{1\rho}$ rate constant on the spin-lock field strength. In addition, Y33 ϵ , which is solvent exposed and undergoing very fast ring flips, is also expected to show an essentially flat dispersion profile. Furthermore, the two labeled sites in tryptophan, W43 $\delta 1$ and W43 $\zeta 3$ also serve as useful controls: W43 $\delta 1$ does not experience sizeable ${}^3J_{\text{HH}}$ couplings, and neither site undergoes exchange, since this residue does not readily undergo ring flips. In a previous study, site-selective ^1H - $^{13}\text{C}/^2\text{H}$ - ^{12}C labeling resulted in 99% correct labeling in case of Phe ϵ^* and 75% in case of Trp $\zeta 3$, whereas Tyr ϵ^* labeling yielded only 4% incorporation for reasons that are not clear (Raum et al. 2019). Here, we increased the amount of tyrosine precursor fourfold in the protein expression medium, resulting in 17% of the desired labeling for Tyr ϵ^* , while the remaining 83% have natural abundance isotope incorporation. Therefore, 0.9% of the sample is ^{13}C labeled at Tyr ϵ and protonated at the δ position. Thus, in the present sample the latter isotope is diluted by a factor of 20 compared to the desired one, which is sufficient to suppress ${}^3J_{\text{HH}}$ coupling artifacts.

Deuteration of vicinal protons is necessary in order to achieve artifact-free aromatic ^1H $R_{1\rho}$ relaxation dispersion profiles

Figure 3 shows the resulting ^1H $R_{1\rho}$ relaxation dispersion profiles for the ^1H - ^{13}C labeled ϵ sites of residues Y3, Y33, F30, and F52 (a–d), and for the $\delta 1$ and $\zeta 3$ sites of W43 (e–f). There is a notable variation among the dispersion profiles of the different residues and between the two $^1\text{H}/^2\text{H}$ labeling patterns for each residue. The non-deuterated samples of residues Y33 ϵ , F30 ϵ , F52 ϵ , and W43 $\zeta 3$ (Figs. 3b–d and

Fig. 3 Aromatic ^1H $R_{1\rho}$ relaxation dispersions recorded on-resonance (tilt angle $\theta=90^\circ$ from the z-axis) at a static magnetic field-strength of 14.1 T and a temperature of 25 °C. Dispersion profiles obtained from uniformly protonated and site-selectively $^{13}\text{C}/^{12}\text{C}$ labeled samples are shown in red, from site-selectively $^1\text{H}-^{13}\text{C}/^2\text{H}-^{12}\text{C}$ labeled samples in blue, and site-selectively $^1\text{H}-^{13}\text{C}/^2\text{H}-^{12}\text{C}$ labeled samples with additional 70% background deuteration in green. Dispersion profiles are shown for Y3e (A), Y33e (B), F30e (C), F52e (D), W4361 (E) and W43ζ3 (F)



f; red symbols) all exhibit anomalous, ‘inverted’ relaxation dispersion profiles characteristic of sizeable (7–8 Hz) $^3J_{\text{HH}}$ coupling (Raum et al. 2018). In contrast, the dispersion profile of Y3e (Fig. 3a) does not appear anomalous, because the effect of Hartmann–Hahn matching is in part masked by a substantial chemical exchange contribution. In general, the magnitude of the artifact is more pronounced in the case of Phe (Fig. 3c, d) compared to Tyr (Fig. 3a, b), because the investigated ^1H spins in Phe couple to two vicinal proton spins (δ and ζ) instead of one (δ) in Tyr. In the case of Trp ζ 3, the magnitude is closer to the Tyr case. In the non-deuterated sample, W4361 displays a flat relaxation dispersion profile (Fig. 3e), as a result of its small coupling constant, $^3J_{\text{HH}} < 2$ Hz, and absence of exchange. This result is in keeping with the expectation outlined above regarding the role of W4361 as a negative control.

Site-selective deuteration of the vicinal hydrogen sites efficiently removes the effect of $^3J_{\text{HH}}$ coupling, resulting in ‘normal’-looking relaxation dispersion profiles (Fig. 3; blue symbols). Y33e, F52e, and W43ζ3 (Figs. 3b, d, f) show flat dispersion profiles in the deuterated sample, again in agreement with expectations (very fast exchange,

no ^1H chemical shift difference between the symmetric sites, and no exchange, respectively; see above). In the case of F30e, the site-selectively deuterated sample reveals a fast exchange process that is completely hidden by the strong-coupling effect in the protonated sample (Fig. 3c). Finally, for Y3e where the relaxation dispersion profile shows clear signs of exchange even in the non-deuterated sample, the profile is more pronounced in case of site-selective deuteration (Fig. 3a). This comparison clearly shows that the Y3e profile in the non-deuterated sample is compromised and cannot be analyzed to yield reliable exchange parameters. Additional, unspecific 70% background deuteration of the protein does slightly shift the ^1H $R_{1\rho}$ to lower values, but does not alter the profile shape (Fig. 3c, d, green symbols). A quantitative analysis comparing the results obtained from the samples with or without background deuteration shows that identical exchange parameters are obtained, within the margin of error (see below). This result demonstrates that site-selective deuteration in the aromatic ring alone is sufficient to obtain artifact free relaxation dispersion profiles, and further indicates that long-range ROE effects (Lundström and

Akke 2005; Weinger et al. 2013a) do not cause concern in the present case.

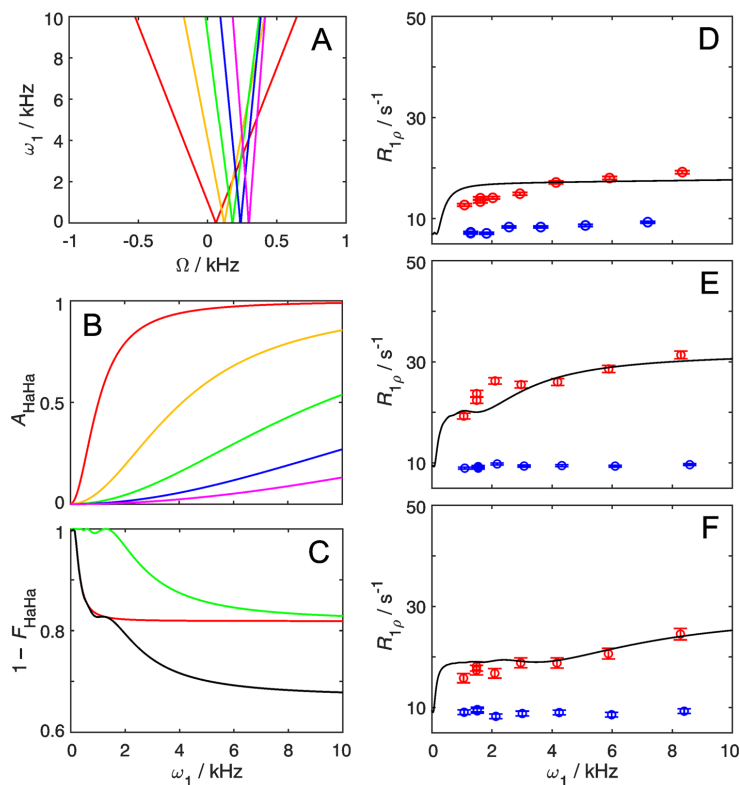
Taken together, the present results illustrate the detrimental effects of $^3J_{\text{HH}}$ couplings on the relaxation dispersion data obtained on non-deuterated samples, and clearly demonstrate that high-quality ^1H $R_{1\rho}$ relaxation dispersion profiles can only be obtained using samples with site-selective deuteration. Our present approach enables ^1H $R_{1\rho}$ relaxation dispersion experiments for Phe, Tyr, and Trp $\zeta 3$, and thus completes the repertoire of probes to cover all aromatic ^1H - ^{13}C positions. By contrast, only Trp $\delta 1$, His $\delta 2$ and His $\epsilon 1$ are accessible also in non-deuterated samples, because these positions do not involve sizeable scalar coupling to vicinal protons.

Hartmann–Hahn transfer explains artifacts in aromatic ^1H $R_{1\rho}$ relaxation dispersion experiments

The artifacts described above for the non-deuterated samples (Fig. 3) can be rationalized as increased homonuclear Hartmann–Hahn transfer from the proton of interest (I) to

a scalar coupled vicinal proton (S) with increasing spin-lock field strength (ω_1). Figure 4 shows the expected values of the amplitude (A_{HaHa}) of the transfer function and the relative loss of magnetization for spin I ($1-F_{\text{HaHa}}$), as a function of the spin-lock field strength and the difference in offset between spins I and S ; see Eqs. (3–5). The magnetization loss expected for the case where spin I has two J -coupled vicinal protons, as for Phe ϵ , is included in Fig. 4c; see Eq. (6). We calculated the amount of magnetization lost from I during the spin-lock period for those residues that do not show exchange contributions to $R_{1\rho}$ (Y33 ϵ , F52 ϵ , and W43 $\zeta 3$), and estimated their resulting apparent $R_{1\rho}$ rate constant as a function of ω_1 . To do so, we took the average $R_{1\rho}$ rate constant measured on site-selectively ^1H - $^{13}\text{C}/^2\text{H}$ - ^{12}C labeled samples to represent the artifact-free first term of Eq. (6), and added the second term involving the calculated value of $(1-F_{\text{HaHa}})$. As shown in Figs. 4d–f, in all three cases the experimental data points acquired on the uniformly protonated sample are reproduced well by the calculated function describing the apparent $R_{1\rho}$ values. Thus, Hartmann–Hahn transfer quantitatively explains the observed artifacts in aromatic

Fig. 4 Hartmann–Hahn coherence transfer between spin-locked proton spins. The carrier frequency of the spin-lock is chosen to match the resonance frequency of spin I . **A** Contour levels of the coherence transfer amplitude, $A_{\text{HaHa}}=0.5$, as a function of the spin-lock ω_1 and the resonance offset from the spin-lock carrier for spin S , Ω . Contour lines are shown for various differences in resonance frequency offsets between the coupled nuclei: 0.2 ppm (red), 0.4 ppm (yellow), 0.6 ppm (green), 0.8 ppm (blue) and 1.0 ppm (magenta). **B** A_{HaHa} plotted as a function of spin-lock field strength for different resonance frequency offsets as in (A). **C** Loss of coherence according to the transfer function, $1-F_{\text{HaHa}}$, for resonance frequency offsets of 0.2 ppm (red) and 0.6 ppm (green), and the product of both (black). **D–F** Measured data points from Y33 ϵ (D), F52 ϵ (E), and W43 $\zeta 3$ (F) as given in Fig. 3, together with predicted apparent $R_{1\rho}$ dispersion profiles (black lines), calculated using Eq. 6 and the artifact-free data measured on deuterated samples (blue points)



^1H $R_{1\rho}$ relaxation dispersion experiments acquired on uniformly protonated samples.

Comparison of ring flip rates of ^1H and ^{13}C based aromatic $R_{1\rho}$ relaxation dispersion experiments

We acquired relaxation dispersion profile for Y3e and F30e in the site-selectively deuterated sample at three different temperatures (Fig. 5). The artifact-free relaxation dispersions could be fitted to the general equation for symmetric exchange, resulting in flip rates at each temperature together with a global chemical shift difference for each residue (Table 1). The derived chemical shift differences are $\Delta\delta = (0.46 \pm 0.03)$ ppm for Y3e and (0.47 ± 0.02) ppm for F30e, in good agreement with the values measured in the spectrum under slow exchange conditions (0.50 ppm and 0.56 ppm, respectively). In the case of Y3e, the resulting flip rates are virtually the same, within the margin of error, as those determined from ^{13}C based experiments (Fig. 6a, Table 1). Consequently, the activation enthalpy (ΔH^\ddagger) and activation entropy (ΔS^\ddagger) determined from the temperature dependence of the flip rates are identical within the margin of error to previous estimates (Fig. 6a): $\Delta H^\ddagger = (82 \pm 8)$ kJ mol $^{-1}$ for ^1H versus (87 ± 14) kJ mol $^{-1}$ for ^{13}C ; and $\Delta S^\ddagger = (111 \pm 26)$ J mol $^{-1}$ K $^{-1}$ versus (126 ± 46) J mol $^{-1}$ K $^{-1}$. In case of F30e, we cannot directly compare flip rates determined by ^1H and ^{13}C $R_{1\rho}$ experiments, because its $^{13}\text{C}\epsilon$ chemical shift difference is zero. However, ring flip rates have been measured for F30 δ using ^{13}C $R_{1\rho}$ relaxation experiments at two higher temperatures, although the flip rate is far outside the optimal range of the $R_{1\rho}$ experiment in this case and should only be interpreted semi-quantitatively (Fig. 6b). At lower temperatures F30 δ becomes broadened beyond detection, because of its large $^{13}\text{C}\delta$ chemical shift difference. The rates derived from the ^1H $R_{1\rho}$ experiments seem to be a bit higher (as gauged from the extrapolated line in Fig. 6b), although the two data points from the ^{13}C $R_{1\rho}$ experiments seem to follow the temperature dependence determined from the ^1H $R_{1\rho}$ experiments. Background deuteration in the F30e sample leads to a minor improvement of the fit in the region of the highest refocusing frequencies (Fig. 5 bc), where the ROE effect is the most severe. The derived values of ΔH^\ddagger and ΔS^\ddagger with and without background deuteration are also identical, within the margin of error (Fig. 6b): $\Delta H^\ddagger = (47 \pm 4)$ kJ mol $^{-1}$ for ^1H with protonated background versus (50 ± 1) kJ mol $^{-1}$ with deuterated background; and $\Delta S^\ddagger = (0 \pm 13)$ J mol $^{-1}$ K $^{-1}$ versus (10 ± 4) J mol $^{-1}$ K $^{-1}$. In summary, aromatic ^1H $R_{1\rho}$ experiments allow the determination of correct exchange parameters, provided that the aromatic ring

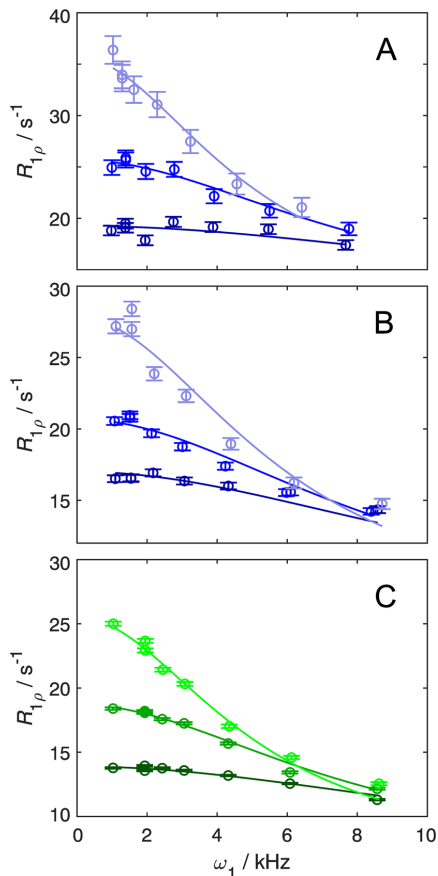


Fig. 5 Temperature dependent aromatic ^1H $R_{1\rho}$ relaxation dispersion data. Experiments were recorded on-resonance ($\theta = 90^\circ$ from the z-axis) on site-selectively ^1H - $^{13}\text{C}/^2\text{H}$ - ^{12}C labeled GB1 at pH 7.0 and a static magnetic field strength of 14.1 T. Data of Y3e acquired at 25 °C, 30 °C, and 35 °C and F30e at 15 °C, 20 °C, and 25 °C are represented by light, medium, and dark hues, respectively. **A** Y3e (blue), **B** F30e (blue), and **C** F30e with additionally 70% deuterated background (green). The relaxation dispersions were fitted using a fixed population $p_1 = p_2 = 0.5$ and $\Delta\delta$ as a free parameter with the restrictions: $k_{\text{flip}}(T_{\text{high}}) > k_{\text{flip}}(T_{\text{low}})$, $R_{2,0}(T_{\text{high}}) \leq R_{2,0}(T_{\text{low}})$. The derived ring flip rate constants (k_{flip}) are given in Table 1

is site-selectively $^1\text{H}/^2\text{H}$ labeled; further deuteration of the background is not needed.

Concluding remarks

There are multiple positions available in aromatic side chains that are suitable for studying exchange dynamics. However, it is not uncommon that certain sites do not experience sufficiently large $\Delta\delta$ for a given nucleus, or experience

Table 1 Ring flip rates and chemical shift differences

	Y3 ^a	Y3 ^b	F30 ^a	F30 ^c	F30 ^b
$\Delta\delta(\text{ppm})$	0.46 ± 0.03	0.50	0.47 ± 0.02	0.49 ± 0.02	0.56
$k_{\text{flip}} (10^3 \text{ s}^{-1})$					
15 °C			18 ± 1	20 ± 1	
20 °C			28 ± 1	29 ± 1	
25 °C	15 ± 2	12 ± 2	37 ± 1	42 ± 1	
30 °C	26 ± 2	22 ± 3			
35 °C	46 ± 3	38 ± 4			53 ± 4
40 °C					75 ± 8

^aDerived from aromatic ^1H $R_{1\rho}$ relaxation dispersion experiments on position ϵ of site-selective deuterated samples with protonated background

^bTaken from (Dreydoppel et al. 2020); chemical shift difference of position ϵ are derived from spectra under slow exchange conditions; ring flip rates are derived from aromatic ^{13}C $R_{1\rho}$ relaxation dispersion experiments on Y3 $^{13}\text{C}\delta$ and F30 $^{13}\text{C}\delta$. In the case of F30 the flip rates are clearly outside the optimal range of the experiment and should only be interpreted semi-quantitatively

^cDerived from aromatic ^1H $R_{1\rho}$ relaxation dispersion experiments on position ϵ of site-selective deuterated samples with deuterated background

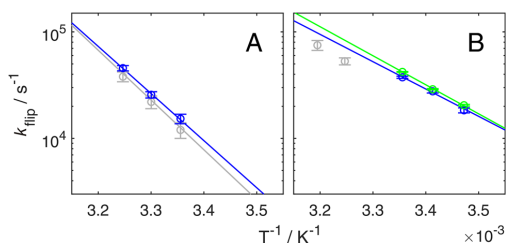


Fig. 6 Temperature dependence of ring-flip rates. k_{flip} is plotted as a function of $1/T$. **A** Y3e and **B** F30e flip rates determined from aromatic ^1H $R_{1\rho}$ relaxation dispersion measurements are shown in blue (protonated background) and green (deuterated background), and from previous ^{13}C $R_{1\rho}$ relaxation dispersion measurements in grey (Dreydoppel et al. 2020). Solid lines represent non-linear regression of k_{flip} on T according to the Eyring equation, displayed on a logarithmic y-axis to show the expected linearity. Derived activation enthalpies (ΔH^\ddagger) and entropies (ΔS^\ddagger) are: Y3 ^1H (protonated background), (82 ± 8) kJ mol⁻¹ and (111 ± 26) J mol⁻¹ K⁻¹ (A, blue); Y3 ^{13}C (87 ± 14) kJ mol⁻¹ and (126 ± 46) J mol⁻¹ K⁻¹ (A, grey); F30 ^1H (protonated background), (47 ± 4) kJ mol⁻¹ and (0 ± 13) J mol⁻¹ K⁻¹ (B, blue); F30 ^1H (deuterated background), (50 ± 1) kJ mol⁻¹ and (10 ± 4) J mol⁻¹ K⁻¹ (B, green)

exchange rates outside of the optimal relaxation dispersion window for a given nuclide (e.g., ^1H or ^{13}C). Thus, it is highly advantageous to be able to measure exchange using different nuclides, so as to probe as many sites as possible in a given protein. For example, our studies of ring flip dynamics in GB1 highlight the advantage of using both ^1H and ^{13}C based experiments: Y3 can be probed using all four positions ($^1\text{H}\delta$, $^{13}\text{C}\delta$, $^1\text{H}\epsilon$ and $^{13}\text{C}\epsilon$), while F30 and F52 can each be probed using only a single probe ($^1\text{H}\epsilon$ and $^{13}\text{C}\epsilon$, respectively). Our present approach extends the available toolbox to make all aromatic positions accessible by NMR relaxation dispersion experiments using either CPMG or

$R_{1\rho}$ refocusing elements. The higher effective field strength available in ^1H $R_{1\rho}$ experiments is clearly of advantage in this context, and allows to reliably study exchange processes up to an exchange rate of about 80,000 s⁻¹ (equal to a flip rate of 40,000 s⁻¹).

Acknowledgements This research was supported by the Deutsche Forschungsgemeinschaft (WE 5587/1-2 to UW) and the Swedish Research Council (2018-4995 to MA).

Funding Open Access funding enabled and organized by Projekt DEAL.

Data availability All data generated or analysed during this study are included in this published article.

Open Access This article is licensed under a Creative Commons Attribution 4.0 International License, which permits use, sharing, adaptation, distribution and reproduction in any medium or format, as long as you give appropriate credit to the original author(s) and the source, provide a link to the Creative Commons licence, and indicate if changes were made. The images or other third party material in this article are included in the article's Creative Commons licence, unless indicated otherwise in a credit line to the material. If material is not included in the article's Creative Commons licence and your intended use is not permitted by statutory regulation or exceeds the permitted use, you will need to obtain permission directly from the copyright holder. To view a copy of this licence, visit <http://creativecommons.org/licenses/by/4.0/>.

References

- Ahlner A, Carlsson M, Jonsson BH, Lundström P (2013) PINT: a software for integration of peak volumes and extraction of relaxation rates. *J Biomol NMR* 56:191–202. <https://doi.org/10.1007/s10858-013-9737-7>
- Akke M, Palmer AG (1996) Monitoring Macromolecular motions on microsecond-millisecond time scales by $R_{1\rho}$ - R_1 constant-relaxation-time NMR spectroscopy. *J Am Chem Soc* 118:911–912

- Bartlett GJ, Porter CT, Borkakoti N, Thornton JM (2002) Analysis of catalytic residues in enzyme active sites. *J Mol Biol* 324:105–121
- Birtalan S, Fisher RD, Sidhu SS (2010) The functional capacity of the natural amino acids for molecular recognition. *Mol Biosyst* 6:1186–1194. <https://doi.org/10.1039/b927393j>
- Boehr DD, McElheny D, Dyson HJ, Wright PE (2006) The dynamic energy landscape of dihydrofolate reductase catalysis. *Science* 313:1638–1642
- Bogan AA, Thorn KS (1998) Anatomy of hot spots in protein interfaces. *J Mol Biol* 280:1–9
- Boyer JA, Lee AL (2008) Monitoring aromatic picosecond to nanosecond dynamics in proteins via C-13 relaxation: expanding perturbation mapping of the rigidifying core mutation, V54A, in Eglin C. *Biochemistry* 47:4876–4886
- Brath U, Akke M, Yang DW, Kay LE, Mulder FAA (2006) Functional dynamics of human FKBP12 revealed by methyl C-13 rotating frame relaxation dispersion NMR spectroscopy. *J Am Chem Soc* 128:5718–5727
- Burley SK, Petsko GA (1985) Aromatic-aromatic interaction: a mechanism of protein structure stabilization. *Science* 229:23–28
- Burley SK, Petsko GA (1989) Electrostatic interactions in aromatic oligopeptides contribute to protein stability trends. *Biotech* 7:354–359
- Carr HY, Purcell EM (1954) Effects of diffusion on free precession in nuclear magnetic resonance experiments. *Phys Rev* 94:630–638
- Cole R, Loria JP (2002) Evidence for flexibility in the function of ribonuclease A. *Biochemistry* 41:6072–6081
- Delaglio F, Grzesiek S, Vuister GW, Zhu G, Pfeifer J, Bax A (1995) Nmrpipe - a multidimensional spectral processing system based on inix pipes. *J Biomol NMR* 6:277–293
- Demers JP, Mittermaier A (2009) Binding mechanism of an SH3 domain studied by NMR and ITC. *J Am Chem Soc* 131:4355–4367. <https://doi.org/10.1021/ja808255d>
- Dreydoppel M, Raum HN, Weininger U (2020) Slow ring flips in aromatic cluster of GB1 studied by aromatic C-13 relaxation dispersion methods. *J Biomol NMR* 74:183–191. <https://doi.org/10.1007/s10858-020-00303-3>
- Eisenmesser EZ, Bosco DA, Akke M, Kern D (2002) Enzyme dynamics during catalysis. *Science* 295:1520–1523
- Forsen S, Hoffman RA (1963) Study of moderately rapid chemical exchange reactions by means of nuclear magnetic double resonance. *J Chem Phys* 39:2892–3000. <https://doi.org/10.1063/1.1734121>
- Geen H, Freeman R (1991) Band-selective radiofrequency pulses. *J Magn Reson* 93:93–141. [https://doi.org/10.1016/0022-2364\(91\)90034-Q](https://doi.org/10.1016/0022-2364(91)90034-Q)
- Gutowsky HS, Saika A (1953) Dissociation, chemical exchange, and the proton magnetic resonance in some aqueous electrolytes. *J Chem Phys* 21:1688–1694
- Igumenova TI, Brath U, Akke M, Palmer AG (2007) Characterization of chemical exchange using residual dipolar coupling. *J Am Chem Soc* 129:13396
- James TL, Matson GB, Kuntz ID, Fisher RW (1977) Rotating frame spin-lattice relaxation in presence of an off-resonance radio-frequency field - investigation of intermediate molecular motions. *J Magn Reson* 28:417–426. [https://doi.org/10.1016/0022-2364\(77\)90283-9](https://doi.org/10.1016/0022-2364(77)90283-9)
- Kasinath V, Valentine KG, Wand AJ (2013) A C-13 labeling strategy reveals a range of aromatic side chain motion in Calmodulin. *J Am Chem Soc* 135:9560–9563
- Kasinath V, Fu YN, Sharp KA, Wand AJ (2015) A sharp thermal transition of fast aromatic-ring dynamics in ubiquitin. *Angew Chem Int Edit* 54:102–107
- Kay LE, Keifer P, Saarinen T (1992) Pure absorption gradient enhanced heteronuclear single quantum correlation spectroscopy with improved sensitivity. *J Am Chem Soc* 114:10663–10665. <https://doi.org/10.1021/Ja00052a088>
- Korzhev DM, Skrynnikov NR, Millet O, Torchia DA, Kay LE (2002) An NMR experiment for the accurate measurement of heteronuclear spin-lock relaxation rates. *J Am Chem Soc* 124:10743–10753. <https://doi.org/10.1021/ja0204776>
- Lichtenecker RJ (2014) Synthesis of aromatic C-13/H-2-alpha-ketoacid precursors to be used in selective phenylalanine and tyrosine protein labelling. *Org Biomol Chem* 12:7551–7560. <https://doi.org/10.1039/c4ob01129e>
- Lichtenecker RJ, Weinhaupl K, Schmid W, Konrat R (2013) alpha-Ketoacids as precursors for phenylalanine and tyrosine labelling in cell-based protein overexpression. *J Biomol NMR* 57:327–331
- Lindman S, Xue WF, Szczepankiewicz O, Bauer MC, Nilsson H, Linse S (2006) Salting the charged surface: pH and salt dependence of protein G B1 stability. *Biophys J* 90:2911–2921. <https://doi.org/10.1529/biophysj.105.071050>
- Lo Conte L, Chothia C, Janin J (1999) The atomic structure of protein-protein recognition sites. *J Mol Biol* 285:2177–2198
- Loria JP, Rance M, Palmer AG (1999a) A relaxation-compensated Carr-Purcell-Meiboom-Gill sequence for characterizing chemical exchange by NMR spectroscopy. *J Am Chem Soc* 121:2331–2332
- Loria JP, Rance M, Palmer AG (1999b) A TROSY CPMG sequence for characterizing chemical exchange in large proteins. *J Biomol NMR* 15:151–155
- Lundström P, Akke M (2005) Off-resonance rotating-frame amide proton spin relaxation experiments measuring microsecond chemical exchange in proteins. *J Biomol NMR* 32:163–173. <https://doi.org/10.1007/s10858-005-5027-3>
- Lundström P et al (2007) Fractional C-13 enrichment of isolated carbons using [1-C-13]- or [2-C-13]-glucose facilitates the accurate measurement of dynamics at backbone C-alpha and side-chain methyl positions in proteins. *J Biomol NMR* 38:199–212
- Malmendal A, Evenas J, Forsen S, Akke M (1999) Structural dynamics in the C-terminal domain of calmodulin at low calcium levels. *J Mol Biol* 293:883–899
- Massi F, Johnson E, Wang C, Rance M, Palmer AG 3rd (2004) NMR R1 rho rotating-frame relaxation with weak radio frequency fields. *J Am Chem Soc* 126:2247–2256. <https://doi.org/10.1021/ja038721w>
- Meiboom S, Gill D (1958) Modified spin-echo method for measuring nuclear relaxation times. *Rev Sci Instrum* 29:688–691
- Miloushev VZ, Palmer AG (2005) R(1p) relaxation for two-site chemical exchange: general approximations and some exact solutions. *J Magn Reson* 177:221–227. <https://doi.org/10.1016/j.jmr.2005.07.023>
- Mittermaier AK, Kay LE (2009) Observing biological dynamics at atomic resolution using NMR. *Trends Biochem Sci* 34:601–611
- Mulder FAA, de Graaf RA, Kaptein R, Boelens R (1998) An off-resonance rotating frame relaxation experiment for the investigation of macromolecular dynamics using adiabatic rotations. *J Magn Reson* 131:351–357. <https://doi.org/10.1006/jmre.1998.1380>
- Mulder FAA, Skrynnikov NR, Hon B, Dahlquist FW, Kay LE (2001) Measurement of slow (μ s-ms) time scale dynamics in protein side chains by N-15 relaxation dispersion NMR spectroscopy: application to Asn and Gln residues in a cavity mutant of T4 lysozyme. *J Am Chem Soc* 123:967–975
- Palmer AG (2004) NMR characterization of the dynamics of biomacromolecules. *Chem Rev* 104:3623–3640
- Palmer AG 3rd, Koss H (2019) Chemical exchange. *Methods Enzymol* 615:177–236. <https://doi.org/10.1016/bs.mie.2018.09.028>
- Palmer AG, Cavanagh J, Wright PE, Rance M (1991) Sensitivity improvement in proton-detected 2-dimensional heteronuclear correlation Nmr-spectroscopy. *J Magn Reson* 93:151–170. [https://doi.org/10.1016/0022-2364\(91\)90036-S](https://doi.org/10.1016/0022-2364(91)90036-S)

- Press WH, Teukolsky SA, Vetterling WT, Flannery BP (2002) Numerical recipes in C++ : the art of scientific computing, 2nd edn. Cambridge University Press, Cambridge
- Raum HN, Dreydoppel M, Weininger U (2018) Conformational exchange of aromatic side chains by (1)H CPMG relaxation dispersion. *J Biomol NMR* 72:105–114. <https://doi.org/10.1007/s10858-018-0210-5>
- Raum HN, Schorghuber J, Dreydoppel M, Lichtenecker RJ, Weininger U (2019) Site-selective (1)H/(2)H labeling enables artifact-free (1)H CPMG relaxation dispersion experiments in aromatic side chains. *J Biomol NMR* 73:633–639. <https://doi.org/10.1007/s10858-019-00275-z>
- Schörghuber J et al (2018) Late metabolic precursors for selective aromatic residue labeling. *J Biomol NMR* 71:129–140. <https://doi.org/10.1007/s10858-018-0188-z>
- Steiner E, Schlagnitweit J, Lundström P, Petzold K (2016) Capturing excited states in the fast-intermediate exchange limit in biological systems using (HNMR)-H-1 spectroscopy. *Angew Chem Int Edit* 55:15869–15872. <https://doi.org/10.1002/anie.201609102>
- Teilum K, Brath U, Lundström P, Akke M (2006) Biosynthetic C-13 labeling of aromatic side chains in proteins for NMR relaxation measurements. *J Am Chem Soc* 128:2506–2507
- Vallurupalli P, Bouvignies G, Kay LE (2012) Studying “Invisible” excited protein states in slow exchange with a major state conformation. *J Am Chem Soc* 134:8148–8161. <https://doi.org/10.1021/ja3001419>
- Vallurupalli P, Hansen DF, Stollar E, Meirovitch E, Kay LE (2007) Measurement of bond vector orientations in invisible excited states of proteins. *Proc Natl Acad Sci USA* 104:18473–18477
- Vallurupalli P, Sekhar A, Yuwen TR, Kay LE (2017) Probing conformational dynamics in biomolecules via chemical exchange saturation transfer: a primer. *J Biomol NMR* 67:243–271. <https://doi.org/10.1007/s10858-017-0099-4>
- van de Ven FJM (1995) Multidimensional NMR in liquids: basic principles and experimental methods. Wiley, New York
- Wagner G (1980) Activation volumes for the rotational motion of interior aromatic rings in globular-proteins determined by high-resolution H-1-Nmr at variable pressure. *FEBS Lett* 112:280–284
- Wagner G, Demarco A, Wüthrich K (1976) Dynamics of aromatic amino-acid residues in globular conformation of basic pancreatic trypsin-inhibitor (Bpti) 1 H-1 Nmr-studies. *Biophys Struct Mech* 2:139–158
- Weininger U et al (2013) Protein conformational exchange measured by H-1 R-1 rho relaxation dispersion of methyl groups. *J Biomol NMR* 57:47–55
- Weininger U (2019) Optimal isotope labeling of aromatic amino acid side chains for NMR studies of protein dynamics. *Methods Enzymol* 614:67–86. <https://doi.org/10.1016/bs.mie.2018.08.028>
- Weininger U, Diehl C, Akke M (2012a) C-13 relaxation experiments for aromatic side chains employing longitudinal- and transverse-relaxation optimized NMR spectroscopy. *J Biomol NMR* 53:181–190
- Weininger U, Respondek M, Akke M (2012b) Conformational exchange of aromatic side chains characterized by L-optimized TROSY-selected C-13 CPMG relaxation dispersion. *J Biomol NMR* 54:9–14
- Weininger U, Respondek M, Löw C, Akke M (2013) Slow aromatic ring flips detected despite near-degenerate NMR frequencies of the exchanging nuclei. *J Phys Chem B* 117:9241–9247
- Weininger U, Brath U, Modig K, Teilum K, Akke M (2014a) Off-resonance rotating-frame relaxation dispersion experiment for C-13 in aromatic side chains using L-optimized TROSY-selection. *J Biomol NMR* 59:23–29
- Weininger U, Modig K, Akke M (2014b) Ring flips revisited: C-13 relaxation dispersion measurements of aromatic side chain dynamics and activation barriers in basic pancreatic trypsin inhibitor. *Biochemistry* 53:4519–4525
- Weininger U, Modig K, Geitner AJ, Schmidpeter PAM, Koch JR, Akke M (2017) Dynamics of aromatic side chains in the active site of FKBP12. *Biochemistry* 56:334–343. <https://doi.org/10.1021/acs.biochem.6b01157>

Publisher's Note Springer Nature remains neutral with regard to jurisdictional claims in published maps and institutional affiliations.

Paper III



Transition-State Compressibility and Activation Volume of Transient Protein Conformational Fluctuations

Matthias Dreydoppel, Britta Dorn, Kristofer Modig, Mikael Akke, and Ulrich Weininger*



Cite This: *JACS Au* 2021, 1, 833–842



Read Online

ACCESS |



Metrics & More



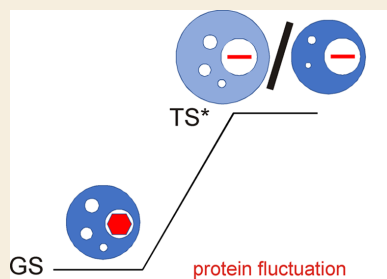
Article Recommendations



Supporting Information

ABSTRACT: Proteins are dynamic entities that intermittently depart from their ground-state structures and undergo conformational transitions as a critical part of their functions. Central to understanding such transitions are the structural rearrangements along the connecting pathway, where the transition state plays a special role. Using NMR relaxation at variable temperature and pressure to measure aromatic ring flips inside a protein core, we obtain information on the structure and thermodynamics of the transition state. We show that the isothermal compressibility coefficient of the transition state is similar to that of short-chain hydrocarbon liquids, implying extensive local unfolding of the protein. Our results further indicate that the required local volume expansions of the protein can occur not only with a net positive activation volume of the protein, as expected from previous studies, but also with zero activation volume by compaction of remote void volume, when averaged over the ensemble of states.

KEYWORDS: protein dynamics, protein volume fluctuations, NMR spectroscopy, relaxation dispersion, high-pressure NMR



INTRODUCTION

Protein motions are essential for biological function. Functionally important protein dynamics often involve rare transitions between alternative conformations that require collective movement of many atoms, taking place on relatively slow time scales, on the order of microseconds to milliseconds. Over the last couple of decades, development of NMR relaxation dispersion methods has enabled in-depth studies of conformational exchange dynamics, highlighting the critical role of lowly populated, high-energy conformations for protein function.^{1–3} While these studies have made it possible to characterize the properties of high-energy states, much less is known about the transition states of the free-energy barriers between the ground and high-energy states. Understanding the protein motions that enable conformational changes requires characterization of the transition states to assess the extent of structural and energetic perturbation of the protein as it passes the free energy barrier between basins in the energy landscape.

Aromatic ring flips, i.e., 180° jumps around the χ_2 dihedral angle (or the imaginary $C_\beta-C_\gamma-C_\gamma$ -axis) in phenylalanine and tyrosine residues, represent a hallmark of protein dynamics⁴ first revealed by seminal studies in the mid-1970s that fundamentally changed the view of proteins by demonstrating their highly dynamic character.^{5–7} The apparently simple reaction coordinate of ring flips—in the case of phenylalanine, the two end states have an identical conformation—makes for an attractive system to investigate the nature of the transition-state ensemble and its thermodynamic properties. The

activation enthalpy and activation entropy of ring flips have been characterized by temperature-dependent NMR experiments for only a handful of proteins.^{5,7–13} Indeed, despite the long history of studying ring flips, there are not many proteins for which ring flip rates have been measured experimentally.^{5–18} In fact, experimental characterization of ring flip rates did not progress much after the groundbreaking observations in the 1970s, partly because of limitations of the NMR technique, which required well-resolved signals in the slow-exchange regime. Recently, there has been a renaissance in these types of studies,^{11,13,19,20} enabled by methodological advances, including site-selective isotope labeling of aromatic side chains,^{21–27} relaxation dispersion experiments tailored to aromatic rings,^{28–31} and improved analysis that takes into account the effects of strong $^1\text{H}-^1\text{H}$ J -coupling within the aromatic ring.¹⁶

The densely packed interior of globular proteins implies that ring flips can occur only upon the formation of substantial void volume around the ring. Thus, it is of significant interest to characterize such activation volumes with the aim to obtain key information about the conformational fluctuations of the local

Received: February 12, 2021

Published: June 3, 2021



ring environment. Activation volumes of ring flips can be determined from pressure-dependent NMR experiments, which have been performed on a small number of proteins.^{8,13,14,32} Applying high hydrostatic pressure is an elegant means to shift the equilibrium between different states, often in a fully reversible way.^{33–37} Pressure-dependent studies yield access to additional thermodynamic parameters, including the difference between states in their partial molar volumes and isothermal compressibilities. Furthermore, by varying both pressure and temperature, it is possible to determine the pressure–temperature phase diagram of a process (Figure 1)

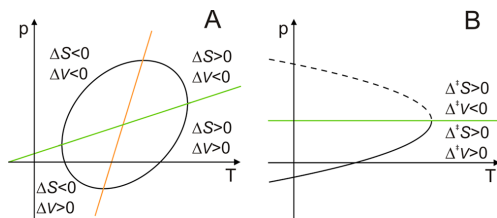


Figure 1. Schematic representation of pressure–temperature phase diagrams $\Delta G(p,T)$ for a protein. (A) Protein stability. Different regions for ΔV and ΔS are indicated. Lines indicating $\Delta V = 0$ and $\Delta S = 0$ are shown in green and orange, respectively. The same principles hold for equilibrium and kinetic diagrams. (B) Schematic representation of a phase diagram $\Delta^\ddagger G(p,T)$ for a ring flip process, as addressed in the text. The green line $\Delta^\ddagger V = 0$ divides the pressure–temperature surface into regions of $\Delta^\ddagger V > 0$ (full line) and $\Delta^\ddagger V < 0$ (dashed line). Distinctions between the phase diagrams in (A) and (B) originate from the different numbers of temperature-dependent parameters, which determine the shape of the contour lines.

and probe the thermal expansion and heat capacity.³⁴ Most pressure-dependent studies on proteins have addressed folding–unfolding equilibria,^{34,38–40} where the effects are large and can be studied efficiently by low-resolution methods (e.g., fluorescence, UV, or CD spectroscopy). High-pressure NMR spectroscopy offers significant advantages, including a high-resolution view of protein structure and dynamics.^{33,41–47} NMR studies have revealed the effect of pressure on the native-state protein structure^{14,48,49} and its hydrogen bond network^{44,46} as well as on protein-folding kinetics^{42,50–54} and the pressure–temperature phase diagram of protein folding.³⁸

Here, we employ pressure- and temperature-dependent NMR relaxation dispersion experiments to determine the activation enthalpy ($\Delta^\ddagger H_0$), entropy ($\Delta^\ddagger S_0$), volume ($\Delta^\ddagger V_0$), and isothermal volume compressibility ($\Delta^\ddagger \kappa'$) of aromatic ring flips for F52 in the B1 domain of protein G (GB1); see **Materials and Methods** for a description of the underlying theory. Together, these thermodynamic parameters provide unique information on the structural and energetic properties of the transition state. The four parameters paint a consistent picture of the transition state as being expanded with a concomitant loss of favorable interactions, an increase in the number of populated conformations, and a compressibility considerably greater than that of the ground state. The results further indicate that ring flips can occur via two complementary mechanisms that involve either a positive activation volume, as previously observed, or positive volume fluctuations that, on average, are compensated by compaction of remote void volumes to yield a net zero activation volume. Taken

together, these observations reveal that the local density of the protein core is considerably perturbed by frequent fluctuations.

RESULTS AND DISCUSSION

We focused in this study on the aromatic ring of F52 in protein GB1, which gives rise to high-quality $R_{1\rho}$ relaxation dispersion profiles over a wide range of temperature and pressure. Several factors restrict the ranges of temperature and pressure over which ring flips can be studied in aqueous solution, including the obvious limitations imposed by the freezing and boiling points of water. Second, most proteins have limited thermal stability and often start to unfold even below 50 °C and ambient pressure. Third, the sensitivity of NMR experiments designed to study exchange processes depends critically on various system parameters that in turn depend on temperature and pressure, such as the kinetic rate constants in relation to the chemical shift difference between the exchanging states. However, F52 has a sizable ^{13}C chemical shift difference ($\Delta\delta$) between the two ϵ -positions of the ring, which we measured under slow-exchange conditions,¹³ leading to significant relaxation dispersion also at higher flip rates. For this residue, the counteracting effects of increasing pressure (which decreases the flip rate) and increasing temperature (which increases the flip rate) serve to keep the flip rate within the NMR-observable window under conditions where the protein is fully folded. This is in contrast to the other aromatic rings in GB1, which yield suitable $R_{1\rho}$ relaxation data only at higher temperatures and ambient pressure and therefore cannot be characterized at higher pressures, because the required raise in temperature leads to the onset of unfolding. The aromatic ring of F52 is occluded in the protein core, where it is surrounded by the side chains of Y3, F30, W43, and Y45 (Figure 2). We

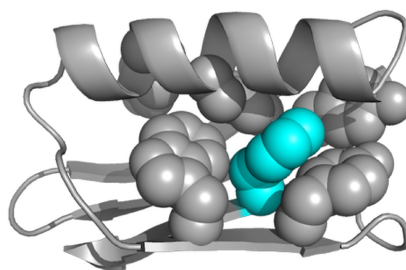


Figure 2. Protein GB1 structure overview. The backbone is shown in ribbon representation, and aromatic side chains are shown as space-filling spheres. F52 is colored cyan. PDB entity 1pgb.⁶⁵

used GB1 samples site-specifically ^{13}C -labeled using 2- ^{13}C glucose, which results in 20% ^{13}C incorporation at the ϵ -positions of Tyr and Phe.²⁴ This labeling scheme is sufficient for small- to medium-sized proteins that can be investigated at concentrations of 1 mM or higher. Higher ^{13}C incorporation levels can be achieved using chemically synthesized precursors that are metabolically closer to the product, e.g., 99% ^{13}C incorporation has been reported for the ϵ -position in Phe,²³ such labeling schemes also enable site-specific deuterium, which might be beneficial for larger proteins.^{21,23} However, the present level of ^{13}C incorporation can be used advantageously in combination with the transverse relaxation-optimized spectroscopy (TROSY)-selected $R_{1\rho}$ relaxation dispersion

Table 1. Ring Flip Rates for F52 at Different Pressures and Temperatures^a

p (MPa)	k_{flip} (10^3 s^{-1})						
	10 °C	15 °C	20 °C	25 °C	30 °C	35 °C	40 °C
0.1	8.5 ± 0.8	10.2 ± 0.7	14.2 ± 0.7				
50	4.6 ± 0.6	7.5 ± 0.6	9.5 ± 0.5	13.1 ± 0.5			
100			7.7 ± 0.5	9.8 ± 0.5	13.6 ± 0.5		
150			4.7 ± 0.5	8.3 ± 0.5	11.5 ± 0.4	18.8 ± 0.7	
200				7.0 ± 0.9	9.9 ± 0.7	15.0 ± 0.8	21.7 ± 1.3

^aDerived with the restriction $k_{\text{flip}}(T_{\text{high}}) > k_{\text{flip}}(T_{\text{low}})$, $R_{2,0}(T_{\text{high}}) \leq R_{2,0}(T_{\text{low}})$.

experiment, which leads to a significant reduction of the inherent transverse relaxation rates ($R_{2,0}$) and therefore dramatically increased sensitivity to conformational exchange.^{28,29} We acquired 18 ^{13}C $R_{1\rho}$ relaxation dispersion curves of sufficient quality at temperatures between 10–40 °C and pressures between 0.1–200 MPa (Figure S1). We determined the ring flip rates, k_{flip} , by global fitting of the dispersion data across all temperatures at a given pressure, with the restrictions $k_{\text{flip}}(T_{\text{high}}) > k_{\text{flip}}(T_{\text{low}})$ and $R_{2,0}(T_{\text{high}}) \leq R_{2,0}(T_{\text{low}})$, yielding the results summarized in Table 1. The values of k_{flip} determined here are on the order of 10^4 s^{-1} , which is at the higher end of previously measured flip rates (10^1 – 10^5 s^{-1})^{7–9,11,12} but a factor of 10^5 slower than those inferred for surface-exposed aromatic rings in ubiquitin via their effect on ^{13}C order parameters.⁵⁵ The wide range of flip rates reflects the strong dependence of the ring dynamics on the packing density and stability of the local protein environment.

Activation Enthalpy, Entropy, and Volume from Separate Temperature- or Pressure-Dependent Analyses

We analyzed 18 flip rates obtained at 5 different pressures (0.1–200 MPa) by performing nonlinear fits using the Eyring equation, eq 8, to derive five different pressure-dependent activation enthalpies that vary between $(51 \pm 2) \text{ kJ mol}^{-1}$ and $(54 \pm 2) \text{ kJ mol}^{-1}$ and a single, global activation entropy of $(11 \pm 7) \text{ J mol}^{-1} \text{ K}^{-1}$ (Figure 3); the activation entropy is pressure-independent as a consequence of assuming that the isobaric volume expansivity is negligible, $\Delta^{\ddagger}\alpha' = 0$; see eq 3. The

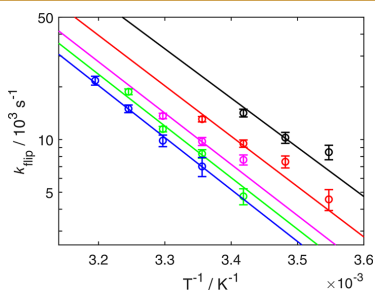


Figure 3. Temperature-dependence of flip rates. k_{flip} is plotted as a function of $1/T$ at different pressures: 0.1 MPa (black), 50 MPa (red), 100 MPa (magenta), 150 MPa (green), and 200 MPa (blue). The fits of eq 8 to the data are displayed as solid lines. The data are represented using a logarithmic y -axis to show the expected linearity, but the fit was performed using nonlinear regression of k_{flip} on T . Data were fitted globally to a common activation entropy ($\Delta^{\ddagger}S$) and different apparent activation enthalpies ($\Delta^{\ddagger}H$) at the different pressures.

narrow temperature range accessible in these experiments limits the precision in $\Delta^{\ddagger}S$. The pressure-dependent increase in activation enthalpy is small, in agreement with the only previous study addressing this issue,⁸ and the derived activation entropy is positive in agreement with all previous experimental studies of ring flip rates.^{5,7–13} The activation free energy is very similar to the value determined in our previous study based solely on temperature-dependent measurements, whereas both $\Delta^{\ddagger}H$ and $\Delta^{\ddagger}S$ are lower than the previous estimates,¹³ emphasizing the difficulties of deconvoluting the two parameters in that case. However, these differences have no impact on the present study, which is self-consistent. The very limited variation in $\Delta^{\ddagger}H$ indicates that this parameter can be considered temperature- and pressure-independent.

Next, we fitted eight flip rates measured at three temperatures (10, 15, and 20 °C) against pressure according to eq 9 to derive a global activation volume of $(17 \pm 2) \text{ mL mol}^{-1}$ (Figure 4), which is somewhat smaller than that measured in

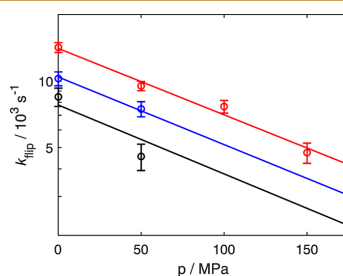


Figure 4. Pressure-dependence of ring flip rates. k_{flip} is plotted as a function of pressure at different temperatures: 10 °C (black), 15 °C (blue), and 20 °C (red). The fits of eq 9 to the data are displayed as solid lines. The data are represented using a logarithmic y -axis to show the expected linearity, but the fit was performed using nonlinear regression of k_{flip} on p .

our previous study.¹³ In agreement with all previous experimental studies, the activation volume is positive.^{8,13,14,32} The positive values of both $\Delta^{\ddagger}S$ and $\Delta^{\ddagger}V$ are consistent with the expectation that the transition-state ensemble is more expanded with a greater number of conformations than the ground state, which is densely packed and conformationally restricted. Note that in the present context, the “transition state” refers specifically to the activation barrier of the ring flip process.

The pressure-dependence of the flip rate directly shows that it decreases progressively with increasing pressure (Figure 3). That is, the fitted lines, describing the flip rate as a function of temperature, approach each other as pressure increases. Furthermore, determination of the activation volume using

only rates measured at higher pressure results in a smaller activation volume. Therefore, it is clear that the activation volume alone cannot account for the observed pressure-dependence, demonstrating the requirement to include the isothermal volume compressibility κ' in the model, which amounts to introducing a second-order pressure-dependence of the activation free energy; see eq 6.

Pressure–Temperature Phase Diagram of the F52 Ring Flip

We performed a global fit of eq 6 to all derived ring flip rates, so as to determine the Gibbs free energy ($\Delta^\ddagger G_0$), activation entropy ($\Delta^\ddagger S_0$), and activation volume ($\Delta^\ddagger V_0$) at the reference point as well as the volume compressibility of activation ($\Delta^\ddagger \kappa'$) (Figure S2A). The reference point (p_0, T_0) was set to atmospheric pressure (0.1 MPa) and 20 °C. By comparison, a global fit without the compressibility factor included describes the experimental data visibly worse (Figure S2B). Inclusion of $\Delta^\ddagger \kappa'$ reduces χ^2_{red} (i.e., χ^2 normalized by the number of degrees of freedom) from 4.4 to 2.0, which is significant as gauged by *F*-tests based on Monte Carlo simulations. The probability that inclusion of $\Delta^\ddagger \kappa'$ would reduce χ^2 as much as observed even if it is not the correct model (overfitting; type I error) is $p_I < 0.001$. The probability that the model including $\Delta^\ddagger \kappa'$ does not reduce χ^2 as much as observed when it is the correct model (type II error) is $p_{II} \approx 0.07$. In other words, the probability is low that a fit without $\Delta^\ddagger \kappa'$ would describe the data as well as actually observed.

The global fit resulted in $\Delta^\ddagger \kappa' = (0.13 \pm 0.02)$ mL mol⁻¹ MPa⁻¹, which we analyze in detail below. Further, $\Delta^\ddagger G_0 = (48.2 \pm 0.1)$ kJ mol⁻¹ and $\Delta^\ddagger S_0 = (17 \pm 7)$ J mol⁻¹ K⁻¹ (Table 2), both corresponding well with the values obtained when

Table 2. Thermodynamic Parameters of F52 Ring Flipping^a

data	$\Delta^\ddagger G_0$ (kJ mol ⁻¹)	$\Delta^\ddagger S_0$ (J mol ⁻¹ K ⁻¹)	$\Delta^\ddagger V_0$ (mL mol ⁻¹)	$\Delta^\ddagger \kappa'$ (mL mol ⁻¹ MPa ⁻¹)
k_{flip}^b	48.2 ± 0.1	17 ± 7	28 ± 2	0.13 ± 0.02
$R_{1,p}^c$	48.4 ± 0.1	5 ± 5	24 ± 2	0.11 ± 0.02

^aGlobal fitting using eq 6. The reference point (p_0, T_0) = (0.1 MPa, 20 °C). ^bGlobal fit of flip rates determined separately at each *p* and *T*. ^cDirect, global fit of $R_{1,p}$ relaxation dispersion data.

including only the temperature-dependence. The activation volume was determined to $\Delta^\ddagger V_0 = (28 \pm 2)$ mL mol⁻¹ = (46 ± 3) Å³, which is substantially larger than the value obtained when considering only the pressure-dependence, (17 ± 2) mL mol⁻¹ (Figure 4); the apparent discrepancy arises because the higher-order model deconvolutes the activation volume from the volume compressibility. However, the result is in fair agreement with our previous study on GB1¹³ and activation volumes obtained for other systems, which range from 27 to 51 mL mol⁻¹.^{8,13,14,32} $\Delta^\ddagger V_0$ can be compared to the volume available to the F52 ring in the ground state, which is 125 Å³ (see below). Notably, the sum of the ground-state volume and activation volume ($125 + 46 = 171$ Å³) matches well with the volume of the sphere swept out by a rotating aromatic ring, 164 Å³.³²

The pressure–temperature phase diagram calculated from these values is shown in Figure 5A. It displays a parabolic shape for the contours of constant $\Delta^\ddagger G$, with lower $\Delta^\ddagger G$ values at higher temperatures, according to the positive sign of $\Delta^\ddagger S_0$, which indicates an increase in the number of populated conformations of the transition-state ensemble compared to

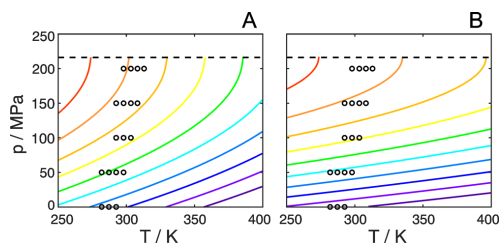


Figure 5. Experimental pressure–temperature phase diagram of the F52 ring flip. Calculated from the thermodynamic parameters obtained by (A) global fitting of flip rates shown in Table 1 and (B) direct global fitting of $R_{1,p}$ relaxation dispersions. Colored lines indicate contours of constant values for the Gibbs free energy of activation, $\Delta^\ddagger G$, ranging equidistantly (A) from 47.0 kJ mol⁻¹ (violet) to 51.5 kJ mol⁻¹ (red) and (B) from 48.3 kJ mol⁻¹ (violet) to 51.0 kJ mol⁻¹ (red). Measured data points are shown as black circles, and $\Delta^\ddagger V = 0$ is indicated as a dashed line.

the ground state. The experimentally measured activation free energies are located in the region where $\Delta^\ddagger V > 0$, with data points obtained at higher pressures approaching the line $\Delta^\ddagger V = 0$, which occurs at about 215 MPa.

After having established the model for deriving the pressure–temperature phase diagram of the F52 ring flip (including the volume compressibility of activation $\Delta^\ddagger \kappa'$), we performed a global fit of all $R_{1,p}$ relaxation dispersion profiles directly to the model described by eq 6 in order to possibly minimize uncertainties in the fitted activation parameters (Figure S1, red lines). As a consequence of this approach, all derived flip rates now fall directly on the curves describing the model; see the dependence of k_{flip} on T^{-1} (Figure S2C). The new global fit resulted in $\Delta^\ddagger G_0 = (48.4 \pm 0.1)$ kJ mol⁻¹, $\Delta^\ddagger S_0 = (5 \pm 5)$ J mol⁻¹ K⁻¹, $\Delta^\ddagger V_0 = (24 \pm 2)$ mL mol⁻¹, and $\Delta^\ddagger \kappa' = (0.11 \pm 0.02)$ mL mol⁻¹ MPa⁻¹ (Table 2). All values are identical within the margin of error to those determined by the alternative approach described above. Moreover, the estimated errors in the parameters are also highly similar between the two approaches. The largest difference is observed for the activation entropy, where the direct fit to the $R_{1,p}$ data results in a lower value. As before, $\Delta^\ddagger S_0$ is not well-determined due to the limited temperature range of our experiments. Nevertheless, $\Delta^\ddagger S_0$ is positive in both approaches, as expected from theoretical considerations (see above). The extrapolated value of $\Delta^\ddagger V = 0$ now occurs at 218 MPa, which is virtually identical to the pressure reported above (215 MPa). The *p*–*T* phase diagram resulting from the direct fit to the $R_{1,p}$ data is shown in Figure 5B. The lower value of $\Delta^\ddagger S_0$ leads to a less pronounced temperature-dependence compared to Figure 5A, but the main features of the two diagrams are highly similar. In summary, we conclude that the two fitting approaches work equally well and result in very similar activation parameters. In the following, we base our analysis on the parameters corresponding to Figure 5A but provide the values derived from the alternative fit within parentheses where appropriate.

Ring Flips Can Occur without a Net Positive Activation Volume

At 20 °C and ambient pressure, the F52 ring flips occur via an expanded transition state characterized by a volume increase of $\Delta^\ddagger V_0 = 46$ Å³ (or 40 Å³ from the direct fit to the $R_{1,p}$ data). Nonetheless, ring flips still take place at higher pressures

approaching the region where $\Delta^\ddagger V = 0$ and $\Delta^\ddagger G$ is insensitive to pressure (i.e., the tangent of the contour line is vertical), as shown in Figure 5. Pressure-independent volume fluctuations that do not lead to a net average expansion of the local ring environment enable $k_{\text{flip}} = 6.9 \times 10^3 \text{ s}^{-1}$, obtained by extrapolation to 25 °C and 215 MPa, where $\Delta^\ddagger V = 0$. This value can be compared to the slowest measured flip rate, $k_{\text{flip}} = (7.0 \pm 0.3) \times 10^3 \text{ s}^{-1}$, obtained at 25 °C and 200 MPa (Table 1). It is important to note that $\Delta^\ddagger V$ describes the ensemble-averaged difference between the ground and transition states. When $\Delta^\ddagger V = 0$, the ring flip does not involve a net average expansion of the protein core. Instead, the required void volume around the ring is created by volume fluctuations that, on average across the ensemble, are compensated by compaction of void volumes. These fluctuations are described by the protein compressibility; see eq 7. The root-mean-square volume fluctuations of the GB1 ground state have been estimated to 0.75% of the total protein volume, or 60 \AA^3 ,⁵⁶ indicating that ring flips can be accommodated by fluctuations at the tail end (>1 standard deviation) of the volume probability distribution. Interestingly, this type of behavior has been predicted from microsecond-long molecular dynamics simulations, where dynamic volume fluctuations lead to “cavity migrations” through the protein core.⁵⁷

Fluctuations that do lead to a net expansion ($\Delta^\ddagger V > 0$) occur at pressures lower than 215 MPa, allowing for increasingly frequent ring flips as $\Delta^\ddagger V$ increases with decreasing pressure; for reference, extrapolated to 25 °C and ambient pressure, the F52 ring undergoes 23×10^3 flips per second. The result that ring flips can occur without a net activation volume explains in part why ring flips in different proteins appear to show varying activation volumes. In this view, the activation volume does not report on the minimal expansion required for a ring flip to occur but rather on the average net volume increase that leads to a ring flip under given conditions. The present results demonstrate that significant fluctuations in the local packing density persist even at quite high pressure, thus underscoring the highly dynamic nature of proteins. The difference in volume compressibility between the ground state and the transition state, $\Delta^\ddagger \kappa'$, is positive, demonstrating that the transition-state ensemble is more compressible and undergoes greater volume fluctuations than the well-packed ground state. Figure 6 summarizes these results in a schematic fashion.

Protein Component Compressibility of the Transition State

The compressibility of a protein state depends on its intrinsic packing and hydration properties.⁵⁸ The protein compressibility includes contributions from protein–solvent cross-correlated volume fluctuations that appear to contribute as much as the protein autocorrelated fluctuations.^{56,59} By measuring the pressure-dependence of ring flips, we are in principle monitoring not only the volume fluctuations and activation volume of the local environment of the aromatic ring but also cross-correlations with other regions outside of its immediate surroundings, which include the solvent shell. However, the present work does not resolve these different contributions to the compressibility, and it is likely that our results primarily report on the surroundings of the aromatic ring.

The value of the volume compressibility change upon activation determined herein, $\Delta^\ddagger \kappa' = (130 \pm 20) \text{ mL mol}^{-1}$

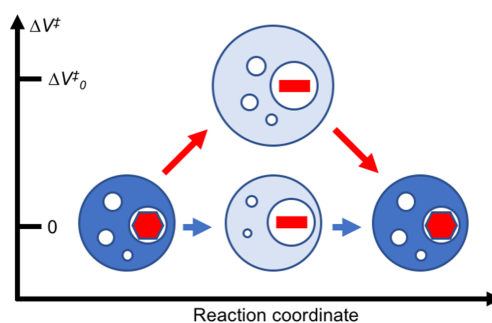


Figure 6. Schematic illustration of aromatic ring flips. The two identical ground states are represented by dark blue spheres with void volumes shown as white spheres and the aromatic rings shown as red hexagons. The transition state is represented by a light blue sphere with the red line representing the aromatic ring in an orientation orthogonal to that of the ground state. The hue of the blue sphere indicates the compressibility, with light and dark blue representing higher and lower compressibility, respectively. At very high pressures (lower pathway, blue arrows), ring flips can occur without a net activation volume ($\Delta^\ddagger V = 0$) but with an increase in compressibility of the transition state compared to the ground state ($\Delta^\ddagger \kappa' > \kappa$). At lower pressures (upper pathway, red arrows), ring flips occur with a combination of positive activation volume ($\Delta^\ddagger V > 0$) and increased compressibility. The relative size of the circles provides a qualitative illustration of volume changes. The representation is valid only for the ensemble-averaged properties of the ground and transition states.

GPa^{-1} (or $110 \text{ mL mol}^{-1} \text{ GPa}^{-1}$), is on the order of the changes associated with unfolding of globular proteins,^{35,58,60,61} which might suggest that the compressibility of the transition state is similar to that of the unfolded state. However, this interpretation is highly tentative, because $\Delta^\ddagger \kappa' = \Delta^\ddagger(\kappa V)$, and the changes in volume might differ considerably between the ring flip and unfolding processes. To estimate the isothermal compressibility coefficient of the transition state, $\Delta^\ddagger \kappa = \kappa + \Delta^\ddagger \kappa'$, we first expand the volume compressibility by differentiation: $\Delta^\ddagger \kappa' \approx \kappa \Delta^\ddagger V_0 + V_0 \Delta^\ddagger \kappa$. Next, we use the experimentally measured values of $\Delta^\ddagger \kappa'$ and $\Delta^\ddagger V_0$ (reported above) together with calculated values for κ and V_0 (see below). The ratio $\Delta^\ddagger \kappa' / \Delta^\ddagger V_0 = 4.7 \pm 0.8 \text{ GPa}^{-1} \approx \kappa + V_0 \Delta^\ddagger \kappa / \Delta^\ddagger V_0 \kappa$. This value is about 20 times greater than the value, $\kappa = 0.24 \text{ GPa}^{-1}$, determined for GB1 by molecular dynamics simulations,⁵⁶ indicating that the term $V_0 \Delta^\ddagger \kappa / \Delta^\ddagger V_0$ is most likely not negligible. To continue, using the values for κ and $\Delta^\ddagger V_0$, we obtain $V_0 \Delta^\ddagger \kappa \approx \Delta^\ddagger \kappa' - \kappa \Delta^\ddagger V_0 = 124 \text{ mL mol}^{-1} \text{ GPa}^{-1}$ (or $104 \text{ mL mol}^{-1} \text{ GPa}^{-1}$). We take V_0 to be the volume available to the phenyl ring of F52 in the ground state, represented by the crystal structure 1pgb.⁶² Using additively weighted Voronoi tessellation as implemented in Voronota,⁶³ we calculate $V_0 = 125 \text{ \AA}^3 = 76 \text{ mL/mol}$. For comparison, this value is on par with volumes previously calculated for aromatic rings in the interior of globular proteins^{64,65} but greater than the volume of the van der Waals envelope of a phenyl ring (75 \AA^3) and less than the volume swept out by the rotating ring ($164 \text{ \AA}^3 = 100 \text{ mL/mol}$).^{8,13,14,32} Using $V_0 = 125 \text{ \AA}^3$, we obtain $\Delta^\ddagger \kappa = 1.6 \text{ GPa}^{-1}$ (or 1.4 GPa^{-1}) and thus a transition-state compressibility, $\Delta^\ddagger \kappa = 1.8 \text{ GPa}^{-1}$ (or 1.6 GPa^{-1}). Notably, this value is similar to the compressibility of organic liquids, e.g., short-chain alkanes at 25 °C.⁶⁶ Thus, the transition-state ensemble exhibits liquid-like volume fluctuations, a character-

istic that has also been inferred for unfolded states,⁵⁸ indicating that the conformational rearrangements that enable ring flips involve significant unfolding of the local structure through transient “breathing motions” of the protein. We note that very rapid ring flips of the aromatic residues in ubiquitin have been interpreted to suggest liquid-alkane-like properties of the surrounding environment in the ground state.⁵⁵ Given the high degree of solvent exposure of the aromatic residues in ubiquitin, it might be expected that their local environment is similar to unfolded states. Taken together, the previous and present results show that aromatic ring flip rates can vary drastically depending on the local packing density. Aromatic rings in the interior of globular proteins might require extensive disruption of the local structure in order to flip, whereas surface-exposed rings can undergo large-scale librational motions and flip rapidly.

CONCLUSIONS

We have demonstrated that temperature- and pressure-dependent NMR relaxation dispersion experiments provide unique thermodynamic information on the transition state of rare conformational transitions, such as aromatic ring flips. We determined the activation enthalpy ($\Delta^\ddagger H_0$), entropy ($\Delta^\ddagger S_0$), volume ($\Delta^\ddagger V_0$), and isothermal volume compressibility ($\Delta^\ddagger \kappa'$) of aromatic ring flips, which report on the structural and energetic perturbations of the transition state. It is worth noting that our measurements of compressibility are unique in that they report directly on the protein component compressibility of the local ring environment, which should be contrasted with previous experimental measurements that have determined the partial compressibility of the protein solute via concentration-dependent measurements of sound velocity in aqueous solutions.⁵⁸ It is gratifying that all determined thermodynamic parameters present a consistent view of the transition state. Compared to the ground state, the transition state is expanded ($\Delta^\ddagger V_0 > 0$) and has fewer stabilizing interactions ($\Delta^\ddagger H_0 > 0$), populates a greater number of conformations ($\Delta^\ddagger S_0 > 0$), and has significantly greater compressibility ($\Delta^\ddagger \kappa' > 0$). Thus, the aromatic ring flip involves transient “melting” of the surrounding protein structure, which approaches liquid-like features in the transition state.

Our results indicate that ring flips can occur with zero activation volume ($\Delta^\ddagger V = 0$), that is, without any difference between the ground-state and transition-state ensemble averages of protein volume. In this case, the required expansion of the local structure occurs via volume fluctuations that, on average across the ensemble, involve a local increase in volume and compensatory compaction of remote void volume (Figure 6). These volume fluctuations enable a baseline of exchange events, which remain at play even at very high pressure ($p > 200$ MPa). As pressure decreases toward ambient conditions, fluctuations causing net expansion of the protein become increasingly prevalent, leading to more frequent exchange events. Altogether, these results advance our understanding of protein dynamics by detailing the properties of the state and should serve as a benchmark for future computational investigations.

MATERIALS AND METHODS

Protein Samples

The 2-¹³C glucose-labeled B1 domain of Staphylococcal protein G (GB1; UniProtKB P06654) was expressed and purified as described

elsewhere.⁶⁷ 2-¹³C-Glucose labeling results in site-selective ¹³C enrichment at the ϵ -positions of Phe and Tyr residues.^{24,27} The sample was dissolved to a concentration of 5 mM in 20 mM HEPES, 90% H₂O + 10% D₂O, and a small amount of NaN₃. The pH was adjusted to 7.0.

NMR Spectroscopy

All experiments were performed on a Bruker Avance III spectrometer operating at a static magnetic field strength of 14.1 T. Aromatic L-optimized TROSY-selective on-resonance ¹³C $R_{1\rho}$ relaxation dispersion experiments^{28–31} were acquired at temperatures of 10, 15, 20, 25, 30, 35, and 40 °C and pressures of 0.1, 50, 100, 150, and 200 MPa. In short, the pulse sequence consists of the following steps: insensitive nuclei enhanced by polarization transfer (INEPT) from ¹H to ¹³C, followed by the S³E element to select the TROSY component; a relaxation period divided into two blocks separated by the S³CT selective inversion element; ¹³C chemical shift evolution during t_1 ; and magnetization transfer back to ¹H for detection during t_2 . In each relaxation block,¹³C magnetization was aligned along the B_1 field axis by 4 ms tan/tanh adiabatic ramps,⁶⁸ then spin-locked on-resonance using B_1 field strengths of 900–4000 Hz, and finally returned to the original state by a time-reversed adiabatic ramp. For each effective field, two separate experiments were acquired with and without the spin-lock relaxation period, from which relaxation rate constants were calculated as $R_{1\rho} = \ln(I_{\text{relax}}/I_{\text{ref}})/t_{\text{relax}}$ where I_{relax} and I_{ref} are the intensities measured in the spectra acquired with and without the relaxation period, respectively, and t_{relax} is the length of the relaxation period. At a given combination of temperature and pressure, the relaxation dispersion data were acquired as an interleaved pseudo-3D experiment, where the effective field strengths were varied prior to incrementing t_1 .

High-pressure experiments were performed using a commercial 3 mm ceramic cell⁶⁹ (Daedalus Innovations LLC), connected to a home-built pressure generator, consisting of a water column pressurized by a hand pump. The pressurizing water was separated from the protein solution by a thin layer of paraffin oil.

Data Analysis

NMR spectra were processed with NMRPipe⁷⁰ and analyzed with PINT.⁷¹ $R_{1\rho}$ relaxation dispersion data were fitted to the general equation for symmetric exchange derived by Miloushev and Palmer⁷² using fixed populations, $p_1 = p_2 = 0.5$, and treating $\Delta\delta$ as fixed at the value ($\Delta\delta_{\text{spectra}}$) measured from heteronuclear single quantum coherence spectroscopy (HSQC) spectra under slow-exchange conditions.¹³ Chemical shift changes of the observed signal with pressure and temperature are small and linear (Figure S3). The shift difference can be assumed as independent of temperature.^{5,7–13} Data sets acquired at a given pressure and different temperatures were fitted simultaneously while imposing the restrictions $k_{\text{flip}}(T_{\text{high}}) > k_{\text{flip}}(T_{\text{low}})$, $R_{2,0}(T_{\text{high}}) \leq R_{2,0}(T_{\text{low}})$, which are visibly valid at higher temperatures (Figure S1) and required to obtain reliable results under conditions where the ring flip rates reach their highest values. Global fitting of all $R_{1\rho}$ dispersion curves directly to the thermodynamic model (eq 6, see below), involved the restriction $R_{2,0}(T_{\text{high}}) \leq R_{2,0}(T_{\text{low}})$ on data sets acquired at a given pressure.

Theory of Pressure- and Temperature-Dependence of Ring Flip Dynamics

The rate constant depends on the free energy barrier as described by the Eyring equation

$$k_{\text{flip}} = \left(\frac{k_B T}{h} \right) \times \exp \left[- \frac{\Delta^\ddagger G}{RT} \right] \quad (1)$$

in which k_B and h denote Boltzmann's and Planck's constants, respectively, and $\Delta^\ddagger G$ is the Gibbs free energy of activation. To find the overall pressure and temperature dependencies of $\Delta^\ddagger G$, one has to integrate the fundamental equation

$$d\Delta^\ddagger G = -\Delta^\ddagger S dT + \Delta^\ddagger V dp \quad (2)$$

The entropy and volume depend on temperature and pressure according to

$$dS = \frac{C_p}{T} dT - \alpha' dp \quad (3)$$

and

$$dV = \alpha' dT - \kappa' dp \quad (4)$$

where $\alpha' = \alpha V$ is defined here as the isobaric thermal volume expansivity, α is the expansivity coefficient, $\kappa' = \kappa V$ is defined as the isothermal volume compressibility, and κ is the compressibility coefficient.^{56,73} Note that these quantities are not named consistently throughout the literature.

We thus define the volume expansivity of activation as $\Delta^{\ddagger}\alpha' = \Delta^{\ddagger}(\alpha V)$ and the volume compressibility of activation as $\Delta^{\ddagger}\kappa' = \Delta^{\ddagger}(\kappa V)$, with Δ^{\ddagger} denoting the difference between the transition state and the ground state. Note that $\Delta^{\ddagger}\alpha'$ and $\Delta^{\ddagger}\kappa'$ are products of two quantities that might both be different between the two states and therefore do not directly report on the expansivity or compressibility of either state. As an approximation, we differentiate the products into $\Delta^{\ddagger}\kappa' \approx \kappa \Delta^{\ddagger}V + V \Delta^{\ddagger}\kappa$, etc.

eq 2 can be integrated from an arbitrarily chosen reference point (p_0, T_0). Neglecting any pressure-dependence of $\Delta^{\ddagger}S$ or temperature-dependence of $\Delta^{\ddagger}V$, one obtains

$$\begin{aligned} \Delta^{\ddagger}G(p, T) = & \Delta^{\ddagger}G_0 - \Delta^{\ddagger}S_0(T - T_0) - \Delta^{\ddagger}C_p \left[T \left(\ln \left(\frac{T}{T_0} \right) - 1 \right) + T_0 \right] \\ & + \Delta^{\ddagger}\alpha'(T - T_0)(p - p_0) + \Delta^{\ddagger}V_0(p - p_0) - \frac{\Delta^{\ddagger}\kappa'}{2}(p - p_0)^2 \end{aligned} \quad (5)$$

where the subscript 0 indicates the value at (p_0, T_0). The last three terms in eq 5 gives the change in $\Delta^{\ddagger}G(p, T)$ with pressure and are valid only if the changes in $\Delta^{\ddagger}V_0$ with pressure and temperature are small, i.e., if the factors $\Delta^{\ddagger}\alpha'(T - T_0)$ and $\Delta^{\ddagger}\kappa'(p - p_0)$ are small. The resulting phase diagram of $\Delta^{\ddagger}G(p, T)$ displays an elliptic shape and is divided into four regions according to the signs of $\Delta^{\ddagger}S_0$ and $\Delta^{\ddagger}V_0$ (Figure 1A). To continue, we assume that $\Delta^{\ddagger}H$ as well as $\Delta^{\ddagger}S$ are temperature-independent, i.e., $\Delta^{\ddagger}C_p = 0$. We also assume that $\Delta^{\ddagger}V_0$ is temperature-independent, i.e., $\Delta^{\ddagger}\alpha' = 0$, yielding the final expression

$$\Delta^{\ddagger}G(p, T) = \Delta^{\ddagger}G_0 - \Delta^{\ddagger}S_0(T - T_0) + \Delta^{\ddagger}V_0(p - p_0) - \frac{\Delta^{\ddagger}\kappa'}{2}(p - p_0)^2 \quad (6)$$

Thus, the phase diagram describing the free energy barrier of the ring flip has the shape of a parabola (Figure 1B). It is divided into two segments by the $\Delta^{\ddagger}V = 0$ line as its symmetry axis, which can be calculated from the point of maximal temperature and depicts the pressure where the ring flip process is not associated with any increase in void volume. The vertex of the parabola points toward high or low temperatures for a positive or negative sign of $\Delta^{\ddagger}S_0$, respectively. For completeness, κ is related to the magnitude of volume fluctuations as⁷⁴

$$\kappa = -\frac{1}{\langle V \rangle} \left(\frac{\partial \langle V \rangle}{\partial p} \right)_T = \frac{\langle (V - \langle V \rangle)^2 \rangle}{k_B T \langle V \rangle} \quad (7)$$

Initial Analysis of Temperature- and Pressure-Dependence

Activation parameters of the ring flips were initially determined by nonlinear regression of the flip rates on the temperature T using the Eyring equation, parametrized as

$$k_{\text{flip}} = \left(\frac{k_B T}{h} \right) \times \exp \left[-\frac{\Delta^{\ddagger}H - T \Delta^{\ddagger}S}{RT} \right] \quad (8)$$

where $\Delta^{\ddagger}H$ is the activation enthalpy and $\Delta^{\ddagger}S$ is the activation entropy. The activation volume $\Delta^{\ddagger}V$ was determined from the pressure-dependence of the flip rates according to

$$\left(\frac{\partial \ln k_{\text{flip}}}{\partial p} \right) = -\frac{\Delta^{\ddagger}V}{RT} \quad (9)$$

Analysis of p - T Diagram

Activation parameters were determined from global fitting of all flip rate data to eq 1 with $\Delta^{\ddagger}G$ expanded according to eq 6 and the reference point (p_0, T_0) set to atmospheric pressure and 20 °C. Errors in the fitted parameters were estimated using Monte Carlo simulations,⁷⁵ and the reported errors correspond to one standard deviation. The statistical validation for including $\Delta^{\ddagger}\kappa'$ was performed as follows. The experimental $k_{\text{flip}}(p, T)$ data sets were fitted globally in two ways: first with $\Delta^{\ddagger}\kappa'$ fixed to 0 (the lower-order model) and then with $\Delta^{\ddagger}\kappa'$ fitted (the higher-order model). Then ensembles of 1000 $k_{\text{flip}}(p, T)$ data sets were generated from the best fitted parameters for each of the models. Random errors with the experimental standard deviation were added to give the two Monte Carlo ensembles $\{k_{\text{flip}}\}_{\text{low}}$ and $\{k_{\text{flip}}\}_{\text{high}}$. These data ensembles were then fitted to both models, giving four Monte-Carlo-generated sets with reduced χ^2 -values: $\{\chi^2\}_{\text{low}}^{\text{low}}$, $\{\chi^2\}_{\text{low}}^{\text{high}}$, $\{\chi^2\}_{\text{high}}^{\text{low}}$, and $\{\chi^2\}_{\text{high}}^{\text{high}}$, where the lower index is the generating function and the upper is the fitting function. The observed F -static describing the relative size of χ^2 for the two models is $F_{\text{obs}} = \chi^2_{\text{low}} / \chi^2_{\text{high}}$.⁷⁶ To estimate the type I error, $\{F\}_I = \{\chi^2\}_{\text{low}}^{\text{low}} / \{\chi^2\}_{\text{low}}^{\text{high}}$ is calculated. None of these 1000 values were larger than F_{obs} , thus demonstrating a probability $p_I < 10^{-3}$ that F_{obs} is as large as observed by chance if the lower-order model is the correct one. To estimate the type II error, $\{F\}_{II} = \{\chi^2\}_{\text{high}}^{\text{low}} / \{\chi^2\}_{\text{high}}^{\text{high}}$ is calculated. Here, 69 of the 1000 values are smaller than F_{obs} , demonstrating a probability of about $p_{II} = 0.07$ that the higher-order model would not reduce χ^2 as much as observed even if it is the correct one. As an alternative approach, global fitting of eqs 1 and 6 directly to all $R_{1\rho}$ data was performed with error estimation by Monte Carlo simulations as described above.

Volume Calculations

We calculated the volume available to the phenyl ring of F52 in the ground state, represented by the crystal structure of GB1 (PDB entry 1pgb),⁶² using the algorithm for additively weighted Voronoi tessellation implemented in the software Voronota.⁶³

ASSOCIATED CONTENT

Supporting Information

The Supporting Information is available free of charge at <https://pubs.acs.org/doi/10.1021/jacsau.1c00062>.

All experimental ¹³C aromatic $R_{1\rho}$ relaxation dispersion profiles for F52e; temperature- and pressure-dependence of flip rates fitted with and without $\Delta^{\ddagger}\kappa'$ and the corresponding graph resulting from a global fit of $R_{1\rho}$ relaxation dispersion profiles directly to the thermodynamic model; temperature- and pressure-dependence of chemical shifts for the averaged signal of F52e (PDF)

AUTHOR INFORMATION

Corresponding Author

Ulrich Weinger – Institute of Physics, Biophysics, Martin-Luther-University Halle-Wittenberg, D-06120 Halle (Saale), Germany; orcid.org/0000-0003-0841-8332; Phone: +49 345 55 28555; Email: ulrich.weinger@physik.uni-halle.de

Authors

Matthias Dreydoppel – Institute of Physics, Biophysics, Martin-Luther-University Halle-Wittenberg, D-06120 Halle (Saale), Germany

Britta Dorn – Institute of Physics, Biophysics, Martin-Luther-University Halle-Wittenberg, D-06120 Halle (Saale), Germany

Kristofer Modig – Division of Biophysical Chemistry, Center for Molecular Protein Science, Department of Chemistry, Lund University, SE-22100 Lund, Sweden

Mikael Akke – Division of Biophysical Chemistry, Center for Molecular Protein Science, Department of Chemistry, Lund University, SE-22100 Lund, Sweden; orcid.org/0000-0002-2395-825X

Complete contact information is available at:
<https://pubs.acs.org/10.1021/jacsau.1c00062>

Notes

The authors declare no competing financial interest.

ACKNOWLEDGMENTS

This research was supported by the Deutsche Forschungsgemeinschaft (WE 5587/1-1) and the Swedish Research Council (2018-4995).

REFERENCES

- Mittermaier, A. K.; Kay, L. E. Observing biological dynamics at atomic resolution using NMR. *Trends Biochem. Sci.* **2009**, *34* (12), 601–611.
- Boehr, D. D.; McElheny, D.; Dyson, H. J.; Wright, P. E. The dynamic energy landscape of dihydrofolate reductase catalysis. *Science* **2006**, *313* (5793), 1638–1642.
- Eisenmesser, E. Z.; Bosco, D. A.; Akke, M.; Kern, D. Enzyme dynamics during catalysis. *Science* **2002**, *295* (5559), 1520–1523.
- Wüthrich, K. The way to NMR structures of proteins. *Nat. Struct. Biol.* **2001**, *8* (11), 923–925.
- Campbell, I. D.; Dobson, C. M.; Williams, R. J. P. Proton Magnetic-Resonance Studies of Tyrosine Residues of Hen Lysozyme: Assignment and Detection of Conformational Mobility. *Proc. Royal Soc. B* **1975**, *189* (1097), 503–509.
- Hull, W. E.; Sykes, B. D. Fluorotyrosine Alkaline-Phosphatase - Internal Mobility of Individual Tyrosines and Role of Chemical-Shift Anisotropy as a F-19 Nuclear Spin Relaxation Mechanism in Proteins. *J. Mol. Biol.* **1975**, *98* (1), 121–153.
- Wagner, G.; Demarco, A.; Wüthrich, K. Dynamics of Aromatic Amino-Acid Residues in Globular Conformation of Basic Pancreatic Trypsin-Inhibitor (Bpti) 0.1. H-1 Nmr-Studies. *Biophys. Struct. Mech.* **1976**, *2* (2), 139–158.
- Hattori, M.; Li, H.; Yamada, H.; Akasaka, K.; Hengstenberg, W.; Gronwald, W.; Kalbitzer, H. R. Infrequent cavity-forming fluctuations in HPr from *Staphylococcus carnosus* revealed by pressure- and temperature-dependent tyrosine ring flips. *Protein Sci.* **2004**, *13* (12), 3104–3114.
- Nall, B. T.; Zuniga, E. H. Rates and Energetics of Tyrosine Ring Flips in Yeast Iso-2-Cytochrome-C. *Biochemistry* **1990**, *29* (33), 7576–7584.
- Skalicky, J. J.; Mills, J. L.; Sharma, S.; Szyperki, T. Aromatic ring-flipping in supercooled water: Implications for NMR-based structural biology of proteins. *J. Am. Chem. Soc.* **2001**, *123* (3), 388–397.
- Weininger, U.; Modig, K.; Akke, M. Ring Flips Revisited: C-13 Relaxation Dispersion Measurements of Aromatic Side Chain Dynamics and Activation Barriers in Basic Pancreatic Trypsin Inhibitor. *Biochemistry* **2014**, *53* (28), 4519–4525.
- Yang, C. J.; Takeda, M.; Terauchi, T.; Jee, J.; Kainosho, M. Differential Large-Amplitude Breathing Motions in the Interface of FKBP12-Drug Complexes. *Biochemistry* **2015**, *54* (47), 6983–6995.
- Dreydoppel, M.; Raum, H. N.; Weininger, U. Slow ring flips in aromatic cluster of GB1 studied by aromatic C-13 relaxation dispersion methods. *J. Biomol. NMR* **2020**, *74* (2–3), 183–191.
- Li, H.; Yamada, H.; Akasaka, K. Effect of pressure on the tertiary structure and dynamics of folded basic pancreatic trypsin inhibitor. *Biophys. J.* **1999**, *77* (5), 2801–2812.
- Wagner, G.; Bruhwiler, D.; Wüthrich, K. Reinvestigation of the Aromatic Side-Chains in the Basic Pancreatic Trypsin-Inhibitor by Heteronuclear Two-Dimensional Nuclear-Magnetic-Resonance. *J. Mol. Biol.* **1987**, *196* (1), 227–231.
- Weininger, U.; Respondek, M.; Löw, C.; Akke, M. Slow Aromatic Ring Flips Detected Despite Near-Degenerate NMR Frequencies of the Exchanging Nuclei. *J. Phys. Chem. B* **2013**, *117* (31), 9241–9247.
- Baturin, S. J.; Okon, M.; McIntosh, L. P. Structure, dynamics, and ionization equilibria of the tyrosine residues in *Bacillus circulans* xylanase. *J. Biomol. NMR* **2011**, *51* (3), 379–394.
- Rao, D. K.; Bhuyan, A. K. Complexity of aromatic ring-flip motions in proteins: Y97 ring dynamics in cytochrome c observed by cross-relaxation suppressed exchange NMR spectroscopy. *J. Biomol. NMR* **2007**, *39* (3), 187–196.
- Gauto, D. F.; Macek, P.; Barducci, A.; Fraga, H.; Hessel, A.; Terauchi, T.; Gajan, D.; Miyanoiri, Y.; Boisbouvier, J.; Lichtenecker, R.; Kainosho, M.; Schanda, P. Aromatic Ring Dynamics, Thermal Activation, and Transient Conformations of a 468 kDa Enzyme by Specific H-1-C-13 Labeling and Fast Magic-Angle Spinning NMR. *J. Am. Chem. Soc.* **2019**, *141* (28), 11183–11195.
- Sathyamoorthy, B.; Singarapu, K. K.; Garcia, A. E.; Szyperki, T. Protein Conformational Space Populated in Solution Probed with Aromatic Residual Dipolar C-13-H-1 Couplings. *ChemBioChem* **2013**, *14* (6), 684–688.
- Kasinath, V.; Valentini, K. G.; Wand, A. J. A C-13 Labeling Strategy Reveals a Range of Aromatic Side Chain Motion in Calmodulin. *J. Am. Chem. Soc.* **2013**, *135* (26), 9560–9563.
- Lichtenecker, R. J. Synthesis of aromatic C-13/H-2-alpha-ketoacid precursors to be used in selective phenylalanine and tyrosine protein labelling. *Org. Biomol. Chem.* **2014**, *12* (38), 7551–7560.
- Lichtenecker, R. J.; Weinhaupl, K.; Schmid, W.; Konrat, R. alpha-Ketoacids as precursors for phenylalanine and tyrosine labelling in cell-based protein overexpression. *J. Biomol. NMR* **2013**, *57* (4), 327–331.
- Lundström, P.; Teilum, K.; Carstensen, T.; Bezsonova, I.; Wiesner, S.; Hansen, D. F.; Religa, T. L.; Akke, M.; Kay, L. E. Fractional C-13 enrichment of isolated carbons using [1-C-13]- or [2-C-13]-glucose facilitates the accurate measurement of dynamics at backbone C-alpha and side-chain methyl positions in proteins. *J. Biomol. NMR* **2007**, *38* (3), 199–212.
- Teilum, K.; Brath, U.; Lundström, P.; Akke, M. Biosynthetic C-13 labeling of aromatic side chains in proteins for NMR relaxation measurements. *J. Am. Chem. Soc.* **2006**, *128* (8), 2506–2507.
- Weininger, U. Site-selective ¹³C labeling of proteins using erythrose. *J. Biomol. NMR* **2017**, *67* (3), 191–200.
- Weininger, U. Optimal Isotope Labeling of Aromatic Amino Acid Side Chains for NMR Studies of Protein Dynamics. *Methods Enzymol.* **2019**, *614*, 67–86.
- Weininger, U.; Brath, U.; Modig, K.; Teilum, K.; Akke, M. Off-resonance rotating-frame relaxation dispersion experiment for C-13 in aromatic side chains using L-optimized TROSY-selection. *J. Biomol. NMR* **2014**, *59* (1), 23–29.
- Weininger, U.; Respondek, M.; Akke, M. Conformational exchange of aromatic side chains characterized by L-optimized TROSY-selected C-13 CPMG relaxation dispersion. *J. Biomol. NMR* **2012**, *54* (1), 9–14.
- Raum, H. N.; Dreydoppel, M.; Weininger, U. Conformational exchange of aromatic side chains by (1)H CPMG relaxation dispersion. *J. Biomol. NMR* **2018**, *72* (1–2), 105–114.
- Raum, H. N.; Schorghuber, J.; Dreydoppel, M.; Lichtenecker, R. J.; Weininger, U. Site-selective (1)H/(2)H labeling enables artifact-free (1)H CPMG relaxation dispersion experiments in aromatic side chains. *J. Biomol. NMR* **2019**, *73* (10–11), 633–639.
- Wagner, G. Activation Volumes for the Rotational Motion of Interior Aromatic Rings in Globular-Proteins Determined by High-

- Resolution H-1-Nmr at Variable Pressure. *FEBS Lett.* **1980**, *112* (2), 280–284.
- (33) Akasaka, K.; Kitahara, R.; Kamatari, Y. O. Exploring the folding energy landscape with pressure. *Arch. Biochem. Biophys.* **2013**, *531* (1–2), 110–5.
- (34) Luong, T. Q.; Kapoor, S.; Winter, R. Pressure-A Gateway to Fundamental Insights into Protein Solvation, Dynamics, and Function. *ChemPhysChem* **2015**, *16* (17), 3555–3571.
- (35) Kalbitzer, H. R. High Pressure NMR Methods for Characterizing Functional Substates of Proteins. *Subcell. Biochem.* **2015**, *72*, 179–197.
- (36) Ando, N.; Barstow, B.; Baase, W. A.; Fields, A.; Matthews, B. W.; Gruner, S. M. Structural and thermodynamic characterization of T4 lysozyme mutants and the contribution of internal cavities to pressure denaturation. *Biochemistry* **2008**, *47* (42), 11097–11109.
- (37) Weber, G.; Drickamer, H. G. The Effect of High-Pressure Upon Proteins and Other Biomolecules. *Q. Rev. Biophys.* **1983**, *16* (1), 89–112.
- (38) Klamt, A.; Nagarathinam, K.; Tanabe, M.; Kumar, A.; Balbach, J. Hyperbolic Pressure-Temperature Phase Diagram of the Zinc-Finger Protein apoKt11 Detected by NMR Spectroscopy. *J. Phys. Chem. B* **2019**, *123* (4), 792–801.
- (39) Roche, J.; Caro, J. A.; Norberto, D. R.; Barthe, P.; Roumestand, C.; Schlessman, J. L.; Garcia, A. E.; Garcia-Moreno E, B.; Royer, C. A. Cavities determine the pressure unfolding of proteins. *Proc. Natl. Acad. Sci. U. S. A.* **2012**, *109* (18), 6945–6950.
- (40) Hawley, S. A. Reversible Pressure-Temperature Denaturation of Chymotrypsinogen. *Biochemistry* **1971**, *10* (13), 2436–2442.
- (41) Akasaka, K.; Tezuka, T.; Yamada, H. Pressure-induced changes in the folded structure of lysozyme. *J. Mol. Biol.* **1997**, *271* (5), 671–8.
- (42) Dreydoppel, M.; Becker, P.; Raum, H. N.; Gröber, S.; Balbach, J.; Weininger, U. Equilibrium and Kinetic Unfolding of GB1: Stabilization of the Native State by Pressure. *J. Phys. Chem. B* **2018**, *122* (38), 8846–8852.
- (43) Munte, C. E.; Beck Erlach, M.; Kremer, W.; Koehler, J.; Kalbitzer, H. R. Distinct Conformational States of the Alzheimer -Amyloid Peptide Can Be Detected by High-Pressure NMR Spectroscopy. *Angew. Chem., Int. Ed.* **2013**, *52* (34), 8943–8947.
- (44) Nisius, L.; Grzesiek, S. Key stabilizing elements of protein structure identified through pressure and temperature perturbation of its hydrogen bond network. *Nat. Chem.* **2012**, *4* (9), 711–717.
- (45) Roche, J.; Royer, C. A.; Roumestand, C. Monitoring protein folding through high pressure NMR spectroscopy. *Prog. Nucl. Magn. Reson. Spectrosc.* **2017**, *102*, 15–31.
- (46) Vajpai, N.; Nisius, L.; Wiktor, M.; Grzesiek, S. High-pressure NMR reveals close similarity between cold and alcohol protein denaturation in ubiquitin. *Proc. Natl. Acad. Sci. U. S. A.* **2013**, *110* (5), E368–E376.
- (47) Caro, J. A.; Wand, A. J. Practical aspects of high-pressure NMR spectroscopy and its applications in protein biophysics and structural biology. *Methods* **2018**, *148*, 67–80.
- (48) Wilton, D. J.; Kitahara, R.; Akasaka, K.; Pandya, M. J.; Williamson, M. P. Pressure-Dependent Structure Changes in Barnase on Ligand Binding Reveal Intermediate Rate Fluctuations. *Biophys. J.* **2009**, *97* (5), 1482–1490.
- (49) Wilton, D. J.; Tunnicliffe, R. B.; Kamatari, Y. O.; Akasaka, K.; Williamson, M. P. Pressure-induced changes in the solution structure of the GB1 domain of protein G. *Proteins: Struct., Funct., Genet.* **2008**, *71* (3), 1432–1440.
- (50) Zhang, Y.; Kitazawa, S.; Peran, I.; Stenzoski, N.; McCallum, S. A.; Raleigh, D. P.; Royer, C. A. High Pressure ZZ-Exchange NMR Reveals Key Features of Protein Folding Transition States. *J. Am. Chem. Soc.* **2016**, *138* (46), 15260–15266.
- (51) Alderson, T. R.; Charlier, C.; Torchia, D. A.; Anfirud, P.; Bax, A. Monitoring Hydrogen Exchange During Protein Folding by Fast Pressure Jump NMR Spectroscopy. *J. Am. Chem. Soc.* **2017**, *139* (32), 11036–11039.
- (52) Charlier, C.; Alderson, T. R.; Courtney, J. M.; Ying, J. F.; Anfirud, P.; Bax, A. Study of protein folding under native conditions by rapidly switching the hydrostatic pressure inside an NMR sample cell. *Proc. Natl. Acad. Sci. U. S. A.* **2018**, *115* (18), E4169–E4178.
- (53) Bezsonova, I.; Korzhnev, D. M.; Prosser, R. S.; Forman-Kay, J. D.; Kay, L. E. Hydration and packing along the folding pathway of SH3 domains by pressure-dependent NMR. *Biochemistry* **2006**, *45* (15), 4711–4719.
- (54) Tugarinov, V.; Libich, D. S.; Meyer, V.; Roche, J.; Clore, G. M. The Energetics of a Three-State Protein Folding System Probed by High-Pressure Relaxation Dispersion NMR Spectroscopy. *Angew. Chem., Int. Ed.* **2015**, *54* (38), 11157–11161.
- (55) Kasinath, V.; Fu, Y. N.; Sharp, K. A.; Wand, A. J. A Sharp Thermal Transition of Fast Aromatic-Ring Dynamics in Ubiquitin. *Angew. Chem., Int. Ed.* **2015**, *54* (1), 102–7.
- (56) Persson, F.; Halle, B. Compressibility of the protein-water interface. *J. Chem. Phys.* **2018**, *148* (21), 215102.
- (57) Schiffer, J. M.; Feher, V. A.; Malmstrom, R. D.; Sida, R.; Amaro, R. E. Capturing Invisible Motions in the Transition from Ground to Rare Excited States of T4 Lysozyme L99A. *Biophys. J.* **2016**, *111* (8), 1631–1640.
- (58) Taulier, N.; Chalikian, T. V. Compressibility of protein transitions. *Biochim. Biophys. Acta, Protein Struct. Mol. Enzymol.* **2002**, *1595* (1–2), 48–70.
- (59) Marchi, M. Compressibility of cavities and biological water from Voronoi volumes in hydrated proteins. *J. Phys. Chem. B* **2003**, *107* (27), 6598–6602.
- (60) Lassalle, M. W.; Yamada, H.; Akasaka, K. The pressure-temperature free energy-landscape of staphylococcal nuclease monitored by H-1 NMR. *J. Mol. Biol.* **2000**, *298* (2), 293–302.
- (61) Prehoda, K. E.; Mooberry, E. S.; Markley, J. L. Pressure denaturation of proteins: Evaluation of compressibility effects. *Biochemistry* **1998**, *37* (17), 5785–5790.
- (62) Gallagher, T.; Alexander, P.; Bryan, P.; Gilliland, G. L. 2 Crystal-Structures of the B1 Immunoglobulin-Binding Domain of Streptococcal Protein-G and Comparison with Nmr. *Biochemistry* **1994**, *33* (15), 4721–4729.
- (63) Olechnovic, K.; Venclovas, C. Voronota: A Fast and Reliable Tool for Computing the Vertices of the Voronoi Diagram of Atomic Balls. *J. Comput. Chem.* **2014**, *35* (8), 672–681.
- (64) Richards, F. M. Interpretation of Protein Structures - Total Volume, Group Volume Distributions and Packing Density. *J. Mol. Biol.* **1974**, *82* (1), 1–14.
- (65) Tsai, J.; Taylor, R.; Chothia, C.; Gerstein, M. The packing density in proteins: Standard radii and volumes. *J. Mol. Biol.* **1999**, *290* (1), 253–266.
- (66) Rumble, J. R. *CRC handbook of chemistry and physics*, 101st ed.; CRC Press/Taylor & Francis Group: Boca Raton, 2020.
- (67) Lindman, S.; Xue, W. F.; Szczepankiewicz, O.; Bauer, M. C.; Nilsson, H.; Linse, S. Salting the charged surface: pH and salt dependence of protein G B1 stability. *Biophys. J.* **2006**, *90* (8), 2911–21.
- (68) Mulder, F. A. A.; de Graaf, R. A.; Kaptein, R.; Boelens, R. An off-resonance rotating frame relaxation experiment for the investigation of macromolecular dynamics using adiabatic rotations. *J. Magn. Reson.* **1998**, *131* (2), 351–357.
- (69) Peterson, R. W.; Wand, A. J. Self contained high pressure cell, apparatus and procedure for the preparation of encapsulated proteins dissolved in low viscosity fluids for NMR spectroscopy. *Rev. Sci. Instrum.* **2005**, *76* (9), 094101.
- (70) Delaglio, F.; Grzesiek, S.; Vuister, G. W.; Zhu, G.; Pfeifer, J.; Bax, A. Nmrpipe - a Multidimensional Spectral Processing System Based on Unix Pipes. *J. Biomol. NMR* **1995**, *6* (3), 277–293.
- (71) Ahlner, A.; Carlsson, M.; Jonsson, B. H.; Lundström, P. PINT: a software for integration of peak volumes and extraction of relaxation rates. *J. Biomol. NMR* **2013**, *56* (3), 191–202.
- (72) Nair, S. K.; Christianson, D. W. Unexpected Ph-Dependent Conformation of His-64, the Proton Shuttle of Carbonic Anhydrase-II. *J. Am. Chem. Soc.* **1991**, *113* (25), 9455–9458.
- (73) Imai, T.; Nomura, H.; Kinoshita, M.; Hirata, F. Partial molar volume and compressibility of alkali-halide ions in aqueous solution:

Hydration shell analysis with an integral equation theory of molecular liquids. *J. Phys. Chem. B* **2002**, *106* (29), 7308–7314.

(74) Landau, L. D.; Lifshits, E. M. *Statistical physics Pt. 1*, 3rd ed.; Butterworth-Heinemann: Oxford, 1980.

(75) Press, W. H.; Teukolsky, S. A.; Vetterling, W. T.; Flannery, B. P. *Numerical recipes in C++: the art of scientific computing*, 2nd ed.; Cambridge University Press: Cambridge, 2002.

(76) Bevington, P. R.; Robinson, D. K. *Data reduction and error analysis for the physical sciences*, 3rd ed.; McGraw-Hill: Boston, 2002.

Paper IV



Characterizing Fast Conformational Exchange of Aromatic Rings Using Residual Dipolar Couplings: Distinguishing Jumplike Flips from Other Exchange Mechanisms

Matthias Dreydoppel, Mikael Akke, and Ulrich Weininger*



Cite This: *J. Phys. Chem. B* 2022, 126, 7950–7956



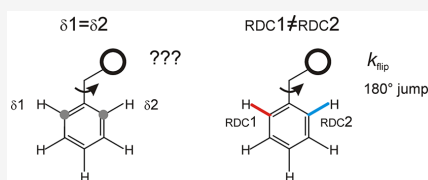
Read Online

ACCESS |

Metrics & More

Article Recommendations

ABSTRACT: Aromatic ring flips are a hallmark of protein dynamics. They are experimentally studied by NMR spectroscopy, where recent advances have led to improved characterization across a wide range of time scales. Results on different proteins have been interpreted as continuous diffusive ring rotations or jumplike flips, leading to diverging views of the protein interior as being fluidlike or solidlike, respectively. It is challenging to distinguish between these mechanisms and other types of conformational exchange because chemical-shift-mediated line broadening provides only conclusive evidence for ring flips only if the system can be moved from the slow- to intermediate/fast-exchange regime. Moreover, whenever the chemical shift difference between the two symmetry-related sites is close to zero, it is not generally possible to determine the exchange time scale. Here we resolve these issues by measuring residual dipolar coupling (RDC)-mediated exchange contributions using NMR relaxation dispersion experiments on proteins dissolved in dilute liquid crystalline media. Excellent agreement is found between the experimental difference in RDC between the two symmetry-related sites and the value calculated from high-resolution X-ray structures, demonstrating that dynamics measured for F52 in the B1 domain of protein G reports on distinct, jumplike flips rather than other types of conformational exchange.



that the transition state is liquidlike, whereas the ground state is solidlike. This result differs from conclusions reached in another study of the dynamics of surface-exposed aromatic residues in ubiquitin, which suggest that the ground state is liquidlike and the aromatic rings undergo continuous diffusive rotations.²⁴ Thus, further studies are warranted to provide detailed insights into the mechanism and energetics of aromatic ring dynamics and how these properties might differ among aromatic side chains located in different environments, e.g., in the protein core or closer to the protein surface.

INTRODUCTION

Conformational dynamics of proteins is essential for biological function. Aromatic ring flips, i.e., 180° rotations of the χ_2 dihedral angle in Phe and Tyr side chains, are a hallmark of transient conformational fluctuations in proteins.^{1,2} Aromatic side chains in the interior of globular proteins commonly undergo rapid rotations, as gauged by the observation of a single peak in the NMR spectrum originating from the two symmetry-related nuclei of the ring. In the past, ring flip rates have been measured for only a limited number of proteins by using line shape analysis or longitudinal exchange experiments.^{1,3–6} The development of site-selective isotope labeling schemes for aromatic side chains^{7–14} has enabled relaxation dispersion experiments for aromatic ¹³C and ¹H sites^{15–18} and led to a renaissance in studying ring flips by NMR spectroscopy.^{19–25}

The rotation of an aromatic side chain located inside the protein core requires that the surrounding side chains transiently create sufficient volume to accommodate the ring rotation. Temperature- and pressure-dependent experiments make it possible to determine the activation enthalpy (ΔH^\ddagger), entropy (ΔS^\ddagger), and volume (ΔV^\ddagger) of this process.^{1,5,20,21,26,27} Recently, we presented a combined analysis of temperature- and pressure-dependent ring flip data that enabled us to also determine the change in compressibility ($\Delta\kappa^\ddagger$) between ground and transition states of a ring flip,¹⁹ which indicates

that the transition state is liquidlike, whereas the ground state is solidlike. This result differs from conclusions reached in another study of the dynamics of surface-exposed aromatic residues in ubiquitin, which suggest that the ground state is liquidlike and the aromatic rings undergo continuous diffusive rotations.²⁴ Thus, further studies are warranted to provide detailed insights into the mechanism and energetics of aromatic ring dynamics and how these properties might differ among aromatic side chains located in different environments, e.g., in the protein core or closer to the protein surface.

To date, the study of ring flips by solution-state NMR spectroscopy has mainly relied on measuring exchange contributions to the line width (or longitudinal exchange for very slow cases), caused by differences in the chemical shifts of the symmetry-related pairs of ¹H δ , ¹He, ¹³C δ , or ¹³C ϵ nuclei. However, it is not uncommon that none of these sites display significant differences in chemical shift, thereby making ring flip studies by NMR relaxation difficult or impossible.^{20,22,28} Furthermore, when separate peaks cannot be observed for the

Received: July 19, 2022

Revised: August 3, 2022

Published: September 30, 2022



two sides of the aromatic ring, it has been impossible to determine with certainty that exchange broadening is due to ring flips rather than other types of conformational exchange.

Here we demonstrate that these impediments can be resolved by studying exchange broadening mediated by residual dipolar couplings,^{29,30} introduced by partial alignment of the protein in dilute liquid crystalline media.³¹ The use of RDC-mediated conformational exchange is particularly powerful in the case of aromatic ring flips because the approach resolves cases where the chemical shift difference is (close to) zero and, importantly, provides critical structural information to distinguish whether aromatic rings undergo distinct, jumplike flips, or continuous diffusive ring rotation as invoked recently,²⁴ or other types of conformational exchange.

MATERIALS AND METHODS

Protein Expression and Purification. The 1-¹³C and 2-¹³C glucose-labeled B1 domain of Staphylococcal protein G (GB1; UniProtKB P06654) carrying the mutations T2Q, N8D, and N37D (QDD-GB1) was expressed and purified as described elsewhere.³² It has been established that QDD-GB1 has the same structure as wild-type GB1 and that comparisons between the two variants are valid;³² henceforth, we refer to the triple mutant simply as GB1. 1-¹³C glucose labeling results in site-selective ¹³C enrichment at the δ positions of Phe and Tyr residues, while 2-¹³C glucose labeling results in site-selective ¹³C enrichment at their ϵ positions.^{10,12,14}

NMR Sample Preparation. To induce weak alignment of the protein in the static magnetic field, samples were prepared by using dilute liquid crystalline phases consisting of hexaethylene glycol monododecyl ether (C₁₂E₆, Sigma) and *n*-hexanol (Fluka), which were used without further purification. C₁₂E₆ was dissolved in the protein solution (2.3 mM of 1-¹³C or 3.3 mM of 2-¹³C glucose labeled GB1) in H₂O containing 10% D₂O to reach a C₁₂E₆/water ratio of 8 wt %.³³ The pH was adjusted to 7.0, followed by addition of *n*-hexanol to a C₁₂E₆/*n*-hexanol molar ratio of 0.64. The alcohol was added in microliter steps under vigorous mixing and shaking of the solution at a temperature of 35 °C. After cooling below 10 °C, the solution became opalescent and stably monophasic and was stored at 4 °C. Aqueous GB1 samples were dissolved to a concentration of 1 mM in 20 mM HEPES, 90% H₂O/10% D₂O, with small amounts of NaN₃. The pH was adjusted to 7.0 in the sample.

NMR Spectroscopy. All experiments were performed at a static magnetic field strength of 14.1 T. Experiments on the 1-¹³C glucose-labeled sample were performed on a Bruker Avance IV spectrometer equipped with a cryoprobe, while RDC measurements on the 2-¹³C glucose-labeled sample were performed on a Bruker Avance III spectrometer equipped with a room temperature probe. Aromatic L-optimized TROSY-selected ¹³C R_{1 ρ} relaxation dispersion experiments¹⁶ were performed with the spin-lock placed on-resonance with F52 δ at temperatures of 5, 10, and 15 °C. In short, the pulse sequence selects the TROSY component by using an S³E element,³⁴ and the relaxation period is divided into two blocks separated by a S³CT selective inversion element.³⁵ In each relaxation block,¹³C magnetization was aligned along the B₁ field axis by using a 4 ms tan/tanh adiabatic ramp,³⁶ spin-locked on-resonance using spin-lock field strengths of $\omega_1/2\pi = \{923, 1259, 1688, 2048, 2610, 3784, 4313, 5486\}$ Hz, and finally returned to the original state by a time-reversed

adiabatic ramp. Two separate experiments were acquired with and without the spin-lock relaxation period for each effective field, from which relaxation rate constants were calculated as $R_{1\rho} = \ln(I_{\text{thx}}/I_{\text{ref}})/t_{\text{thx}}$ where I_{thx} and I_{ref} are the intensities measured in the spectra acquired with and without the relaxation period, respectively, and $t_{\text{thx}} = 20$ ms is the length of the relaxation period. Relaxation dispersion data were acquired as an interleaved pseudo-3D experiment, where the effective field strengths were varied prior to incrementing the indirect evolution period t_1 .

Relaxation Data Analysis. NMR spectra were processed with NMRPipe³⁷ and analyzed with PINT.³⁸ The on-resonance R_{1 ρ} relaxation rate constant is the sum of the intrinsic transverse relaxation rate constant and the exchange contribution: $R_{1\rho} = R_{2,0} + R_{\text{ex}}$. Miloushev and Palmer have derived a general expression for symmetric two-state exchange³⁹ that is applicable to the case of aromatic ring flips, which involves fixed populations, $p_a = p_b = 0.5$. In the present case, where the spin-lock is applied on-resonance with the average signal, the exchange contribution can be expressed as

$$R_{\text{ex}} = \frac{k}{2} - \frac{k}{2} \sqrt{1 - \frac{\Delta\omega^2}{\frac{\omega_a^2\omega_b^2}{\omega_1^2} + k^2 \left[1 - \frac{\Delta\omega^2}{4} \frac{\omega_a^2 + \omega_b^2}{\omega_a^2\omega_b^2 + k^2\omega_1^2} \right]}} \quad (1)$$

where $\Delta\omega$ is the difference in resonance frequency between the two sites, ω_a and ω_b are the effective field strengths at the resonance frequency of each site (i.e., $\omega_a = ((\omega_{a,\text{RDC}}/2 + \Omega_a)^2 + \omega_1^2)$, and vice versa for ω_b), Ω_a is the chemical shift (Larmor frequency) offset from the carrier, $\omega_{a,\text{RDC}}$ is the RDC, ω_1 is the spin-lock field strength (all expressed in units of rad/s), and $k = 2k_{\text{flip}}$, with k_{flip} being the ring flip rate. Data sets were fitted simultaneously, while imposing the restrictions $k_{\text{flip}}(T_{\text{high}}) > k_{\text{flip}}(T_{\text{low}})$ and $R_{2,0}(T_{\text{high}}) \leq R_{2,0}(T_{\text{low}})$.²⁰ In addition, the restriction $\Delta\omega(T_{\text{high}}) < \Delta\omega(T_{\text{low}})$ was used, which takes into account the reduced alignment strength at higher temperatures.³³ T_{high} and T_{low} denote the sample temperatures of the relaxation dispersion experiments. Errors in the fitted parameters were estimated by using Monte Carlo simulations.⁴⁰

RDC Measurements and Structure-Based Predictions. Backbone ¹³C α -¹H α RDCs and aromatic ¹³C-¹H RDCs were measured in non-decoupled, non-constant time ¹H-¹³C HSQC spectra, with and without alignment medium, at 5 °C. RDCs were measured for 11 clearly resolved cross-peaks corresponding to sites T17 α , T18 α , A26 α , K31 α , W43- ($\alpha, \eta, 2, \epsilon, 3, \zeta, 2, \zeta, 3$), T51 α , and F52 α . The resulting RDCs were used to calculate the alignment tensors (AT) based on the 1.92 and 1.14 Å X-ray crystal structures (PDB entries 1PGB⁴¹ and 2GI9,⁴² respectively), with the program REDCAT,⁴³ provided in NMRbox.⁴⁴ In REDCAT five independent RDCs in combination with the proteins structure are sufficient for AT calculation.⁴³ Its robustness was checked by systematically excluding each of the 11 RDCs, leading to the same results within margin of error. Aromatic RDCs in Tyr and Phe residues were predicted based on the experimentally determined AT and the crystal structures. Errors in the predicted RDCs were estimated as one standard deviation of RDCs predicted from 200 replicate REDCAT calculations.

The difference between the ¹H-¹³C RDC values predicted for the individual symmetry-related sites ($\delta 1$ and $\delta 2$) can be

compared with the value ($\Delta\omega_{\text{RDC}}$) determined experimentally from the RDC-mediated relaxation dispersion data

$$\Delta\omega_{\text{RDC}} = |\omega_{\delta_1, \text{RDC}} - \omega_{\delta_2, \text{RDC}}|/2 \quad (2)$$

The factor 1/2 arises because only one-half of the RDC affects the TROSY line, while the other half affects the anti-TROSY line. The absolute value arises from $\Delta\omega^2$ (see eq 1). The averaged value of the RDC measured in the spectrum is given by

$$\langle\omega_{\text{RDC}}\rangle = (\omega_{\delta_1, \text{RDC}} + \omega_{\delta_2, \text{RDC}})/2 \quad (3)$$

RDCs for δ_1 and δ_2 were calculated as a function of the χ_2 dihedral angle, as follows. Using both the 1PGB and 2GI9 structures, the atomic coordinates of the F52 aromatic ring were updated following stepwise rotation by 2° around the C_β - C_γ - C_ζ axis, while keeping all other atom coordinates constant. The PDB coordinates were saved after each step to cover in total a rotation of 360° . On the basis of these hypothetical, intermediate state structures and the previously calculated AT, ^{13}C - ^1H RDCs were calculated by using REDCAT for each of the 180 different χ_2 dihedral angles.

RESULTS AND DISCUSSION

In isotropic solutions, aromatic ring flips of Phe and Tyr residues can normally be studied only if they possess different chemical shifts in the two δ or ε positions; although in special cases it can be possible to measure ring flips rates even if the shifts are identical.²² In total, there are four sites to study: $^{13}\text{C}\delta$ and $^{13}\text{C}\varepsilon$ (Figure 1A) and $^1\text{H}\delta$ and $^1\text{H}\varepsilon$ (Figure 1B). Because

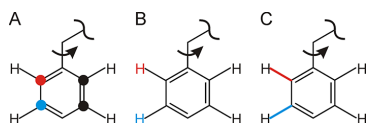


Figure 1. Differences in resonance frequencies between the two symmetry-related positions of the aromatic ring enable measurement of ring flip rates: (A) ^{13}C chemical shifts differ between the colored and black carbon nuclei; (B) ^1H chemical shifts differ between the colored and black hydrogen nuclei; (C) RDCs differ between the colored and black ^1H - ^{13}C moieties. The δ and ε positions are colored red and blue, respectively.

of the narrow chemical shift range of aromatic nuclei and the strong coupling between them, relaxation dispersion experiments require site-selective ^{13}C labeling to probe the carbons^{7,10–14} and additional ^2H labeling of vicinal sites to probe the protons.^{15,18,45} It is not uncommon that only a subset of the four sites can be studied, either because the chemical shifts of the two symmetric positions of the ring are identical or because a site is severely broadened by exchange under the desired experimental conditions. In GB1 the chemical shifts have been measured for three aromatic residues under slow exchange conditions induced by low temperature and high pressure.²⁰ Y3 displays chemical shift differences for all four sites: $^1\text{H}\delta$, $^{13}\text{C}\delta$, $^1\text{H}\varepsilon$, and $^{13}\text{C}\varepsilon$. F30 displays chemical shift differences for $^1\text{H}\delta$, $^{13}\text{C}\delta$, and $^1\text{H}\varepsilon$, with the δ position being severely broadened throughout the permissible temperature range from 1°C to the onset of unfolding at 40°C . F52 only displays chemical shift differences for $^{13}\text{C}\varepsilon$, but not for the other nuclei.

Here we take advantage of the fact that the RDC usually differs between the two sides of the ring (Figure 1C). By studying RDC-mediated exchange line broadening using relaxation dispersion methods, we increase the number of possible probes for characterizing ring flips from four to six (i.e., four chemical shifts plus two RDCs). Moreover, RDCs allow for a direct structural interpretation, which is rarely possible based on chemical shifts, except in cases where the chemical shift difference between the symmetry-related sites has been measured under slow exchange conditions. We used F52 $^{13}\text{C}\delta$ as a critical test case because the δ_1 and δ_2 carbons have identical chemical shifts ($\Delta\omega_{\text{iso}} = 0$) and therefore yield flat ^{13}C relaxation dispersion profiles in isotropic solutions (Figure 2A).

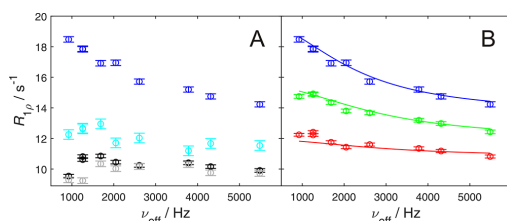


Figure 2. Relaxation dispersion profiles for F52 $^{13}\text{C}\delta$ and Y33 $^{13}\text{C}\delta$. Data were recorded using on-resonance spin-lock fields at a static magnetic field strength of 14.1 T. (A) Relaxation dispersion profiles acquired at 5°C in aqueous buffer (F52 in cyan and Y33 in gray) and $\text{C}_{12}\text{E}_6/n$ -hexanol liquid crystalline alignment medium (F52 in blue and Y33 in black). (B) Relaxation dispersion profiles acquired in alignment medium at temperatures of 5°C (blue, as in panel A), 10°C (green), and 15°C (red). The continuous lines represent the fitted symmetric two-state exchange model (eq 1).

RDC-Mediated Exchange Line Broadening Studied by ^{13}C $R_{1\rho}$ Relaxation Dispersion. Aromatic ^{13}C $R_{1\rho}$ relaxation experiments performed on F52 δ in $\text{C}_{12}\text{E}_6/n$ -hexanol liquid crystalline medium³³ reveals a significant dispersion profile, even though the ^{13}C chemical shift difference is zero,²⁰ as also evidenced by a flat dispersion profile in isotropic solvent (Figure 2A). In contrast, Y33 δ , which undergoes fast ring flips, displays flat dispersion profiles independent from the alignment medium. This result directly points to a significant difference in RDC between the two symmetry-related positions of the aromatic ring that enables a reliable fit of exchange rates (Figure 2B).

Fitting eq 1 to the experimental data yields exchange rates that agree well with previously determined values obtained from ^{13}C $R_{1\rho}$ data for the F52 ε position (Table 1), thereby validating RDC-mediated exchange as a method to study

Table 1. Ring Flip Rates of F52 δ Determined by RDC-Enabled ^{13}C $R_{1\rho}$ Relaxation Dispersion Experiments

T (°C)	$k_{\text{flip}}^{13\text{C}\delta}$ (10^3 s^{-1})	$k_{\text{flip}}^{13\text{C}\varepsilon}$ (10^3 s^{-1})	$\Delta\omega_{\text{RDC}}$ (Hz)	$\langle\omega_{\text{RDC}}\rangle$ (Hz)
5	6.9 ± 1.5	7.8 ± 1.0	90 ± 7	12 ± 1
10 ^b	8.7 ± 1.8	8.5 ± 0.8	78 ± 9	8 ± 1
15	9.0 ± 6.2	10.2 ± 0.7	45 ± 10	5 ± 1

^aDerived from ref 19. ^bIdentical results were obtained on a sample of 1 mM protein concentration: $k_{\text{ex}} = (8.8 \pm 3.0) \times 10^3 \text{ s}^{-1}$ and $\Delta\omega_{\text{RDC}} = 74 \pm 8 \text{ Hz}$.

aromatic ring flips. The relaxation dispersion profiles are more pronounced at lower temperatures (Figure 2B), in agreement with the expectation that decreased rates of ring flipping lead to greater exchange contributions to $R_{1\rho}$ (cf. eq 1). In addition, the alignment is weaker at higher temperature, leading to reduced $R_{1\rho}$ as a consequence of reduced $\Delta\omega_{\text{RDC}}$, as can also be seen from the lower average RDC value, $\langle\omega_{\text{RDC}}\rangle$, measured in the ^1H – ^{13}C HSQC spectrum (Table 1).

Unfortunately, none of the other aromatic residues in GB1 are amenable to RDC-mediated exchange characterization for the following reasons: Y3 has the lowest $\Delta\omega_{\text{RDC}}$ value and displays significant differences in isotropic ^{13}C chemical shifts ($\Delta\omega_{\text{iso}} = 210$ and 316 Hz at 14.1 T), which renders the contribution from the RDC-mediated broadening relatively small; Y33 is surface exposed and exhibits very fast ring flips; and F30 and Y45 are severely broadened at conditions optimal for $R_{1\rho}$ experiment. The latter three cases represent general challenges in studying ring flips that are independent of the RDC approach. In fact, our approach should be widely applicable to aromatic residues suitable for characterization by relaxation dispersion experiments because $\Delta\omega_{\text{RDC}}$ is expected to be sufficiently large in the majority of cases. As an example, we calculated $\Delta\omega_{\text{RDC}}$ values for all δ and ε positions of the Tyr and Phe residues in GB1, based on the crystal structure and the determined alignment tensor. The predicted $\Delta\omega_{\text{RDC}}$ values range between 46 and 97 Hz, which are large enough to produce significant relaxation dispersion profiles provided that the exchange rate falls in a suitable regime. For comparison, these $\Delta\omega_{\text{RDC}}$ values correspond to ^{13}C chemical shift differences of 0.3 and 0.65 ppm at a magnetic field strength of 14.1 T. In rare cases the ^1H – ^{13}C bond vectors of both symmetry-related sites might be aligned identically with respect to the laboratory frame, which would yield $\Delta\omega_{\text{RDC}}$ near zero. This problem can be circumvented by choosing an alignment medium that generates a different alignment tensor. Otherwise, we expect that RDC-mediated exchange line broadening will serve as a valuable probe of aromatic side chain dynamics.

To validate the fitted $\Delta\omega_{\text{RDC}}$ values, we plotted the temperature-dependent data against $\langle\omega_{\text{RDC}}\rangle$, which indeed shows the expected linear correlation (Figure 3) (cf. eqs 2 and 3). By taking the linear combinations of $\Delta\omega_{\text{RDC}}$ and $\langle\omega_{\text{RDC}}\rangle$,

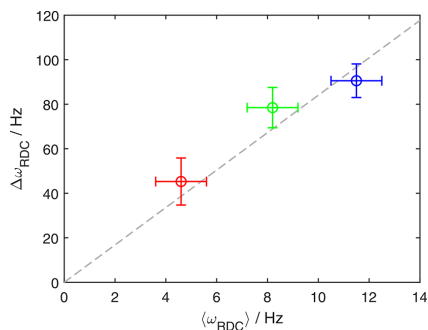


Figure 3. Validation of $\Delta\omega_{\text{RDC}}$ values extracted from ^{13}C $R_{1\rho}$ relaxation dispersion data. Fitted $\Delta\omega_{\text{RDC}}$ values are plotted against $\langle\omega_{\text{RDC}}\rangle$ measured in the non-decoupled ^1H – ^{13}C HSQC spectra at 5 °C (blue), 10 °C (green), and 15 °C (red). The dashed line is a linear fit with zero intercept drawn to show the expected linearity.

we extract $\omega_{\delta 1, \text{RDC}} = 102 \pm 7$ Hz and $\omega_{\delta 2, \text{RDC}} = -78 \pm 7$ Hz. These RDCs can be compared with values predicted from crystal structures, which provides insights into the mechanism of ring rotations, as described below.

RDC Values Determined by Relaxation Dispersion Agree with Predictions from Crystal Structures. We interpreted the fitted $\Delta\omega_{\text{RDC}}$ values and $\langle\omega_{\text{RDC}}\rangle$ determined at 5 °C in structural terms. We first determined the alignment tensor of GB1 from the experimental RDC values and two high-resolution crystal structures, 1PGB⁴¹ (1.92 Å) and 2GI9⁴² (1.14 Å), using REDCAT.⁴³ On the basis of the structural coordinates and the resulting alignment tensors, we then predicted the ^1H – ^{13}C RDC values for the individual symmetry-related sites, $\omega_{\delta 1, \text{RDC}}$ and $\omega_{\delta 2, \text{RDC}}$, of F52 δ 1 and F52 δ 2. The experimental and predicted RDCs are compared in Table 2. Excellent agreement is observed between the

Table 2. Experimental and Predicted RDC Values for F52 δ at 5 °C^a

	$\omega_{\delta 1, \text{RDC}}$	$\omega_{\delta 2, \text{RDC}}$	$\Delta\omega_{\text{RDC}}$	$\langle\omega_{\text{RDC}}\rangle$
experiment	102 ± 7	-78 ± 7	90 ± 7	12 ± 1
1PGB	100 ± 2	-83 ± 2	91 ± 2	9 ± 2
2GI9	102 ± 3	-97 ± 3	99 ± 2	2 ± 2

^aUnits in Hz.

predicted and experimental values of $\Delta\omega_{\text{RDC}}$ and $\langle\omega_{\text{RDC}}\rangle$ when comparing with the 1PGB crystal structure. The 2GI9 structure shows slightly less good agreement, particularly for $\omega_{\delta 2, \text{RDC}}$, while the agreement for $\Delta\omega_{\text{RDC}}$ is still reasonable.

Importantly, the agreement between the experimental results for F52 δ and the RDCs predicted from the orientations of the H–C vectors in the crystal structure clearly indicates that the observed exchange is caused by aromatic ring flips, rather than other types of conformational exchange, such as exchange between alternative ring orientations induced by changes in the χ_1 dihedral angle. While large-scale χ_1 fluctuations are not expected to occur readily for aromatic side chains that are packed tightly in the protein core, such as F52 in GB1, this type of motion is possible for solvent exposed residues. Thus, quantitative measurement of RDC-mediated exchange makes it possible to conclusively identify ring flip dynamics even for aromatic residues that undergo fast exchange on the chemical shift time scale under all attainable experimental conditions.

It should be noted that the present evidence for jumplike ring flips does not suggest that the ring does not undergo ground-state fluctuations within each rotamer well. However, the correlation times of intrawell fluctuations are expected to be much shorter (faster) than the correlation times of ring flips, which are rare events in the case of buried rings in the interior of proteins. There is a difference of approximately 10^5 between these correlation times (sub-ns and 0.1 ms in the present case). Thus, the intrawell fluctuations are completely averaged prior to each ring flip, and the ring-flip rate extracted from the relaxation dispersion data is governed by the difference between the population-weighted ground-state and transition-state free energies.

RDC-Mediated Exchange Line-Broadening Provides Evidence for Distinct Jumplike Ring Flips. It has been proposed that aromatic rings in ubiquitin undergo complete ring rotation by continuous diffusion rather than jumplike flips.²⁴ The distinction between jumplike flips and such “continuous diffusion” has not previously been investigated

more directly by liquid-state NMR. Here we address this issue by comparing how the effective value of $\Delta\omega_{\text{RDC}}$ differs between the two scenarios.

We predicted the variation in RDC values as a function of the χ_2 dihedral angle (Figure 4). To estimate $\Delta\omega_{\text{RDC}}$ and

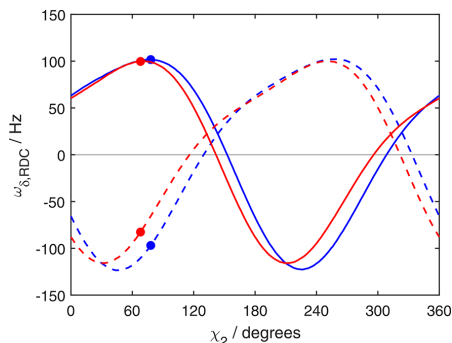


Figure 4. Predicted RDC values as a function of the χ_2 dihedral angle of F52 δ at 5 °C. $\omega_{\delta 1, \text{RDC}}$ and $\omega_{\delta 2, \text{RDC}}$ plotted vs χ_2 as solid and dashed lines, respectively, based on the X-ray structures 1PGB (red) and 2G19 (blue). Ground-state values are indicated as filled dots.

$\langle\omega_{\text{RDC}}\rangle$ values resulting from continuous diffusive motion around χ_2 , we averaged each of the two $\omega_{\delta, \text{RDC}}$ values over a complete 360° rotation by using either a uniform probability distribution (which is rather unphysical) or a probability distribution weighted by the χ_2 dihedral potential of the CHARMM36 force field with the bottom of the potential well set to either the nominal value of $\chi_2 = 90^\circ$ or the actual value measured in the crystal structure, $\chi_2 = 68^\circ$ (1PGB) or $\chi_2 = 78^\circ$ (2G19), before calculating $\Delta\omega_{\text{RDC}}$ and $\langle\omega_{\text{RDC}}\rangle$.

Neither the uniform nor the weighted distribution is expected to accurately portray reality because the probability distribution of ring orientations will surely depend also on tertiary interactions in the protein core. However, the greater the distinguishing features of the probability distribution, the less likely is continuous diffusional rotation. Thus, the two different averaging procedures employed here provide a first reasonable comparison of our experimental results with those expected from the continuous diffusion model. The resulting values of $\Delta\omega_{\text{RDC}}$ and $\langle\omega_{\text{RDC}}\rangle$ are listed in Table 3. As might be expected, the continuous diffusion model yields significantly reduced $\Delta\omega_{\text{RDC}}$ values near zero, quite different from the experimental result of $\Delta\omega_{\text{RDC}} = 90$ Hz. By contrast, the $\Delta\omega_{\text{RDC}}$ value calculated from the ground-state structure shows excellent agreement with the value determined by experiment. In addition, $\langle\omega_{\text{RDC}}\rangle$ is underestimated by the continuous

Table 3. Predicted RDC Values for F52 δ at 5 °C (in Hz), Averaged over a Complete 360° Rotation around χ_2

crystal structure	$\Delta\omega_{\text{RDC}}$		$\langle\omega_{\text{RDC}}\rangle$	
	1PGB	2G19	1PGB	2G19
uniform probability	0.4	0.5	5.3	5.2
weighted probability ^a	0.3	0.4	9.4	6.7
weighted probability ^b	0.3	0.4	6.0	4.8

^aDihedral potential with minimum at $\chi_2 = 90^\circ$. ^bDihedral potential with minimum at $\chi_2 = 68^\circ$ (1PGB) or $\chi_2 = 78^\circ$ (2G19).

diffusion model. Taken together, these results provide strong evidence that the aromatic ring of F52 in GB1 undergoes a distinct, jumplike 180° flip around the χ_2 dihedral angle.

Solid-state NMR spectroscopy can provide powerful information about aromatic ring dynamics because the dipolar coupling strength and asymmetry parameter depend on the underlying motional modes.^{46–49} We note that a previous solid-state NMR study of microcrystalline wild-type GB1 indicated that the F52 ring is nearly rigid in this environment,⁴⁸ which is clearly not the case in solution as demonstrated herein. Thus, the breathing motions that enable the F52 ring to flip are apparently quenched in the crystalline state. These differences highlight the critical role of the protein packing density, where not only the local environment around the ring is important but also more remote interactions such as the protein–protein interface of the crystal.

Structural Aspects of a Ring Flips. We have previously determined the activation parameters of the F52 ring flip, including ΔH^\ddagger and ΔS^\ddagger , as well as the activation volume, ΔV^\ddagger , and the isothermal volume compressibility.¹⁹ These parameters present a consistent picture of the transition state as being significantly expanded with fewer stabilizing interactions than the ground state, while populating a larger number of conformations and having a compressibility similar to that of unfolded proteins, indicating that the F52 ring flip is made possible by relatively large-scale breathing motions that resemble local unfolding.¹⁹ Yet, our present results are fully consistent with a jumplike two-state exchange process that does not involve any intermediate or off-pathway high-energy conformations. This result contrasts with recent observations involving a buried tyrosine residue in an SH3 domain,⁵⁰ which exchanges between the ground state and an alternative high-energy conformation characterized by different values of the χ_2 dihedral angle. MD simulations showed that local breathing motions create a significant void volume ($\Delta V^\ddagger = 65 \text{ \AA}^3$) allowing for rapid ring flips ($k_{\text{flip}} > 25000 \text{ s}^{-1}$). However, once in a while (70 s^{-1}) the ring flip is apparently intercepted by interactions with surrounding residues, leading to recompaction of the local structure and trapping of the ring in the high-energy conformation, which consequently is off-pathway with respect to the ring flip reaction. X-ray crystal structures of variant SH3 domains that stabilize the high-energy state provide unique structural details of large-scale structural changes that might be coupled to ring flipping.⁵⁰

The difference in behavior observed for the aromatic residues in the SH3 domain,⁵⁰ ubiquitin,²⁴ and GB1 illustrates the complexity and variation among proteins in the intramolecular dynamics associated with ring flipping, which evidently is critically dependent on local structure and interactions.

CONCLUSIONS

We have shown that RDC-mediated exchange line broadening enables measurement of aromatic ring flip dynamics using relaxation dispersion experiments. As reported previously for other nuclei,^{29,30} the approach offers a valuable complement to experiments probing exchange mediated by the isotropic chemical shift. In the special case of aromatic side chains, the experimentally determined RDCs provide particularly powerful information about the mechanism of the ring flips by making it possible to distinguish between distinct jumps and alternative models, including continuous diffusive motion around the χ_2 dihedral angle as proposed by Wand and co-workers based on

studies of aromatic residues in ubiquitin.²⁴ We conclude that the aromatic side chain of F52 in GB1 undergoes distinct, jumplike ring flips, in full agreement with our previous conclusions based on temperature- and pressure-dependent studies of the activation volume and transition state compressibility of the exchange process.¹⁹

AUTHOR INFORMATION

Corresponding Author

Ulrich Weinger – *Institute of Physics, Biophysics, Martin-Luther-University Halle-Wittenberg, D-06120 Halle (Saale), Germany*; orcid.org/0000-0003-0841-8332; Phone: +49 345 55 28555; Email: ulrich.weinger@physik.uni-halle.de

Authors

Matthias Dreydoppel – *Institute of Physics, Biophysics, Martin-Luther-University Halle-Wittenberg, D-06120 Halle (Saale), Germany*

Mikael Akke – *Division of Biophysical Chemistry, Center for Molecular Protein Science, Department of Chemistry, Lund University, SE-22100 Lund, Sweden*; orcid.org/0000-0002-2395-825X

Complete contact information is available at:
<https://pubs.acs.org/10.1021/acs.jpcb.2c05097>

Notes

The authors declare no competing financial interest.

ACKNOWLEDGMENTS

This work was supported by Deutsche Forschungsgemeinschaft (WE 5587/1-2), the Swedish Research Council (2018-4995), and the ERASMUS+ programme. This study made use of NMRbox: National Center for Biomolecular NMR Data Processing and Analysis, a Biomedical Technology Research Resource (BTRR), which is supported by NIH Grant P41GM111135 (NIGMS).

REFERENCES

- (1) Wagner, G.; Demarco, A.; Wüthrich, K. Dynamics of Aromatic Amino-Acid Residues in Globular Conformation of Basic Pancreatic Trypsin-Inhibitor (Bpti). I. H-1 Nmr-Studies. *Biophys. Struct. Mech.* **1976**, *2* (2), 139–158.
- (2) Wüthrich, K. The way to NMR structures of proteins. *Nat. Struct. Biol.* **2001**, *8* (11), 923–925.
- (3) Campbell, I. D.; Dobson, C. M.; Williams, R. J. P. Proton Magnetic-Resonance Studies of Tyrosine Residues of Hen Lysozyme-Assignment and Detection of Conformational Mobility. *Proc. Royal Soc. B* **1975**, *189* (1097), 503–509.
- (4) Baturin, S. J.; Okon, M.; McIntosh, L. P. Structure, dynamics, and ionization equilibria of the tyrosine residues in *Bacillus circulans* xylanase. *J. Biomol. NMR* **2011**, *51* (3), 379–394.
- (5) Hattori, M.; Li, H.; Yamada, H.; Akasaka, K.; Hengstenberg, W.; Gronwald, W.; Kalbitzer, H. R. Infrequent cavity-forming fluctuations in HPr from *Staphylococcus carnosus* revealed by pressure- and temperature-dependent tyrosine ring flips. *Protein Sci.* **2004**, *13* (12), 3104–3114.
- (6) Nall, B. T.; Zuniga, E. H. Rates and Energetics of Tyrosine Ring Flips in Yeast Iso-2-Cytochrome-C. *Biochemistry* **1990**, *29* (33), 7576–7584.
- (7) Kasinath, V.; Valentine, K. G.; Wand, A. J. A C-13 Labeling Strategy Reveals a Range of Aromatic Side Chain Motion in Calmodulin. *J. Am. Chem. Soc.* **2013**, *135* (26), 9560–9563.
- (8) Lichtenecker, R. J. Synthesis of aromatic C-13/H-2-alpha-ketoacid precursors to be used in selective phenylalanine and tyrosine

protein labelling. *Organic & Biomolecular Chemistry* **2014**, *12* (38), 7551–7560.

(9) Lichtenecker, R. J.; Weinhaupl, K.; Schmid, W.; Konrat, R. alpha-Ketoacids as precursors for phenylalanine and tyrosine labelling in cell-based protein overexpression. *J. Biomol. NMR* **2013**, *57* (4), 327–331.

(10) Lundström, P.; Teilum, K.; Carstensen, T.; Bezsonova, I.; Wiesner, S.; Hansen, D. F.; Religa, T. L.; Akke, M.; Kay, L. E. Fractional C-13 enrichment of isolated carbons using [1-C-13]- or [2-C-13]-glucose facilitates the accurate measurement of dynamics at backbone C-alpha and side-chain methyl positions in proteins. *J. Biomol. NMR* **2007**, *38* (3), 199–212.

(11) Milbradt, A. G.; Arthanari, H.; Takeuchi, K.; Boeszoeremnyi, A.; Hagn, F.; Wagner, G. Increased resolution of aromatic cross peaks using alternate C-13 labeling and TROSY. *J. Biomol. NMR* **2015**, *62* (3), 291–301.

(12) Teilum, K.; Brath, U.; Lundström, P.; Akke, M. Biosynthetic C-13 labeling of aromatic side chains in proteins for NMR relaxation measurements. *J. Am. Chem. Soc.* **2006**, *128* (8), 2506–2507.

(13) Weinger, U. Site-selective 13C labeling of proteins using erythrose. *J. Biomol. NMR* **2017**, *67* (3), 191–200.

(14) Weinger, U. Optimal Isotope Labeling of Aromatic Amino Acid Side Chains for NMR Studies of Protein Dynamics. *Methods Enzymol* **2019**, *614*, 67–86.

(15) Raum, H. N.; Schorghuber, J.; Dreydoppel, M.; Lichtenecker, R. J.; Weinger, U. Site-selective (1)H/(2)H labeling enables artifact-free (1)H CPMG relaxation dispersion experiments in aromatic side chains. *J. Biomol. NMR* **2019**, *73* (10–11), 633–639.

(16) Weinger, U.; Brath, U.; Modig, K.; Teilum, K.; Akke, M. Off-resonance rotating-frame relaxation dispersion experiment for C-13 in aromatic side chains using L-optimized TROSY-selection. *J. Biomol. NMR* **2014**, *59* (1), 23–29.

(17) Weinger, U.; Respondek, M.; Akke, M. Conformational exchange of aromatic side chains characterized by L-optimized TROSY-selected C-13 CPMG relaxation dispersion. *J. Biomol. NMR* **2012**, *54* (1), 9–14.

(18) Dreydoppel, M.; Lichtenecker, R. J.; Akke, M.; Weinger, U. 1H R1rho relaxation dispersion experiments in aromatic side chains. *J. Biomol. NMR* **2021**, *75*, 383.

(19) Dreydoppel, M.; Dorn, B.; Modig, K.; Akke, M.; Weinger, U. Transition-State Compressibility and Activation Volume of Transient Protein Conformational Fluctuations. *Jacs Au* **2021**, *1* (6), 833–842.

(20) Dreydoppel, M.; Raum, H. N.; Weinger, U. Slow ring flips in aromatic cluster of GB1 studied by aromatic C-13 relaxation dispersion methods. *J. Biomol. NMR* **2020**, *74* (2–3), 183–191.

(21) Weinger, U.; Modig, K.; Akke, M. Ring Flips Revisited: C-13 Relaxation Dispersion Measurements of Aromatic Side Chain Dynamics and Activation Barriers in Basic Pancreatic Trypsin Inhibitor. *Biochemistry* **2014**, *53* (28), 4519–4525.

(22) Weinger, U.; Respondek, M.; Löw, C.; Akke, M. Slow Aromatic Ring Flips Detected Despite Near-Degenerate NMR Frequencies of the Exchanging Nuclei. *J. Phys. Chem. B* **2013**, *117* (31), 9241–9247.

(23) Yang, C. J.; Takeda, M.; Terauchi, T.; Jee, J.; Kainosho, M. Differential Large-Amplitude Breathing Motions in the Interface of FKBP12-Drug Complexes. *Biochemistry* **2015**, *54* (47), 6983–6995.

(24) Kasinath, V.; Fu, Y. N.; Sharp, K. A.; Wand, A. J. A Sharp Thermal Transition of Fast Aromatic-Ring Dynamics in Ubiquitin. *Angew. Chem., Int. Ed.* **2015**, *54* (1), 102–7.

(25) Sathyamoorthy, B.; Singarapu, K. K.; Garcia, A. E.; Szyperski, T. Protein Conformational Space Populated in Solution Probed with Aromatic Residual Dipolar C-13-H-1 Couplings. *ChemBiochem* **2013**, *14* (6), 684–688.

(26) Li, H.; Yamada, H.; Akasaka, K. Effect of pressure on the tertiary structure and dynamics of folded basic pancreatic trypsin inhibitor. *Biophys. J.* **1999**, *77* (5), 2801–2812.

(27) Wagner, G. Activation Volumes for the Rotational Motion of Interior Aromatic Rings in Globular-Proteins Determined by High-

Resolution H-1-Nmr at Variable Pressure. *FEBS Lett.* **1980**, *112* (2), 280–284.

(28) Wagner, G.; Bruhwiler, D.; Wüthrich, K. Reinvestigation of the Aromatic Side-Chains in the Basic Pancreatic Trypsin-Inhibitor by Heteronuclear Two-Dimensional Nuclear-Magnetic-Resonance. *J. Mol. Biol.* **1987**, *196* (1), 227–231.

(29) Igumenova, T. I.; Brath, U.; Akke, M.; Palmer, A. G. Characterization of chemical exchange using residual dipolar coupling. *J. Am. Chem. Soc.* **2007**, *129* (44), 13396.

(30) Vallurupalli, P.; Hansen, D. F.; Stollar, E.; Meirovitch, E.; Kay, L. E. Measurement of bond vector orientations in invisible excited states of proteins. *Proc. Natl. Acad. Sci. U. S. A.* **2007**, *104* (47), 18473–18477.

(31) Tjandra, N.; Bax, A. Direct measurement of distances and angles in biomolecules by NMR in a dilute liquid crystalline medium. *Science* **1997**, *278* (5340), 1111–4.

(32) Lindman, S.; Xue, W. F.; Szczepankiewicz, O.; Bauer, M. C.; Nilsson, H.; Linse, S. Salting the charged surface: pH and salt dependence of protein G B1 stability. *Biophys. J.* **2006**, *90* (8), 2911–21.

(33) Rückert, M.; Otting, G. Alignment of biological macromolecules in novel nonionic liquid crystalline media for NMR experiments. *J. Am. Chem. Soc.* **2000**, *122* (32), 7793–7797.

(34) Meissner, A.; Duus, J. O.; Sorensen, O. W. Spin-state-selective excitation. Application for E.COSY-type measurement of J(HH) coupling constants. *J. Magn. Reson.* **1997**, *128* (1), 92–97.

(35) Sorensen, M. D.; Meissner, A.; Sorensen, O. W. Spin-state-selective coherence transfer via intermediate states of two-spin coherence in IS spin systems: Application to E.COSY-type measurement of J coupling constants. *J. Biomol. NMR* **1997**, *10* (2), 181–186.

(36) Mulder, F. A. A.; de Graaf, R. A.; Kaptein, R.; Boelens, R. An off-resonance rotating frame relaxation experiment for the investigation of macromolecular dynamics using adiabatic rotations. *J. Magn. Reson.* **1998**, *131* (2), 351–357.

(37) Delaglio, F.; Grzesiek, S.; Vuister, G. W.; Zhu, G.; Pfeifer, J.; Bax, A. Nmrpipe - a Multidimensional Spectral Processing System Based on Unix Pipes. *J. Biomol. NMR* **1995**, *6* (3), 277–293.

(38) Ahlner, A.; Carlsson, M.; Jonsson, B. H.; Lundström, P. PINT: a software for integration of peak volumes and extraction of relaxation rates. *J. Biomol. NMR* **2013**, *56* (3), 191–202.

(39) Miloushev, V. Z.; Palmer, A. G. R(1p) relaxation for two-site chemical exchange: General approximations and some exact solutions. *J. Magn. Reson.* **2005**, *177* (2), 221–227.

(40) Press, W. H.; Teukolsky, S. A.; Vetterling, W. T.; Flannery, B. P. *Numerical Recipes in C++: The Art of Scientific Computing*, 2nd ed.; Cambridge University Press: Cambridge, 2002.

(41) Gallagher, T.; Alexander, P.; Bryan, P.; Gilliland, G. L. 2 Crystal-Structures of the B1 Immunoglobulin-Binding Domain of Streptococcal Protein-G and Comparison with Nmr. *Biochemistry* **1994**, *33* (15), 4721–4729.

(42) Franks, W. T.; Wylie, B. J.; Stellfox, S. A.; Rienstra, C. M. Backbone conformational constraints in a microcrystalline U-15N-labeled protein by 3D dipolar-shift solid-state NMR spectroscopy. *J. Am. Chem. Soc.* **2006**, *128* (10), 3154–5.

(43) Valafar, H.; Prestegard, J. H. REDCAT: a residual dipolar coupling analysis tool. *J. Magn. Reson.* **2004**, *167* (2), 228–241.

(44) Maciejewski, M. W.; Schuyler, A. D.; Gryk, M. R.; Moraru, I. I.; Romero, P. R.; Ulrich, E. L.; Eghbalian, H. R.; Livny, M.; Delaglio, F.; Hoch, J. C. NMRbox: A Resource for Biomolecular NMR Computation. *Biophys. J.* **2017**, *112* (8), 1529–1534.

(45) Raum, H. N.; Dreydoppel, M.; Weininger, U. Conformational exchange of aromatic side chains by (1)H CPMG relaxation dispersion. *J. Biomol. NMR* **2018**, *72* (1–2), 105–114.

(46) Rice, D. M.; Wittebort, R. J.; Griffin, R. G.; Meirovitch, E.; Stimson, E. R.; Meinwald, Y. C.; Freed, J. H.; Scheraga, H. A. Rotational Jumps of the Tyrosine Side-Chain in Crystalline Enkephalin - H-2 Nmr Line-Shapes for Aromatic Ring Motion in Solids. *J. Am. Chem. Soc.* **1981**, *103* (26), 7707–7710.

(47) Gauto, D. F.; Macek, P.; Barducci, A.; Fraga, H.; Hessel, A.; Terauchi, T.; Gajan, D.; Miyanoiri, Y.; Boisbouvier, J.; Lichteneker, R.; Kainosho, M.; Schanda, P. Aromatic Ring Dynamics, Thermal Activation, and Transient Conformations of a 468 kDa Enzyme by Specific H-1-C-13 Labeling and Fast Magic-Angle Spinning NMR. *J. Am. Chem. Soc.* **2019**, *141* (28), 11183–11195.

(48) Paluch, P.; Pawlak, T.; Jeziorna, A.; Trebosc, J.; Hou, G. J.; Vega, A. J.; Amoureux, J. P.; Dracinsky, M.; Polenova, T.; Potrzebowski, M. J. Analysis of local molecular motions of aromatic sidechains in proteins by 2D and 3D fast MAS NMR spectroscopy and quantum mechanical calculations. *Phys. Chem. Chem. Phys.* **2015**, *17* (43), 28789–28801.

(49) Vugmeyster, L.; Ostrovsky, D.; Villafranca, T.; Sharp, J.; Xu, W.; Lipton, A. S.; Hoatson, G. L.; Vold, R. L. Dynamics of Hydrophobic Core Phenylalanine Residues Probed by Solid-State Deuteron NMR. *J. Phys. Chem. B* **2015**, *119* (47), 14892–904.

(50) Marino Perez, L.; Ielasi, F. S.; Bessa, L. M.; Maurin, D.; Kragelj, J.; Blackledge, M.; Salvi, N.; Bouvignies, G.; Palencia, A.; Jensen, M. R. Visualizing protein breathing motions associated with aromatic ring flipping. *Nature* **2022**, *602* (7898), 695–700.

Recommended by ACS

Millisecond Time-Resolved Solid-State NMR Initiated by Rapid Inverse Temperature Jumps

C. Blake Wilson and Robert Tycko

MAY 26, 2022

JOURNAL OF THE AMERICAN CHEMICAL SOCIETY

READ 

Approaching Protein Aggregation and Structural Dynamics by Equilibrium and Nonequilibrium Paramagnetic Perturbation

Yamanappa Hunashal, Gennaro Esposito, et al.

JULY 25, 2022

ANALYTICAL CHEMISTRY

READ 

Protein Electrostatics Investigated through Paramagnetic NMR for Nonpolar Groups

Binhan Yu, Junji Iwahara, et al.

MARCH 10, 2022

THE JOURNAL OF PHYSICAL CHEMISTRY B

READ 

High-Resolution Hydrogen–Deuterium Protection Factors from Sparse Mass Spectrometry Data Validated by Nuclear Magnetic Resonance Measurements

Michele Stofella, Emanuele Paci, et al.

APRIL 06, 2022

JOURNAL OF THE AMERICAN SOCIETY FOR MASS SPECTROMETRY

READ 

Get More Suggestions >

Chapter 5

Summary

Extensive temperature and pressure dependent NMR studies on the ring flip dynamics of the small globular protein GB1 revealed interesting key features of protein conformational fluctuations. Established NMR experimental advancements, new findings about GB1 and aromatic ring dynamics, as well as unprecedented conclusions that could be drawn concerning the associated protein volume fluctuations shall be summarized here.

We introduced a novel ^1H $R_{1\rho}$ relaxation experiment for aromatic side chains that allows for the study of faster exchange processes than with previous ^1H and ^{13}C CPMG or ^{13}C $R_{1\rho}$ approaches.^{61,91} The inaccessibility of aromatic nuclei with vanishing ^{13}C chemical shift differences was overcome and it was shown that appropriate labeling schemes enable artifact-free measurements. Thereby more aromatic nuclei and an enhanced range of exchange rates are accessible for NMR measurements on protein exchange processes like aromatic ring flips. Furthermore, we have shown that RDCs can be used for the detection of exchange processes of aromatic rings. By making use of RDC-mediated exchange line broadening, ring flip rates could be measured with relaxation dispersion experiments on nuclei with zero chemical shift difference. At the same time beneficial structural information on the ring flip mechanism can be gained as will be referred to below.

With the presented studies, the small globular protein GB1 was established as a convenient model system for the study of aromatic ring flips. It can now be considered the best studied system in terms of ring flips next to BPTI. In contrast to the latter, GB1 displays diverse structural and nuclear properties of the aromatic side chains, such as aromatic-aromatic stacking interactions and differing chemical shift differences. These can be exploited for the purpose of exchange rate measurements under

different thermodynamic conditions as well as for methodological development. In addition ring flip kinetics in GB1 are significantly faster than in BPTI. The ring flip rates were measured by use of state-of-the-art NMR relaxation dispersion experiments outside the slow exchange regime. This means we became independent of slow exchange conditions previously required for other systems. Since these slow exchange regime conditions are relatively rare in the favourable temperatures in which proteins exist, we generally expanded the amount of protein systems in which ring flips can be studied.

We have realized the first thermodynamic characterization of rings involved in an aromatic cluster. No correlation of the enthalpy, entropy and volume of activation to the stacking interactions or the extent of immersion of the rings could be detected. The activation parameters are similar to those measured in other proteins, indicating common fluctuation mechanisms for the respective hydrophobic environments. All values are positive in consistence with the established perception of aromatic ring flips to be associated with a compact, ordered ground state. Ring flip rates are similar except for the central ring which exhibits higher rates, pointing to a possible connection between the flip processes.

For the first time we determined the volume compressibility of activation of ring flips, thus providing a unique experimental report on the protein component compressibility of the hydrophobic core. From the positive value of the compressibility difference we learn that the transition state exhibits liquid-like properties, while the ground state is solid-like as was shown by computational studies.¹⁵⁸ A higher flexibility of the transition state implies relatively high mobility of the neighbouring side chains in the hydrophobic core during the transition. Given the distinctive molecular structure the process is hence accompanied by transient local unfolding.

We found that ring flips can occur with zero activation volume and thus without net average expansion of the protein structure. Ring flips are apparently associated with two fluctuation mechanisms: On the one hand required local expansions are always provided by compaction of remote interatomic voids, and additionally a positive activation volume of the protein is enabled when possible under a given pressure. The significance of the activation volume could consequently be specified. Instead of displaying the minimum expansion needed for a ring flip, it gives the average volume increase leading to a flip at a given temperature and pressure.

Using RDC-mediated exchange of aromatic side chains, we could give proof that the exchange mechanism of the monitored ring is a distinct, jumplike flip. Continuous diffusive ring rotation can thus be ruled out, and consequently a vanishing activation volume is no indication for any such diffusive motion even if the associated protein breathing motion is negligible at high pressures. The corresponding structural fluctuations are under these conditions to a lesser degree observable as the acquainted breathing motions, but apparently get confined to fluctuations transmitted within the protein structure.

Outlook

The energetics of a protein fluctuation process could be characterized to a novel extent, yet it remains difficult to describe the structure of the transition state itself. From the present studies it can not be inferred how the side chains around an aromatic ring change their orientations and rotamer states during a ring flip. Characterization of structural motions associated with ring flip processes could recently be achieved in only one protein in an indirect way.¹²⁹ Sufficiently long molecular dynamics simulations are in principal also capable to track the course of events during the transition process, which may be elucidated in the future.

As a result of the experimental improvements introduced here, characterization of ring flips in other protein systems can be conducted to generalize the findings. With the range of accessible exchange rates being expanded, and the NMR experiments being extended to nuclei with zero chemical shift difference, it is possible and beneficial to study many more systems where ring flips take place.

Examining the possible correlation between flipping rings involved in stacking interactions would provide valuable information about the dynamics of proteins. The transition-state compressibility of aromatic rings can now be determined as a valuable parameter for the characterization of conformational fluctuations, and it should be pursued if particular differences exist between rings in different proteins or within the structure of one system.

The presented data encourages to progress in the examination of protein fluctuations associated with aromatic ring flips and to clarify the relationship to other important conformational changes such as those related to unfolding or binding. By means of site-specific isotope labeling also catalytically active and medically significant proteins are amenable to the investigation of side chain relaxation properties. NMR and computational methods have opened up new perspectives on the fascinating mechanisms of protein flexibility.

References

- [1] R. P. Feynman, R. B. Leighton, and M. Sands. *The Feynman Lectures on Physics* - online edition, 1963-1965, 2006, 2013, accessed 20 September 2022. URL <https://www.feynmanlectures.caltech.edu/>.
- [2] A. Sekhar and L. E. Kay. An NMR view of protein dynamics in health and disease. *Annu. Rev. Biophys.*, 48:297–319, 2019.
- [3] M. Williamson. *How Proteins Work*. Garland Science, New York, 2011.
- [4] F. G. Parak. Proteins in action: The physics of structural fluctuations and conformational changes. *Curr. Opin. Struct. Biol.*, 13:552–557, 2003.
- [5] A. K. Mittermaier and L. E. Kay. New tools provide new insights in NMR studies of protein dynamics. *Science*, 312:224–228, 2006.
- [6] P. Śledź and A. Caflisch. Protein structure-based drug design: From docking to molecular dynamics. *Curr. Opin. Struct. Biol.*, 48:93–102, 2018.
- [7] A. Sekhar and L. E. Kay. NMR paves the way for atomic level descriptions of sparsely populated, transiently formed biomolecular conformers. *Proc. Natl. Acad. Sci. USA*, 110:12867–12874, 2013.
- [8] K. Wüthrich and G. Wagner. NMR investigations of the dynamics of the aromatic amino acid residues in the basic pancreatic trypsin inhibitor. *FEBS Lett.*, 50:265–268, 1975.
- [9] I. D. Campbell, C. M. Dobson, and R. J. Williams. Proton magnetic resonance studies of the tyrosine residues of hen lysozyme-assignment and detection of conformational mobility. *Proc. R. Soc. B.*, 189:503–509, 1975.
- [10] A. G. Palmer. NMR characterization of the dynamics of biomacromolecules. *Chem. Rev.*, 104:3623–3640, 2004.

- [11] T. I. Igumenova and A. G. Palmer. Off-resonance TROSY-selected $R_{1\rho}$ experiment with improved sensitivity for medium- and high-molecular-weight proteins. *J. Am. Chem. Soc.*, 128:8110–8111, 2006.
- [12] M. Kovermann, P. Rogne, and M. Wolf-Watz. Protein dynamics and function from solution state NMR spectroscopy. *Q. Rev. Biophys.*, 49:e6, 2016.
- [13] A. G. Palmer and H. Koss. Chemical exchange. *Methods Enzymol.*, 615:177–236, 2019.
- [14] A. G. Palmer and F. Massi. Characterization of the dynamics of biomacromolecules using rotating-frame spin relaxation NMR spectroscopy. *Chem. Rev.*, 106:1700–1719, 2006.
- [15] A. K. Mittermaier and L. E. Kay. Observing biological dynamics at atomic resolution using NMR. *Trends Biochem. Sci.*, 34:601–611, 2009.
- [16] M. Karplus and J. Kuriyan. Molecular dynamics and protein function. *Proc. Natl. Acad. Sci. USA*, 102:6679–85, 2005.
- [17] C. N. Pace, J. M. Scholtz, and G. R. Grimsley. Forces stabilizing proteins. *FEBS Lett.*, 588:2177–2184, 2014.
- [18] M. F. Perutz. The role of aromatic rings as hydrogen-bond acceptors in molecular recognition. *Philos. Trans. R. Soc. A*, 345:105–112, 1993.
- [19] C. C. Valley, A. Cembran, J. D. Perlmutter, A. K. Lewis, N. P. Labello, J. Gao, and J. N. Sachs. The methionine-aromatic motif plays a unique role in stabilizing protein structure. *J. Biol. Chem.*, 287:34979–34991, 2012.
- [20] K. B. Wong and V. Daggett. Barstar has a highly dynamic hydrophobic core: Evidence from molecular dynamics simulations and nuclear magnetic resonance relaxation data. *Biochemistry*, 37:11182–11192, 1998.
- [21] A. A. Bogan and K. S. Thorn. Anatomy of hot spots in protein interfaces. *J. Mol. Biol.*, 280:1–9, 1998.
- [22] L. Lo Conte, C. Chothia, and J. Janin. The atomic structure of protein-protein recognition sites. *J. Mol. Biol.*, 285:2177–2198, 1999.
- [23] D. Rajamani, S. Thiel, S. Vajda, and C. J. Camacho. Anchor residues in protein-protein interactions. *Proc. Natl. Acad. Sci. USA*, 101:11287–11292, 2004.
- [24] M. Rooman, J. Liévin, E. Buisine, and R. Wintjens. Cation- π /H-bond stair motifs at protein-DNA interfaces. *J. Mol. Biol.*, 319:67–76, 2002.

- [25] D. Lacabanne, J. Boudet, A. A. Malär, P. Wu, R. Cadalbert, L. Salmon, F. H. Allain, B. H. Meier, and T. Wiegand. Protein side-chain-DNA contacts probed by fast magic-angle spinning NMR. *J. Phys. Chem. B*, 124:11089–11097, 2020.
- [26] D. Barak, A. Ordentlich, Y. Segall, B. Velan, H. P. Benschop, L. P. De Jong, and A. Shafferman. Carbocation-mediated processes in biocatalysts. Contribution of aromatic moieties. *J. Am. Chem. Soc.*, 119:3157–3158, 1997.
- [27] G. J. Bartlett, C. T. Porter, N. Borkakoti, and J. M. Thornton. Analysis of catalytic residues in enzyme active sites. *J. Mol. Biol.*, 324:105–121, 2002.
- [28] G. Hu, P. D. Gershon, A. E. Hodel, and F. A. Quijcho. mRNA cap recognition: Dominant role of enhanced stacking interactions between methylated bases and protein aromatic side chains. *Proc. Natl. Acad. Sci. USA*, 96:7149–7154, 1999.
- [29] S. Birtalan, R. D. Fisher, and S. S. Sidhu. The functional capacity of the natural amino acids for molecular recognition. *Mol. BioSyst.*, 6:1186–1194, 2010.
- [30] D. L. Beene, G. S. Brandt, W. Zhong, N. M. Zacharias, H. A. Lester, and D. A. Dougherty. Cation- π interactions in ligand recognition by serotonergic (5-HT_{3A}) and nicotinic acetylcholine receptors: The anomalous binding properties of nicotine. *Biochemistry*, 41:10262–10269, 2002.
- [31] B. Pan, D. Liu, L. Yang, and K. Wüthrich. GPCR large-amplitude dynamics by ¹⁹F-NMR of a prepeptide bound to the neurokinin 1 receptor. *Proc. Natl. Acad. Sci. USA*, 119:e2122682119, 2022.
- [32] T. Fecker, P. Galaz-Davison, F. Engelberger, Y. Narui, M. Sotomayor, L. P. Parra, and C. A. Ramírez-Sarmiento. Active site flexibility as a hallmark for efficient PET degradation by *I. sakaiensis* PETase. *Biophys. J.*, 114:1302–1312, 2018.
- [33] LLC Schrödinger. The PyMOL molecular graphics system, version 2.0, 2022. URL <https://www.pymol.org/pymol.html>.
- [34] T. Gallagher, P. Alexander, P. Bryan, and G. L. Gilliland. Two crystal structures of the B1 immunoglobulin-binding domain of streptococcal protein G and comparison with NMR. *Biochemistry*, 33:4721–4729, 1994.
- [35] L. Björck and G. Kronvall. Purification and some properties of streptococcal protein G, a novel IgG-binding reagent. *J. Immunol.*, 133:969–974, 1984.
- [36] A. M. Gronenborn, D. R. Filpula, N. Z. Essig, A. Achari, M. Whitlow, P. T. Wingfield, and M. G. Clore. A novel, highly stable fold of the immunoglobulin binding domain of streptococcal protein G. *Science*, 253:657–661, 1991.

- [37] P. Alexander, J. Orban, and P. Bryan. Kinetic analysis of folding and unfolding the 56 amino acid IgG-binding domain of streptococcal protein G. *Biochemistry*, 31:7243–7248, 1992.
- [38] Y. Cao, C. Lam, M. Wang, and H. Li. Nonmechanical protein can have significant mechanical stability. *Angew. Chem. Int. Ed.*, 45:642–645, 2006.
- [39] D. J. Wilton, R. B. Tunnicliffe, Y. O. Kamatari, K. Akasaka, and M. P. Williamson. Pressure-induced changes in the solution structure of the GB1 domain of protein G. *Proteins: Struct., Funct., Bioinf.*, 71:1432–1440, 2008.
- [40] M. Dreydoppel, P. Becker, H. N. Raum, S. Gröger, J. Balbach, and U. Weininger. Equilibrium and kinetic unfolding of GB1: Stabilization of the native state by pressure. *J. Phys. Chem. B*, 122:8846–8852, 2018.
- [41] S. Lindman, W. F. Xue, O. Szczepankiewicz, M. C. Bauer, H. Nilsson, and S. Linse. Salting the charged surface: pH and salt dependence of protein G B1 stability. *Biophys. J.*, 90:2911–2921, 2006.
- [42] J. H. Tomlinson, V. L. Green, P. J. Baker, and M. P. Williamson. Structural origins of pH-dependent chemical shifts in the B1 domain of protein G. *Proteins*, 78:3000–3016, 2010.
- [43] K. Ding, J. M. Louis, and A. M. Gronenborn. Insights into conformation and dynamics of protein GB1 during folding and unfolding by NMR. *J. Mol. Biol.*, 335:2004, 1299–1307.
- [44] J. Wallerstein, U. Weininger, M. A. Khan, S. Linse, and M. Akke. Site-specific protonation kinetics of acidic side chains in proteins determined by pH-dependent carboxyl ¹³C NMR relaxation. *J. Am. Chem. Soc.*, 137:3093–3101, 2015.
- [45] A. Bille, K. S. Jensen, S. Mohanty, M. Akke, and A. Irbäck. Stability and local unfolding of SOD1 in the presence of protein crowders. *J. Phys. Chem. B*, 123:1920–1930, 2019.
- [46] T. Bu, Wang, H. E., and H. Li. Single molecule force spectroscopy reveals critical roles of hydrophobic core packing in determining the mechanical stability of protein GB1. *Langmuir*, 28:12319–12325, 2012.
- [47] E. M. Purcell, H. C. Torrey, and R. V. Pound. Resonance absorption by nuclear magnetic moments in a solid. *Phys. Rev.*, 69:37–38, 1946.
- [48] F. Bloch, W. W. Hansen, and M. Packard. The nuclear induction experiment. *Phys. Rev.*, 70(7-8):474–485, 1946.

- [49] M. H. Levitt. *Spin Dynamics: Basics of Nuclear Magnetic Resonance*. John Wiley & Sons, Ltd., 2nd edition, 2015.
- [50] J. Cavanagh, W. J. Fairbrother, A. G. Palmer, M. Rance, and N. J. Skelton. *Protein NMR Spectroscopy: Principles and Practice*. Elsevier Inc., 2nd edition, 2007.
- [51] F. J. M. van de Ven. *Multidimensional NMR in Liquids: Basic Principles and Experimental Methods*. VCH Publishers, Inc., 1995.
- [52] F. Bloch. Nuclear induction. *Phys. Rev.*, 70(7-8):460–474, 1946.
- [53] O. W. Sørensen, G. W. Eich, M. H. Levitt, G. Bodenhausen, and R. R. Ernst. Product operator formalism for the description of NMR pulse experiments. *Prog. NMR Spectrosc.*, 16:163–192, 1984.
- [54] A. C. de Dios, J. G. Pearson, and E. Oldfield. Secondary and tertiary structural effects on protein NMR chemical shifts: An ab initio approach. *Science*, 260:1491–1496, 1993.
- [55] D. S. Wishart and D. A. Case. Use of chemical shifts in macromolecular structure determination. *Methods Enzymol.*, 338:3–34, 2002.
- [56] A. Bax and A. Grishaev. Weak alignment NMR: A hawk-eyed view of biomolecular structure. *Curr. Opin. Struct. Biol.*, 15:563–570, 2005.
- [57] E. Brunner. Residual dipolar couplings in protein NMR. *Concepts Magn. Reson.*, 13(4):238–259, 2001.
- [58] H. M. McConnell. Reaction rates by nuclear magnetic resonance. *J. Chem. Phys.*, 28(3):430–431, 1958.
- [59] H. Koss, M. Rance, and A. G. Palmer. General expressions for $R_{1\rho}$ relaxation for N -site chemical exchange and the special case of linear chains. *J. Magn. Reson.*, 274:36–45, 2017.
- [60] A. G. Palmer, C. D. Kroenke, and J. P. Loria. Nuclear magnetic resonance methods for quantifying microsecond-to-millisecond motions in biological macromolecules. *Methods Enzymol.*, 339:204–238, 2001.
- [61] C. Charlier, S. F. Cousin, and F. Ferrage. Protein dynamics from nuclear magnetic relaxation. *Chem. Soc. Rev.*, 45:2410–2422, 2016.
- [62] C. Deverell, R.E. Morgan, and J.H. Strange. Studies of chemical exchange by nuclear magnetic relaxation in the rotating frame. *Mol. Phys.*, 18(4):553–559, 1970.

- [63] V. Z. Miloushev and A. G. Palmer. $R_{1\rho}$ relaxation for two-site exchange: General approximations and some exact solutions. *J. Magn. Reson.*, 177:221–227, 2005.
- [64] D. Abergel and A. G. Palmer. On the use of the stochastic Liouville equation in NMR: Application to $R_{1\rho}$ relaxation in the presence of exchange. *Concepts Magn. Reson. A*, 19(2):134–148, 2003.
- [65] H. Wennerström. Nuclear magnetic relaxation induced by chemical exchange. *Mol. Phys.*, 24(1):69–80, 1972.
- [66] D. G. Davis, M. E. Perlman, and R. E. London. Direct measurements of the dissociation-rate constant for inhibitor-enzyme complexes via the $T_{1\rho}$ and T_2 (CPMG) methods. *J. Magn. Reson. Ser. B*, 104:266–275, 1994.
- [67] O. Trott and A. G. Palmer. $R_{1\rho}$ relaxation outside of the fast-exchange limit. *J. Magn. Reson.*, 154:157–160, 2002.
- [68] H. Desvaux and P. Berthault. Study of dynamic processes in liquids using off-resonance rf irradiation. *Prog. NMR Spectrosc.*, 35:295–340, 1999.
- [69] U. Weininger, U. Brath, K. Modig, K. Teilum, and M. Akke. Off-resonance rotating-frame relaxation dispersion experiment for ^{13}C in aromatic side chains using L-optimized TROSY-selection. *J. Biomol. NMR*, 59:23–29, 2014.
- [70] U. Weininger. Optimal isotope labeling of aromatic amino acid side chains for NMR studies of protein dynamics. *Methods Enzymol.*, 614:67–86, 2019.
- [71] H. Geen and R. Freeman. Band-selective radiofrequency pulses. *J. Magn. Reson.*, 93:93–141, 1991.
- [72] F. A. Mulder, R. A. de Graaf, R. Kaptein, and R. Boelens. An off-resonance rotating frame relaxation experiment for the investigation of macromolecular dynamics using adiabatic rotations. *J. Magn. Reson.*, 131:351–357, 1998.
- [73] A. J. Shaka, P. B. Barker, and R. Freeman. Computer-optimized decoupling scheme for wideband applications and low-level operation. *J. Magn. Reson.*, 64:547–552, 1985.
- [74] K. Pervushin, B. Vögeli, and A. Eletsy. Longitudinal ^1H relaxation optimization in TROSY NMR spectroscopy. *J. Am. Chem. Soc.*, 124(43):12898–12902, 2002.
- [75] U. Weininger, C. Diehl, and M. Akke. ^{13}C relaxation experiments for aromatic side chains employing longitudinal- and transverse-relaxation optimized NMR spectroscopy. *J. Biomol. NMR*, 53:181–190, 2012.

- [76] S. Grzesiek and A. Bax. The importance of not saturating H₂O in protein NMR. Application to sensitivity enhancement and NOE measurements. *J. Am. Chem. Soc.*, 115:12593–12594, 1993.
- [77] K. Pervushin, R. Riek, G. Wider, and K. Wüthrich. Attenuated T_2 relaxation by mutual cancellation of dipole–dipole coupling and chemical shift anisotropy indicates an avenue to NMR structures of very large biological macromolecules in solution. *Proc. Natl. Acad. Sci. USA*, 94:12366–12371, 1997.
- [78] W. S. Veeman. Carbon-13 chemical shift anisotropy. *Prog. NMR Spectrosc.*, 16:193–235, 1984.
- [79] J. P. Loria, M. Rance, and A. G. Palmer. A TROSY CPMG sequence for characterizing chemical exchange in large proteins. *J. Biomol. NMR*, 15:151–155, 1999.
- [80] A. Meissner, J. Ø. Duus, and O. W. Sørensen. Spin-state-selective excitation. Application for E.COSY-type measurement of J_{HH} coupling constants. *J. Magn. Reson.*, 128:92–97, 1997.
- [81] M. Akke and A. G. Palmer. Monitoring macromolecular motions on microsecond to millisecond time scales by $R_{1\rho}$ - R_1 constant relaxation time NMR spectroscopy. *J. Am. Chem. Soc.*, 118:911–912, 1996.
- [82] D. F. Hansen and L. E. Kay. Improved magnetization alignment schemes for spin-lock relaxation experiments. *J. Biomol. NMR*, 37:245–255, 2007.
- [83] C. D. Kroenke, J. P. Loria, L. K. Lee, M. Rance, and A. G. Palmer. Longitudinal and transverse ^1H - ^{15}N dipolar/ ^{15}N chemical shift anisotropy relaxation interference: Unambiguous determination of rotational diffusion tensors and chemical exchange effects in biological macromolecules. *J. Am. Chem. Soc.*, 120:7905–7915, 1998.
- [84] M. D. Sørensen, A. Meissner, and O. W. Sørensen. Spin-state-selective coherence transfer via intermediate states of two-spin coherence in is spin systems: Application to E.COSY-type measurement of J coupling constants. *J. Biomol. NMR*, 10:181–186, 1997.
- [85] D. M. Korzhnev, N. S. Skrynnikov, O. Millet, D. A. Torchia, and L. E. Kay. An NMR experiment for the accurate measurement of heteronuclear spin-lock relaxation rates. *J. Am. Chem. Soc.*, 124:10743–10753, 2002.
- [86] F. Massi, E. Johnson, C. Wang, M. Rance, and A. G. Palmer. NMR $R_{1\rho}$ rotating-frame relaxation with weak radio frequency fields. *J. Am. Chem. Soc.*, 126:2247–2256, 2004.

- [87] I. R. Kleckner and M. P. Foster. An introduction to NMR-based approaches for measuring protein dynamics. *Biochim. Biophys. Acta*, 1814:942–968, 2011.
- [88] D. M. Korzhnev, V. Y. Orekhov, and L. E. Kay. Off-resonance $R_{1\rho}$ NMR studies of exchange dynamics in proteins with low spin-lock fields: An application to a Fyn SH3 domain. *J. Am. Chem. Soc.*, 127:713–721, 2005.
- [89] R. Ishima, J. Baber, J. M. Louis, and D. A. Torchia. Carbonyl carbon transverse relaxation dispersion measurements and ms- μ s timescale motion in a protein hydrogen bond network. *J. Biomol. NMR*, 29:187–198, 2004.
- [90] F. A. Mulder and M. Akke. Carbonyl ^{13}C transverse relaxation measurements to sample protein backbone dynamics. *Magn. Reson. Chem.*, 41:853–865, 2003.
- [91] H. N. Raum, M. Dreydoppel, and U. Weininger. Conformational exchange of aromatic side chains by ^1H CPMG relaxation dispersion. *J. Biomol. NMR*, 72: 105–114, 2018.
- [92] U. Brath, M. Akke, D. Yang, L. E. Kay, and F. A. Mulder. Functional dynamics of human FKBP12 revealed by methyl ^{13}C rotating frame relaxation dispersion NMR spectroscopy. *J. Am. Chem. Soc.*, 128:5718–5727, 2006.
- [93] P. Lundström and M. Akke. Microsecond protein dynamics measured by $^{13}\text{C}^\alpha$ rotating-frame spin relaxation. *ChemBioChem*, 6:1685–1692, 2005.
- [94] K. Teilum, U. Brath, P. Lundström, and M. Akke. Biosynthetic ^{13}C labeling of aromatic side chains in proteins for NMR relaxation measurements. *J. Am. Chem. Soc.*, 128:2506–2507, 2006.
- [95] P. Lundström, K. Teilum, T. Carstensen, I. Bezsonova, S. Wiesner, D. F. Hansen, T. L. Religa, M. Akke, and L. E. Kay. Fractional ^{13}C enrichment of isolated carbons using $[1-^{13}\text{C}]$ - or $[2-^{13}\text{C}]$ -glucose facilitates the accurate measurement of dynamics at backbone C^α and side-chain methyl positions in proteins. *J. Biomol. NMR*, 38:199–212, 2007.
- [96] A. Eletsky, H. S. Atreya, G. Liu, and T. Szyperski. Probing structure and functional dynamics of (large) proteins with aromatic rings: L-GFT-TROSY (4,3)D HCCH NMR spectroscopy. *J. Am. Chem. Soc.*, 127(42):14578–14579, 2005.
- [97] R. Ishima and D. A. Torchia. Estimating the time scale of chemical exchange of proteins from measurements of transverse relaxation rates in solution. *J. Biomol. NMR*, 14:369–372, 1999.
- [98] J. G. Reddy, S. Pratihar, D. Ban, S. Frischkorn, S. Becker, C. Griesinger, and D. Lee. Simultaneous determination of fast and slow dynamics in molecules

- using extreme CPMG relaxation dispersion experiments. *J. Biomol. NMR*, 70: 1–9, 2018.
- [99] A. J. Shaka and J. Keeler. Broadband spin decoupling in isotropic-liquids. *Prog. NMR Spectrosc.*, 19:47–129, 1987.
- [100] A. Cooper. Thermodynamic fluctuations in protein molecules. *Proc. Natl. Acad. Sci. USA*, 73:2740–2741, 1976.
- [101] G. Wagner, A. Demarco, and K. Wüthrich. Dynamics of aromatic amino-acid residues in globular conformation of basic pancreatic trypsin-inhibitor (BPTI). I. ^1H NMR studies. *Biophys. Struct. Mech.*, 2:139–158, 1976.
- [102] W. E. Hull and B. D. Sykes. Fluorotyrosine alkaline phosphatase: Internal mobility of individual tyrosines and the role of chemical shift anisotropy as a ^{19}F nuclear spin relaxation mechanism in proteins. *J. Mol. Biol.*, 98:121–153, 98.
- [103] E. A. Meyer, R. K. Castellano, and F. Diederich. Interactions with aromatic rings in chemical and biological recognition. *Angew. Chem. Int. Ed.*, 42:1210–1250, 2003.
- [104] J. P. Gallivan and D. A. Dougherty. Cation- π interactions in structural biology. *Proc. Natl. Acad. Sci. USA*, 96:9459–9464, 1999.
- [105] A. S. Mahadevi and G. N. Sastry. Cation- π interaction: Its role and relevance in chemistry, biology, and material science. *Chem. Rev.*, 113:2100–2138, 2013.
- [106] M. Brandl, M. S. Weiss, A. Jabs, J. Sühnel, and R. Hilgenfeld. C–H... π -interactions in proteins. *J. Mol. Biol.*, 307:357–377, 2001.
- [107] C. A. Hunter, K. R. Lawson, J. Perkins, and C. J. Urch. Aromatic interactions. *J. Chem. Soc., Perkin Trans.*, 2:651–669, 2001.
- [108] S. K. Burley and G. A. Petsko. Aromatic-aromatic interaction: A mechanism of protein structure stabilization. *Science*, 229:23–28, 1985.
- [109] S. Tsuzuki, K. Honda, T. Uchimaru, M. Mikami, and K. Tanabe. Origin of attraction and directionality of the π/π interaction: Model chemistry calculations of benzene dimer interaction. *J. Am. Chem. Soc.*, 124:104–112, 2002.
- [110] C. A. Hunter and J. K. Sanders. The nature of π - π interactions. *J. Am. Chem. Soc.*, 112:5525–5534, 1990.
- [111] G. B. McGaughey, M. Gagné, and A. K. Rappé. π -stacking interactions: Alive and well in proteins. *J. Biol. Chem.*, 273:15458–15463, 1998.

- [112] RCSB Protein Data Bank. Phenylalanine, accessed 07 July 2022. URL <https://www.rcsb.org/ligand/PHE>.
- [113] IUPAC-IUB Joint Commission on Biochemical Nomenclature (JCBN). Nomenclature and symbolism for amino acids and peptides. *Pure Appl. Chem.*, 56:595–624, 1984.
- [114] RCSB Protein Data Bank. Tyrosine, accessed 07 July 2022. URL <https://www.rcsb.org/ligand/TYR>.
- [115] U. Weininger, M. Respondek, C. Löw, and M. Akke. Slow aromatic ring flips detected despite near-degenerate NMR frequencies of the exchanging nuclei. *J. Phys. Chem. B*, 117:9241–9247, 2013.
- [116] M. Hattori, H. Li, H. Yamada, K. Akasaka, W. Hengstenberg, W. Gronwald, and H. R. Kalbitzer. Infrequent cavity-forming fluctuations in HPr from *Staphylococcus carnosus* revealed by pressure- and temperature-dependent tyrosine ring flips. *Protein Sci.*, 13:3104–3114, 2004.
- [117] G. Wagner and K. Wüthrich. Dynamic model of globular protein conformations based on NMR studies in solution. *Nature*, 275:247–248, 1978.
- [118] V. Kasinath, K. G. Valentine, and A. J. Wand. A ^{13}C labeling strategy reveals a range of aromatic side chain motion in calmodulin. *J. Am. Chem. Soc.*, 135:9560–9563, 2013.
- [119] I. D. Campbell, C. M. Dobson, G. R. Moore, S. J. Perkins, and R. J. Williams. Temperature-dependent molecular-motion of a tyrosine residue of ferrocyanochrome c. *FEBS Lett.*, 70:96–100, 1976.
- [120] D. K. Rao and A. K. Bhuyan. Complexity of aromatic ring-flip motions in proteins: Y97 ring dynamics in cytochrome c observed by cross-relaxation suppressed exchange NMR spectroscopy. *J. Biomol. NMR*, 39:187–196, 2007.
- [121] G. Wagner, D. Brühwiler, and K. Wüthrich. Reinvestigation of the aromatic side-chains in the basic pancreatic trypsin inhibitor by heteronuclear two-dimensional nuclear magnetic resonance. *J. Mol. Biol.*, 196:227–231, 1987.
- [122] J. J. Skalicky, J. L. Mills, S. Sharma, and T. Szyperski. Aromatic ring-flipping in supercooled water: Implications for NMR-based structural biology of proteins. *J. Am. Chem. Soc.*, 123:388–397, 2001.
- [123] B. Sathyamoorthy, K. K. Singarapu, A. E. Garcia, and T. Szyperski. Protein conformational space populated in solution probed with aromatic residual dipolar ^{13}C - ^1H couplings. *ChemBioChem*, 14:684–688, 2013.

- [I24] U. Weininger, K. Modig, and M. Akke. Ring flips revisited: ^{13}C relaxation dispersion measurements of aromatic side chain dynamics and activation barriers in basic pancreatic trypsin inhibitor. *Biochemistry*, 53:4519–4525, 2014.
- [I25] B. T. Nall and E. H. Zuniga. Rates and energetics of tyrosine ring flips in yeast iso-2-cytochrome-c. *Biochemistry*, 29:7576–7584, 1990.
- [I26] S. J. Baturin, M. Okon, and L. P. McIntosh. Structure, dynamics, and ionization equilibria of the tyrosine residues in *Bacillus circulans* xylanase. *J. Biomol. NMR*, 51:379–394, 2011.
- [I27] C.-J. Yang, M. Takeda, T. Terauchi, J. Jee, and M. Kainosho. Differential large-amplitude breathing motions in the interface of FKBP12–drug complexes. *Biochemistry*, 54:6983–6995, 2015.
- [I28] U. Weininger, K. Modig, A. Geitner, P. A. Schmidpeter, J. R. Koch, and M. Akke. Dynamics of aromatic side chains in the active site of FKBP12. *Biochemistry*, 56:334–343, 2016.
- [I29] L. M. Mariño Pérez, F. S. Ielasi, L. M. Bessa, D. Maurin, J. Kragelj, M. Blackledge, N. Salvi, G. Bouvignies, A. Palencia, and M. R. Jensen. Visualizing protein breathing motions associated with aromatic ring flipping. *Nature*, 602:695–700, 2022.
- [I30] G. Wagner. Activation volumes for the rotational motion of interior aromatic rings in globular proteins determined by high resolution ^1H NMR at variable pressure. *FEBS Lett.*, 112:280–284, 1980.
- [I31] H. Li, H. Yamada, and K. Akasaka. Effect of pressure on the tertiary structure and dynamics of folded basic pancreatic trypsin inhibitor. *Biophys. J.*, 77:2801–2812, 1999.
- [I32] V. Kasinath, Y. N. Fu, K. A. Sharp, and A. J. Wand. A sharp thermal transition of fast aromatic-ring dynamics in ubiquitin. *Angew. Chem. Int. Ed.*, 54:102–107, 2015.
- [I33] D. M Rice, R. J. Wittebort, R. G. Griffin, E. Meirovitch, E. R. Stimson, Y. C. Meinwald, J. H. Freed, and H. A. Scheraga. Rotational jumps of the tyrosine side chain in crystalline enkephalin. Hydrogen-2 NMR line shapes for aromatic ring motions in solids. *J. Am. Chem. Soc.*, 103:7707–7710, 1981.
- [I34] L. Vugmeyster, D. Ostrovsky, T. Villafranca, J. Sharp, W. Xu, A. S. Lipton, G. L. Hoatson, and R. L. Vold. Dynamics of hydrophobic core phenylalanine residues probed by solid-state deuterium NMR. *J. Phys. Chem. B*, 119:14892–14904, 2015.

- [I35] P. Paluch, T. Pawlak, A. Jeziorna, J. Trébosc, G. Hou, A. J. Vega, J. Amoureux, M. Dracinsky, T. Polenova, and M. J. Potrzebowski. Analysis of local molecular motions of aromatic sidechains in proteins by 2D and 3D fast MAS NMR spectroscopy and quantum mechanical calculations. *Phys. Chem. Chem. Phys.*, 17:28789–28801, 2015.
- [I36] D. F. Gauto, P. Macek, A. Barducci, H. Fraga, A. Hessel, T. Terauchi, D. Gajan, Y. Miyanoiri, J. Boisbouvier, R. Lichtenecker, M. Kainosho, and P. Schanda. Aromatic ring dynamics, thermal activation, and transient conformations of a 468 kDa enzyme by specific ^1H – ^{13}C labeling and fast magic-angle spinning NMR. *J. Am. Chem. Soc.*, 141:11183–11195, 2019.
- [I37] D. F. Gauto, O. O. Lebedenko, L. M. Becker, I. Ayala, R. Lichtenecker, N. R. Skrynnikov, and P. Schanda. Aromatic ring flips in differently packed protein crystals: MAS NMR and MD studies of 3 ubiquitin lattices. *bioRxiv*, 2022. URL <https://www.biorxiv.org/content/early/2022/07/08/2022.07.07.499110>.
- [I38] D. E. Shaw, P. Maragakis, K. Lindorff-Larsen, S. Piana, R. O. Dror, M. P. Eastwood, J. A. Bank, J. M. Jumper, J. K. Salmon, Y. B. Shan, and W. Wriggers. Atomic-level characterization of the structural dynamics of proteins. *Science*, 330:341–346, 2010.
- [I39] M. Kulkarni and P. Söderhjelm. Free energy landscape and rate estimation of the aromatic ring flips in basic pancreatic trypsin inhibitor using metadynamics. *bioRxiv*, 2021. URL <https://www.biorxiv.org/content/early/2021/01/08/2021.01.07.425261>.
- [I40] H. Eyring. The activated complex in chemical reactions. *J. Chem. Phys.*, 3: 107–115, 1935.
- [I41] M. G. Evans and M. Polanyi. Some applications of the transition state method to the calculation of reaction velocities, especially in solution. *Trans. Faraday Soc.*, 31:875–894, 1935.
- [I42] K. J. Laidler and M. C. King. The development of transition-state theory. *J. Phys. Chem.*, 87:2657–2664, 1983.
- [I43] D. A. McQuarrie and J. D. Simon. *Physical Chemistry: A Molecular Approach*. University Science Books, 1997.
- [I44] P. A. Atkins and J. de Paula. *Atkins’ Physical Chemistry - Seventh Edition*. Oxford University Press, 2002.

- [145] R. Hetzel, K. Wüthrich, J. Deisenhofer, and R. Huber. Dynamics of aromatic amino-acid residues in globular conformation of basic pancreatic trypsin-inhibitor (BPTI). II. Semi-empirical energy calculations. *Biophys. Struct. Mech.*, 2:159–180, 1976.
- [146] C. Woodward, I. Simon, and E. Tüchsen. Hydrogen exchange and the dynamic structure of proteins. *Mol. Cell. Biochem.*, 48:135–160, 1982.
- [147] K. Wüthrich and G. Wagner. Internal motion in globular proteins. *Trends Biosci.*, 3:227–230, 1978.
- [148] J. M. Yon. Protein folding: Concepts and perspectives. *Cell. Mol. Life Sci.*, 53: 557–567, 1997.
- [149] B. M. Leu, A. Alatas, H. Sinn, E. E. Alp, A. H. Said, H. Yavaş, J. Zhao, J. T. Sage, and W. Sturhahn. Protein elasticity probed with two synchrotron-based techniques. *J. Chem. Phys.*, 132:085103, 2010.
- [150] K. Gekko. Compressibility gives new insight into protein dynamics and enzyme function. *Biochim. Biophys. Acta*, 1595:382–386, 2002.
- [151] H. Seemann, R. Winter, and C. A. Royer. Volume, expansivity and isothermal compressibility changes associated with temperature and pressure unfolding of staphylococcal nuclease. *J. Mol. Biol.*, 307:1091–1102, 2001.
- [152] N. Taulier and T. V. Chalikian. Compressibility of protein transitions. *Biochim. Biophys. Acta*, 1595:48–70, 2002.
- [153] K. Gekko, N. Obu, J. Li, and J. C. Lee. A linear correlation between the energetics of allosteric communication and protein flexibility in the Escherichia coli cyclic AMP receptor protein revealed by mutation-induced changes in compressibility and amide hydrogen-deuterium exchange. *Biochemistry*, 43:3844–3852, 2004.
- [154] K. Gekko and Y. Hasegawa. Compressibility-structure relationship of globular proteins. *Biochemistry*, 25:6563–6571, 1986.
- [155] L. D. Landau and E. M. Lifshitz. *Statistical Physics, Part I*. Elsevier Inc., 3rd edition, 1980.
- [156] K. Mori, Y. Seki, Y. Yamada, H. Matsumoto, and K. Soda. Evaluation of intrinsic compressibility of proteins by molecular dynamics simulation. *J. Chem. Phys.*, 125:054903, 2006.
- [157] D. Laage, T. Elsaesser, and J. T. Hynes. Water dynamics in the hydration shells of biomolecules. *Chem. Rev.*, 117:10694–10725, 2017.

- [158] F. Persson and B. Halle. Compressibility of the protein-water interface. *J. Chem. Phys.*, 148:215102, 2018.
- [159] C. Scharnagl, M. Reif, and J. Friedrich. Local compressibilities of proteins: Comparison of optical experiments and simulations for horse heart cytochrome-c. *Biophys. J.*, 89:64–75, 2005.
- [160] F. Persson, P. Söderhjelm, and B. Halle. The geometry of protein hydration. *J. Chem. Phys.*, 148:215101, 2018.
- [161] L. Smeller. Pressure-temperature phase diagrams of biomolecules. *Biochim. Biophys. Acta*, 1595:11–29, 2002.
- [162] T. Q. Luong, S. Kapoor, and R. Winter. Pressure – a gateway to fundamental insights into protein solvation, dynamics, and function. *ChemPhysChem*, 16: 3555–3571, 2015.
- [163] E. Steiner, J. Schlagnitweit, P. Lundström, and K. Petzold. Capturing excited states in the fast-intermediate exchange limit in biological systems using ^1H NMR spectroscopy. *Angew. Chem. Int. Ed.*, 55:15869–15872, 2016.
- [164] C. Eichmüller and N. R. Skrynnikov. *J. Biomol. NMR*, 32:281–293, 2005.
- [165] U. Weininger, A. T. Blissing, J. Hennig, A. Ahlner, Z. Liu, H. J. Vogel, M. Akke, and P. Lundström. Protein conformational exchange measured by ^1H $R_{1\rho}$ relaxation dispersion of methyl groups. *J. Biomol. NMR*, 57:47–55, 2013.
- [166] S. A. Hawley. Reversible pressure-temperature denaturation of chymotrypsinogen. *Biochemistry*, 10:2436–2442, 1971.
- [167] H. A. Kramers. Brownian motion in a field of force and the diffusion model of chemical reactions. *Physica*, 7:285–304, 1940.
- [168] M. Karplus and A. McCammon. Pressure dependence of aromatic ring rotations in proteins: A collisional interpretation. *FEBS Lett.*, 131:34–36, 1981.
- [169] T. I. Igumenova, U. Brath, M. Akke, and A. G. Palmer. Characterization of chemical exchange using residual dipolar coupling. *J. Am. Chem. Soc.*, 129: 13396–13397, 2007.

Supplement

Supporting Information to Papers I and III

Slow ring flips in aromatic cluster of GB1 studied by aromatic ^{13}C relaxation dispersion methods

Matthias Dreydoppel, Heiner N. Raum and Ulrich Weininger*

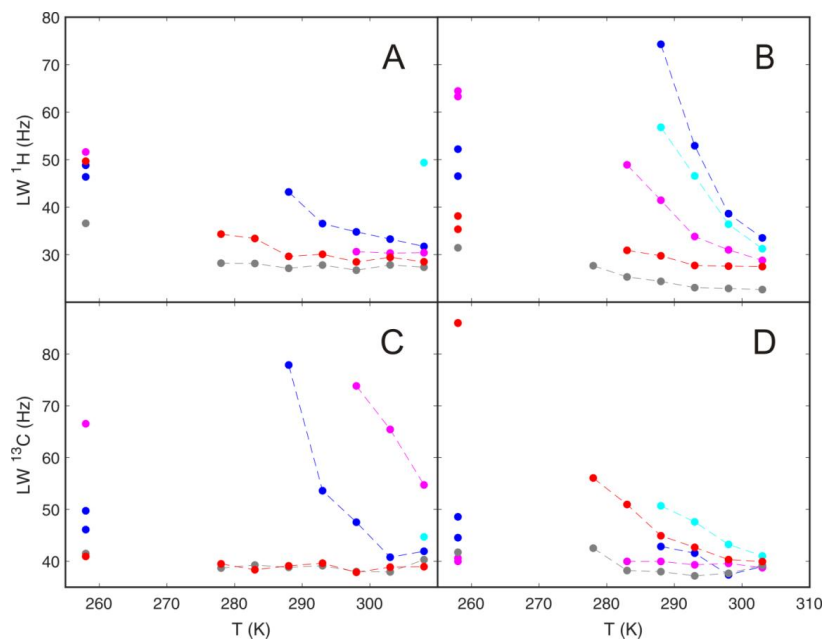
Institute of Physics, Biophysics, Martin-Luther-University Halle-Wittenberg, D-06120 Halle (Saale), Germany

* Correspondence:

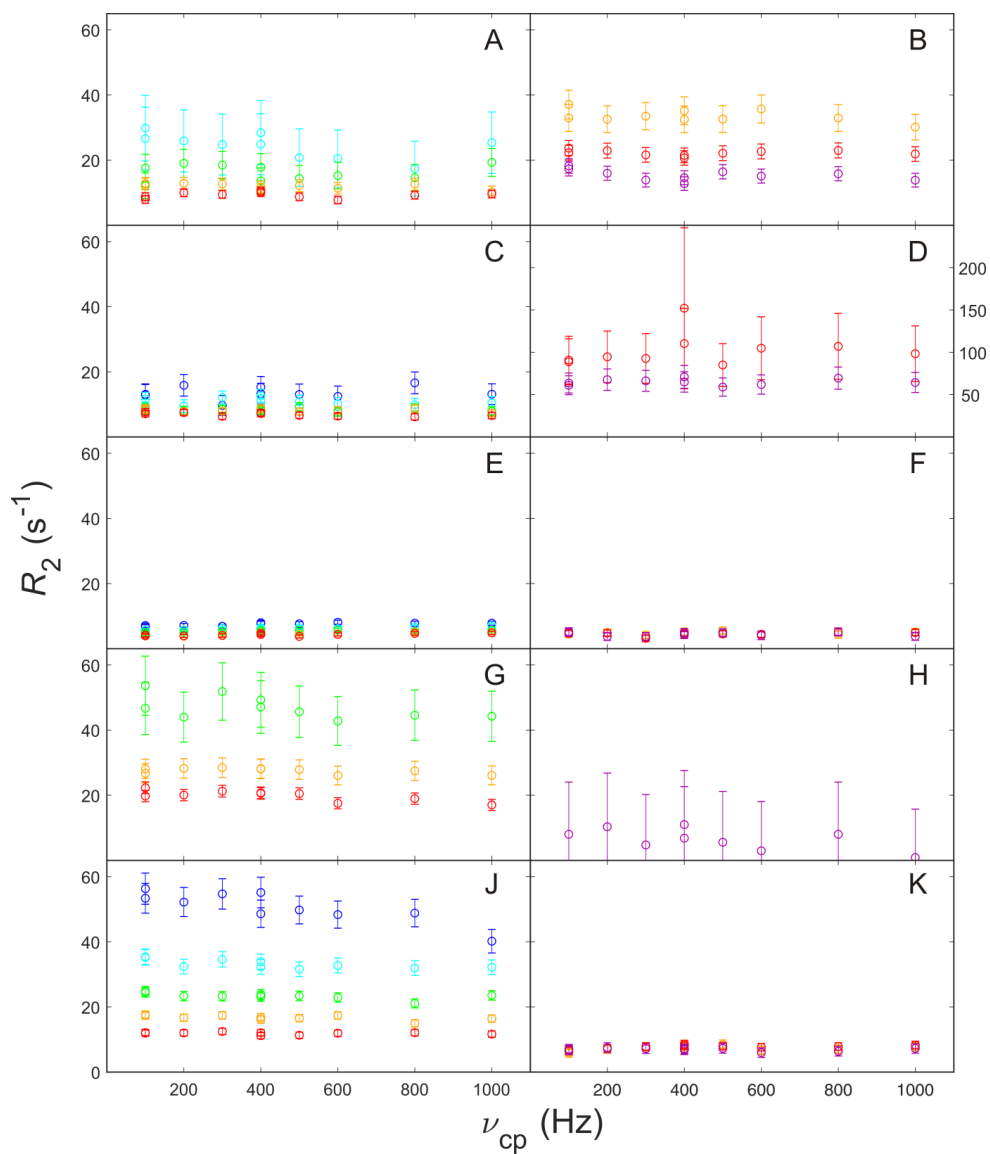
email: ulrich.weininger@physik.uni-halle.de

phone: +49 345 55 28555

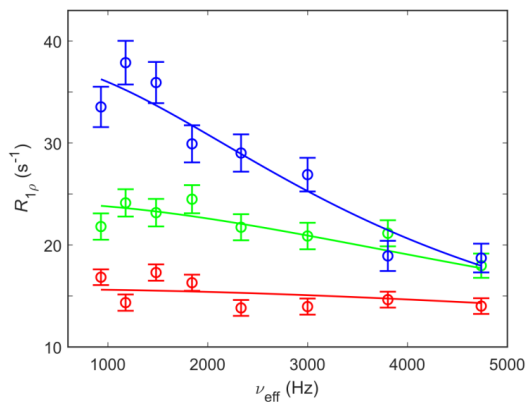
fax: +49 345 55 27161



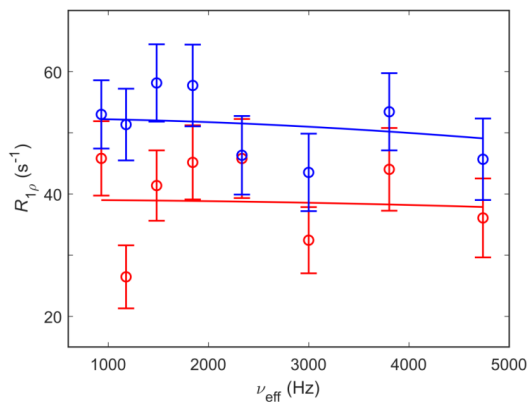
SI Fig 1: Line widths of aromatic signals that can be affected by ring flips (Phe and Tyr δ and ϵ). Y3 is shown in blue, F30 in magenta, Y33 in grey, Y45 in cyan and F52 in red. Absolute ^1H (top) and ^{13}C (bottom) line widths of δ (AC) and ϵ (BD) are plotted against the temperature. Intensities of -5°C and 200 MPa are plotted at -15°C , analog to Fig. 2.



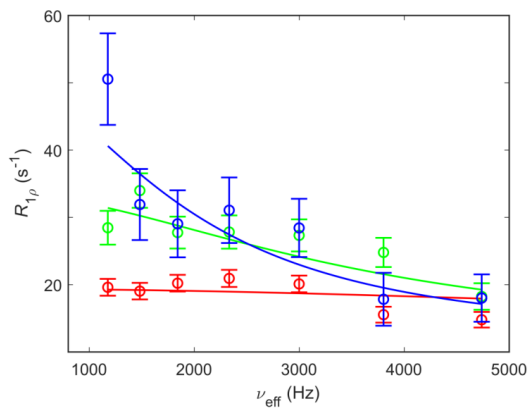
SI Fig 2: ^{13}C aromatic CPMG relaxation dispersion profiles of Y3 ϵ (A), Y3 δ (B), F30 ϵ (C), F30 δ (D), Y33 ϵ (E), Y33 δ (F), Y45 ϵ (G), Y45 δ (H), F52 ϵ (J) and F52 δ (K). Recorded on a 2 mM sample of GB1 at pH 7.0 and a static magnetic field strength of 14.1 T, at temperatures of 10 $^{\circ}\text{C}$ (blue), 15 $^{\circ}\text{C}$ (cyan), 20 $^{\circ}\text{C}$ (green), 25 $^{\circ}\text{C}$ (orange), 30 $^{\circ}\text{C}$ (red) and 35 $^{\circ}\text{C}$ (magenta).



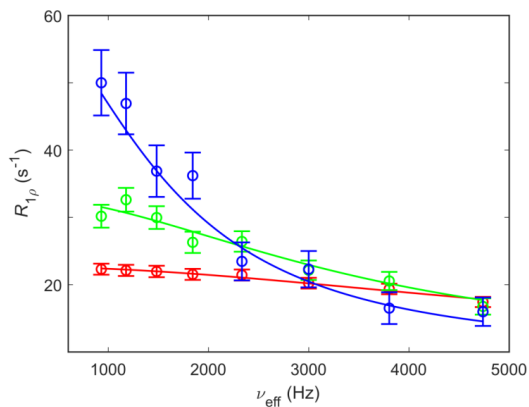
SI Fig 3: ^{13}C aromatic $R_{1\rho}$ relaxation dispersion profiles for Y3 δ recorded on-resonant ($\theta > 85^\circ$) on a 2 mM GB1 at pH 7.0 and a static magnetic field strength of 14.1 T at 25 °C (blue), 30 °C (green) and 35 °C (red). The relaxation dispersions were fitted using a fixed population $p_1 = p_2 = 0.5$ and $\Delta\delta$ fixed at the value measured from HSQC spectra under slow-exchange conditions with the restrictions: $k_{\text{flip}}(T_{\text{high}}) > k_{\text{flip}}(T_{\text{low}})$, $R_{2,0}(T_{\text{high}}) \leq R_{2,0}(T_{\text{low}})$. Derived ring flip rate constants (k_{flip}) are: $(12 \pm 2) \times 10^3 \text{ s}^{-1}$, $(20 \pm 2) \times 10^3 \text{ s}^{-1}$ and $(38 \pm 4) \times 10^3 \text{ s}^{-1}$, respectively.



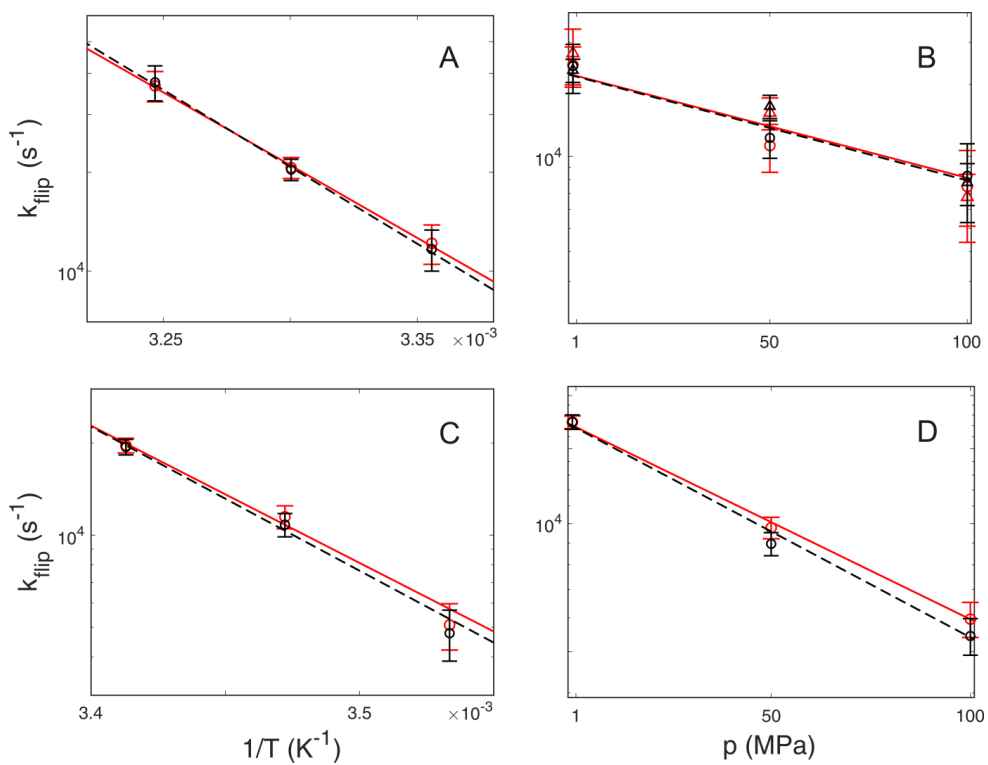
SI Fig 4: ^{13}C aromatic $R_{1\rho}$ relaxation dispersion profiles for F30 δ recorded on-resonant ($\theta > 85^\circ$) on a 2 mM GB1 at pH 7.0 and a static magnetic field strength of 14.1 T at 35 °C (blue) and 40 °C (red). The relaxation dispersions were fitted using a fixed population $p_1 = p_2 = 0.5$ and $\Delta\delta$ fixed at the value measured from HSQC spectra under slow-exchange conditions with the restrictions: $k_{\text{flip}}(T_{\text{high}}) > k_{\text{flip}}(T_{\text{low}})$, $R_{2,0}(T_{\text{high}}) \leq R_{2,0}(T_{\text{low}})$. Derived ring flip rate constants (k_{flip}) are: $(53 \pm 4) \times 10^3 \text{ s}^{-1}$ and $(75 \pm 8) \times 10^3 \text{ s}^{-1}$, respectively.



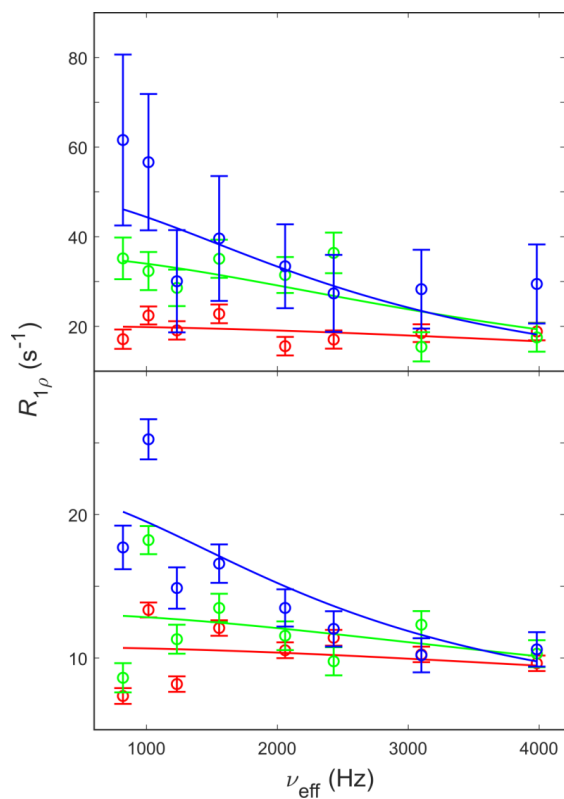
SI Fig 5: ^{13}C aromatic $R_{1\rho}$ relaxation dispersion profiles for Y45 ϵ recorded on-resonant ($\theta > 85^\circ$) on a 2 mM GB1 at pH 7.0 and a static magnetic field strength of 14.1 T at 20 °C (blue), 25 °C (green) and 30 °C (red). The relaxation dispersions were fitted using a fixed population $p_1 = p_2 = 0.5$ and $\Delta\delta$ as a free parameter with the restrictions: $k_{\text{flip}}(T_{\text{high}}) > k_{\text{flip}}(T_{\text{low}})$, $R_{2,0}(T_{\text{high}}) \leq R_{2,0}(T_{\text{low}})$. Derived ring flip rate constants (k_{flip}) are: $(6 \pm 2) \times 10^3 \text{ s}^{-1}$, $(11 \pm 2) \times 10^3 \text{ s}^{-1}$ and $(31 \pm 6) \times 10^3 \text{ s}^{-1}$, respectively.



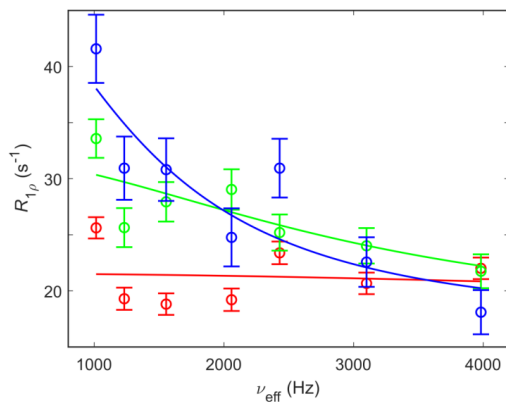
SI Fig 6: ^{13}C aromatic $R_{1\rho}$ relaxation dispersion profiles for F52 ϵ recorded on-resonant ($\theta > 85^\circ$) on a 2 mM GB1 at pH 7.0 and a static magnetic field strength of 14.1 T at 10 °C (blue), 15 °C (green) and 20 °C (red). The relaxation dispersions were fitted using a fixed population $p_1 = p_2 = 0.5$ and $\Delta\delta$ fixed at the value measured from HSQC spectra under slow-exchange conditions with the restrictions: $k_{\text{flip}}(T_{\text{high}}) > k_{\text{flip}}(T_{\text{low}})$, $R_{2,0}(T_{\text{high}}) \leq R_{2,0}(T_{\text{low}})$. Derived ring flip rate constants (k_{flip}) are: $(4.8 \pm 0.9) \times 10^3 \text{ s}^{-1}$, $(10.8 \pm 1.0) \times 10^3 \text{ s}^{-1}$ and $(19.4 \pm 1.2) \times 10^3 \text{ s}^{-1}$, respectively.



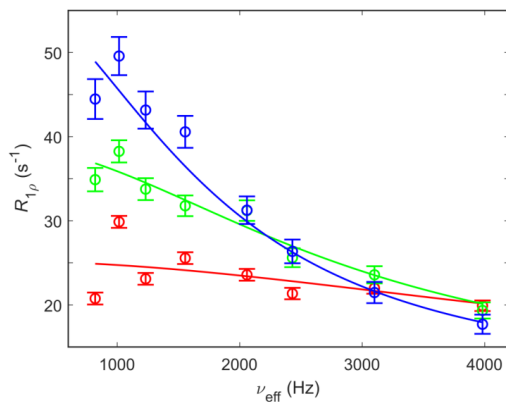
SI Fig 7: Derived flip rates by ^{13}C $R_{1\rho}$ relaxation dispersion experiments with (black) and without (red) fixed $\Delta\delta$ values from the low temperature, high pressure spectra plotted against the inverse temperature (AC) or pressure (BD). A) Y3 δ , B) Y3 δ (circles) and Y3 ϵ (triangles), CD) F52 ϵ . Black dashed and red solid lines represent the fits with and without fixed $\Delta\delta$ values as function of temperature or pressure, respectively. Derived activation parameters (with / without fixed $\Delta\delta$) are: $\Delta H^\ddagger = (87 \pm 14) / (82 \pm 12)$ kJ mol $^{-1}$, $\Delta S^\ddagger = (126 \pm 46) / (110 \pm 42)$ J mol $^{-1}$ K $^{-1}$, and $\Delta V^\ddagger = (26 \pm 5) / (26 \pm 6)$ mL mol $^{-1}$ for Y3, and $\Delta H^\ddagger = (88 \pm 11) / (83 \pm 10)$ kJ mol $^{-1}$, $\Delta S^\ddagger = (137 \pm 38) / (122 \pm 35)$ J mol $^{-1}$ K $^{-1}$, and $\Delta V^\ddagger = (29 \pm 2) / (27 \pm 2)$ mL mol $^{-1}$ for F52.



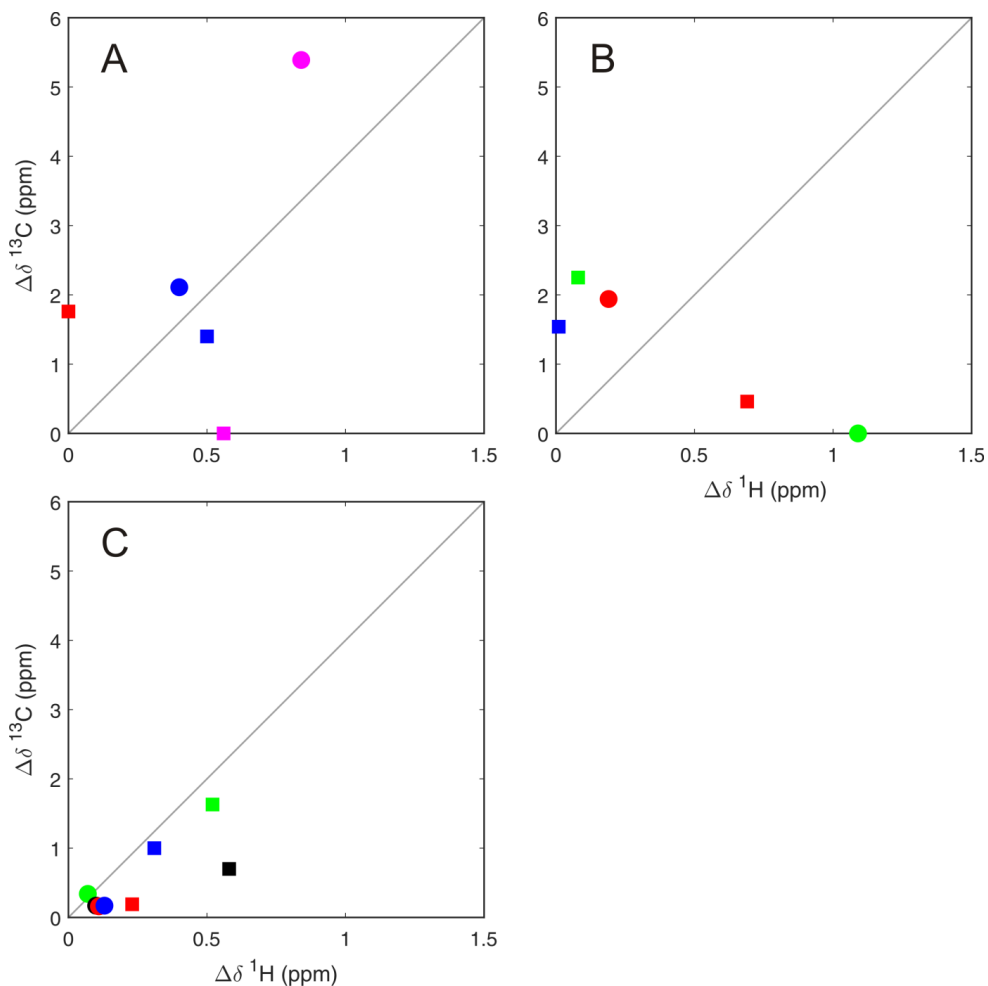
SI Fig 8: ^{13}C aromatic $R_{1\rho}$ relaxation dispersion profiles for Y3 δ (top) and ϵ (bottom) recorded on-resonant ($\theta > 85^\circ$) on a 2 mM GB1 at pH 7.0 and a static magnetic field strength of 14.1 T at 30 °C and 0.1 (red), 50 (green) and 100 MPa (blue) hydrostatic pressure. The relaxation dispersions were fitted using a fixed population $p_1 = p_2 = 0.5$ and $\Delta\delta$ fixed at the value measured from HSQC spectra under slow-exchange conditions with the restrictions: $k_{\text{flip}}(p_{\text{high}}) < k_{\text{flip}}(p_{\text{low}})$. Derived ring flip rate constants (k_{flip}) are: $(24 \pm 4) \times 10^3 \text{ s}^{-1}$, $(12 \pm 2) \times 10^3 \text{ s}^{-1}$, $(8 \pm 3) \times 10^3 \text{ s}^{-1}$ (Y3 δ); and $(23 \pm 3) \times 10^3 \text{ s}^{-1}$, $(16 \pm 2) \times 10^3 \text{ s}^{-1}$ and $(7.8 \pm 1.5) \times 10^3 \text{ s}^{-1}$ (Y3 ϵ), respectively.



SI Fig 9: ^{13}C aromatic $R_{1\rho}$ relaxation dispersion profiles for Y45 ϵ recorded on-resonant ($\theta > 85^\circ$) on a 2 mM GB1 at pH 7.0 and a static magnetic field strength of 14.1 T at 30 $^\circ\text{C}$ and 0.1 (red), 50 (green) and 100 MPa (blue) hydrostatic pressure. The relaxation dispersions were fitted using a fixed population $p_1 = p_2 = 0.5$ and $\Delta\delta$ as a free parameter with the restrictions: $k_{\text{flip}}(p_{\text{high}}) < k_{\text{flip}}(p_{\text{low}})$. Derived ring flip rate constants (k_{flip}) are: $(30 \pm 8) \times 10^3 \text{ s}^{-1}$, $(16 \pm 2) \times 10^3 \text{ s}^{-1}$ and $(4.2 \pm 1.4) \times 10^3 \text{ s}^{-1}$, respectively.



SI Fig 10: ^{13}C aromatic $R_{1\rho}$ relaxation dispersion profiles for F52 ε recorded on-resonant ($\theta > 85^\circ$) on a 2 mM GB1 at pH 7.0 and a static magnetic field strength of 14.1 T at 20 $^\circ\text{C}$ and 0.1 (red), 50 (green) and 100 MPa (blue) hydrostatic pressure. The relaxation dispersions were fitted using a fixed population $p_1 = p_2 = 0.5$ and $\Delta\delta$ fixed at the value measured from HSQC spectra under slow-exchange conditions with the restrictions: $k_{\text{flip}}(p_{\text{high}}) < k_{\text{flip}}(p_{\text{low}})$. Derived ring flip rate constants (k_{flip}) are: $(17.3 \pm 0.7) \times 10^3 \text{ s}^{-1}$, $(9.0 \pm 0.6) \times 10^3 \text{ s}^{-1}$ and $(5.4 \pm 0.5) \times 10^3 \text{ s}^{-1}$, respectively.



SI Fig 11: Aromatic ^1H and ^{13}C chemical shift differences of Tyr and Phe residues, δ positions indicated as circles and ϵ positions as squares. A) GB1 Y3, F30 and F52 in blue, magenta and red, respectively. B) BPTI Y23, Y35 and F45 in blue, green and red taken from [1, 2]. C) FKBP12 Y26 and F99 in the rapamycin-bound state in green and red, and in the FK506-bound state in black and blue, respectively, taken from [3]. The grey lines correspond to $\Delta\delta$ values being equivalent with respect to the ^1H and ^{13}C reference frequencies.

References

- [1] U. Weinger, K. Modig, M. Akke, *Biochemistry* **2014**, *53*, 4519.
- [2] G. Wagner, D. Bruhwiler, K. Wuthrich, *Journal of Molecular Biology* **1987**, *196*, 227.
- [3] C. J. Yang, M. Takeda, T. Terauchi, J. Jee, M. Kainosho, *Biochemistry* **2015**, *54*, 6983.

Supporting Information

Transition State Compressibility and Activation Volume of Transient Protein Conformational Fluctuations

Matthias Dreydoppel¹, Britta Dorn¹, Kristofer Modig², Mikael Akke² and Ulrich Weininger^{1,*}

¹ Institute of Physics, Biophysics, Martin-Luther-University Halle-Wittenberg, D-06120 Halle (Saale), Germany

² Division of Biophysical Chemistry, Center for Molecular Protein Science, Department of Chemistry, Lund University, P.O. Box 124, SE-22100 Lund, Sweden

* Ulrich Weininger

Email: ulrich.weininger@physik.uni-halle.de

Phone: +49 345 55 28555

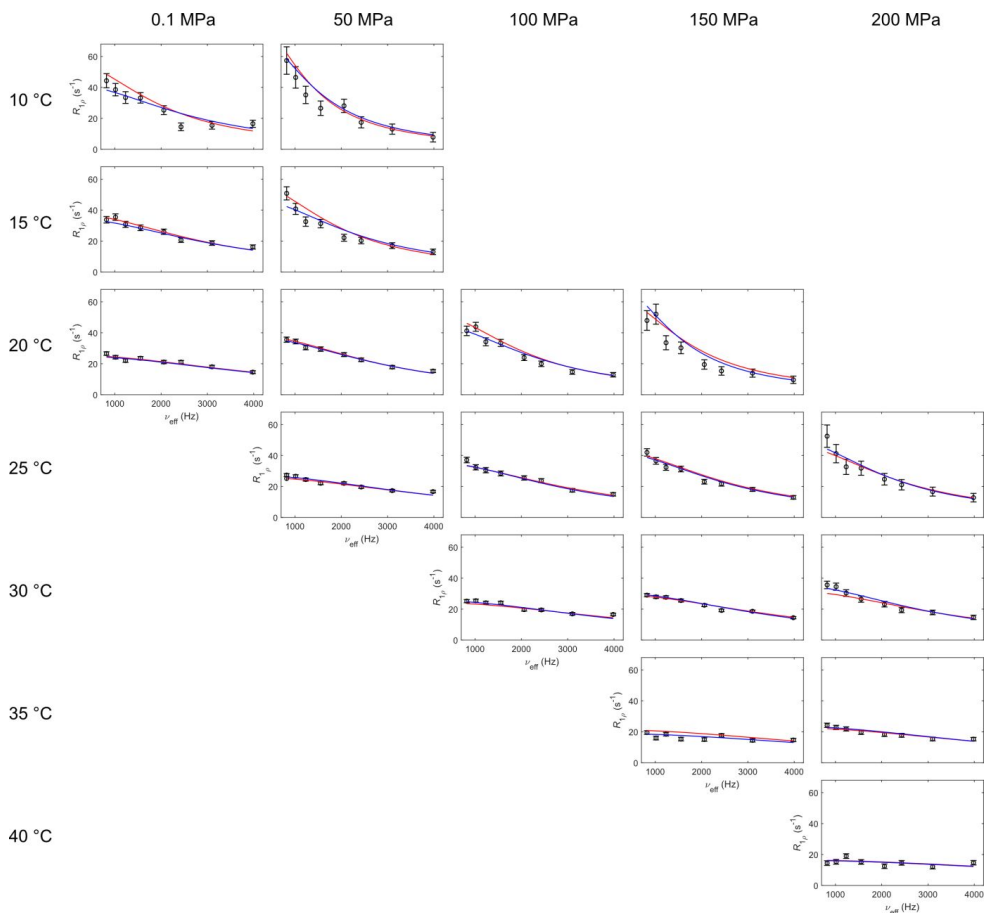


Figure S1: ^{13}C aromatic $R_{1\rho}$ relaxation dispersion profiles for F52 ϵ recorded on-resonant ($\theta > 85^\circ$) on a 5 mM sample of GB1 at pH 7.0 and a static magnetic field strength of 14.1 T. The relaxation dispersions were fitted using a fixed population $p_1 = p_2 = 0.5$ and $\Delta\delta$ fixed at the value measured from HSQC spectra under slow-exchange conditions. Blue lines depict global fits of all temperatures at each pressure, fitted with the restrictions: $k_{\text{flip}}(T_{\text{high}}) > k_{\text{flip}}(T_{\text{low}})$, and $R_{2,0}(T_{\text{high}}) \leq R_{2,0}(T_{\text{low}})$. Derived ring flip rate constants (k_{flip}) are given in Table 1. Red lines depict the global fit of all relaxation dispersions directly to the model given by Eq. (6), with the restriction: $R_{2,0}(T_{\text{high}}) \leq R_{2,0}(T_{\text{low}})$ for sets of equal pressure.

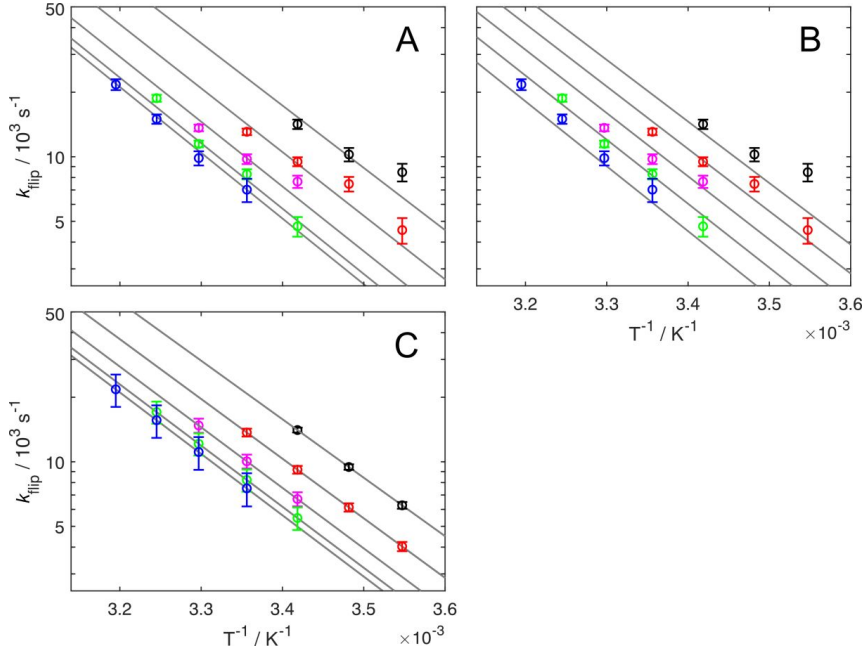


Figure S2: Temperature and pressure dependence of flip rates. k_{flip} is plotted as a function of $1/T$ for F52 at pressures of 0.1 MPa (black), 50 MPa (red), 100 MPa (magenta), 150 MPa (green) and 200 MPa (blue). The solid lines represent the fitted model including the activation parameters $\Delta^\ddagger G_0$, $\Delta^\ddagger S_0$, and $\Delta^\ddagger V_0$ at the reference point of 0.1 MPa and 293 K, as well as $\Delta^\ddagger \kappa^2$, according to Eq. (6). (A) Flip rates derived from $R_{1\rho}$ relaxation dispersions, based on simultaneous fits of all data (all temperatures) at a given pressure using the restrictions $k_{\text{flip}}(T_{\text{high}}) > k_{\text{flip}}(T_{\text{low}})$, and $R_{2,0}(T_{\text{high}}) \leq R_{2,0}(T_{\text{low}})$. (B) Flip rates as in A, fitted with the restriction $\Delta^\ddagger \kappa^2 = 0$. (C) Global fitting of $\Delta^\ddagger G_0$, $\Delta^\ddagger S_0$, $\Delta^\ddagger V_0$, and $\Delta^\ddagger \kappa^2$ directly to all temperature and pressure dependent relaxation dispersion data. In C, flip rates are subsequently calculated from the fitted thermodynamic parameters, and error bars are derived by error propagation; for this reason, error bars are larger for data points further from the reference point.

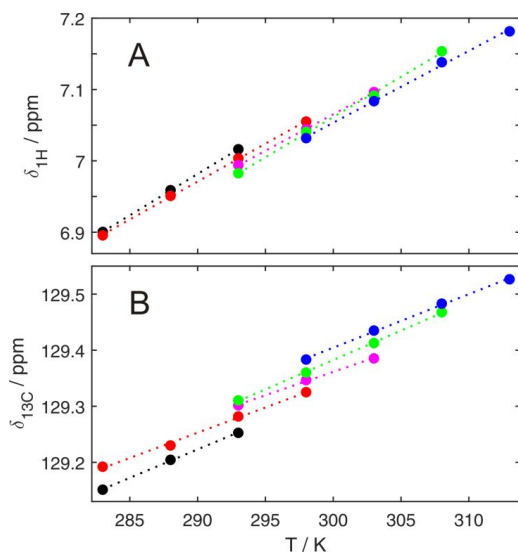


Figure S3: Temperature and pressure dependence of chemical shifts of the averaged signal of F52ε. $\delta_{1\text{H}}$ (A) and $\delta_{13\text{C}}$ (B) are plotted as a function of T at pressures of 0.1 MPa (black), 50 MPa (red), 100 MPa (magenta), 150 MPa (green) and 200 MPa (blue). Dotted lines depict linear fits of $\delta(T)$ at the respective pressures. Slopes of the linear fits range from 0.010 to 0.011 ppm/K for ^1H and from 0.008 to 0.010 ppm/K for ^{13}C . At temperatures of 293 and 298 K, shift changes with pressure are less than or equal to 0.22 ppm/GPa for ^1H and 0.39 ppm/GPa for ^{13}C , respectively.

Curriculum vitae

Personal data

Family name: Dreydoppel
First name: Matthias
Date of birth: 24 March 1993
Place of birth: Neuwied
Nationality: German

Education

05/2018 - present	Doctoral studies <i>incl.</i>	Martin-Luther-University Halle-Wittenberg
04/2021 - 08/2021	Research traineeship	CMPS, Lund University
10/2015 - 03/2018	Master studies (M. Sc. Medical Physics)	Martin-Luther-University Halle-Wittenberg
10/2012 - 09/2015	Bachelor studies (B. Sc. Medical Physics)	
03/2012	Abitur	Werner-Heisenberg- Gymnasium Neuwied

Statutory Declaration – Eidesstattliche Erklärung

Hiermit versichere ich, dass ich die vorliegende Arbeit selbständig und ohne fremde Hilfe verfasst, keine anderen als die von mir angegebenen Quellen und Hilfsmittel benutzt und die den benutzten Werken wörtlich oder inhaltlich entnommenen Stellen als solche kenntlich gemacht habe.

Ich erkläre, dass ich keine anderweitigen Promotionsversuche unternommen und die vorliegende Dissertation weder in der gegenwärtigen noch in einer anderen Fassung einer anderen wissenschaftlichen Einrichtung vorgelegt habe.

Halle (Saale), im Dezember 2022

Matthias Dreydoppel

Acknowledgements – Danksagung

There are many people who made this thesis possible by their contribution. I wish to express my cordial thanks to all of them!

First and foremost thanks to Uli, for your friendly and purposeful guidance and for the countless things I could learn from you.

Thanks to Jochen and Mikael for your teaching and creativity and for being open-hearted supervisors.

Thanks to the entire biophysics group in Halle! To Bruno, Celia, Detlef, Heiner, Kathrin, Malte, Manuel, Tobias, Shubhra, Stefan and Rositta for your help and many enjoyable coffee rounds.

Thanks to Göran from whom I could learn much within a short period of time. Just as many thanks to Chris, Johan, Kristofer and Olof for making my summer in Lund a great scientific and personal experience.

Viele weitere Menschen haben meine Doktorandenjahre zu einer wunderbaren Zeit gemacht. Allen ein großes Dankeschön!

Danke an Martin, dass wir den ganzen Weg seit dem ersten Semester zusammen gegangen sind. Mit dir hat mir das Studium erst wirklich Spaß gemacht!

Danke an Clara, Clemens, Emma, Jette, Ludwig, Markus, Micha, Milena, Paula und Roman für eure Freundschaft und die gemeinsame Musik.

Danke an Tillman und Max für viel Forschergeist und Inspiration. Danke an Karin für das Titelbild!

Danke an Mama, Papa und Markus, dass ihr für mich da seid und an mich glaubt.